An inclusive measurement of the branching fraction for $B \to X_s\gamma$ using the recoil of fully reconstructed B meson decays

Clare Louise Brown

Physics Department

Royal Holloway, University of London

Submitted to the University of London

for the Degree of Doctor of Philosophy.

June 2005.

Abstract

The $b \to s\gamma$ transition is an electroweak "loop" penguin process that occurs in decays of the B meson. It is of high theoretical interest due to the possibility of new high-mass virtual particles entering the loop and contributing to the decay amplitude. A measurement of the inclusive $B \to X_s\gamma$ branching fraction has been carried out. The measurement is based on a data sample of 230 million $\Upsilon(4S) \to B\overline{B}$ events collected with the *BABAR* detector at the e^+e^- PEP-II storage ring at SLAC. A technique of studying the recoil to fully reconstructed B meson hadronic decays is employed, which eliminates the background from non-B decays. The large data sample available enables this method to be used, even though the efficiency for reconstructing a B meson is small (∼0.3%). The branching fraction is obtained from the yield of the signal photon energy spectrum. The result is

$$\mathcal{B}(\mathbf{B \to X_s}\gamma) = (\mathbf{4.04 \pm 0.83(stat.) \pm 0.48(syst.)^{+0.29}_{-0.32}(theo.)) \times 10^{-4}}$$

which is compatible with the current theoretical prediction and previous experimental measurements. The statistical uncertainty is the largest error at present, but as more data become available the technique will provide a very precise measurement of $\mathcal{B}(B \to X_s\gamma)$.

Acknowledgments

I would like to thank my supervisor Tania McMahon for her advice, support and encouragement throughout my PhD and Mike Green for his support during the later stages. I am grateful for the useful comments they both provided on this thesis.

I was fortunate to be a member of the other fully-inclusive $b \to s\gamma$ group at *BABAR* during the first year of my PhD. I benefited from the guidance of the members of this group and wish to thank them all. I am particularly grateful to Erkcan Ozcan and Ruth Schmitz who were extremely kind and always willing to help me.

I must thank Oliver Buchmüller and Henning Flächer for introducing me to the idea of measuring the $B \to X_s\gamma$ branching fraction using a sample of fully reconstructed B mesons. This sample was developed by the Inclusive Semileptonic Analysis Working Group at *BABAR* and I appreciate their work on this. Thanks again to Henning for his efforts in generating the event samples used in this thesis. A special thanks goes to Fabio Bellini, with whom I worked in partnership to develop the analysis. I also profited from the advice of Oliver, Henning, Riccardo Faccini and Daniele del Re.

Thoughout my time spent at Royal Holloway and SLAC, I have met many people who have made this experience enjoyable. I thank them all. It was a pleasure to share an office with the other Royal Holloway *BABAR* members: Fabrizio, Stefania, Ajit, Chris, Henning, Mark, Bob and Paul. They all made my days interesting and were always willing to help solve my problems. The *BABAR* students from other British universities were great company during my stay in California and I have wonderful memories of times spent with them. In addition, I am lucky to have lived with such great flatmates during my final year at Royal Holloway, who frequently baked delicious cookies and cakes.

Last but by no means least, I thank my family. My parents and brother have stood by me through all my decisions. Without their eternal support I would never have achieved what I have to date.

Contents

List of Figures

List of Tables

Chapter 1

Introduction

Electroweak "penguin" loop decays of B mesons induce flavour changing neutral currents which are otherwise forbidden in the Standard Model of Particle Physics (SM). Such decay processes were first proposed theoretically by John Ellis in 1977 [1]. Their existence was confirmed much later in 1993 by the CLEO experiment in their observation of the $B \to K^*\gamma$ decay [2], a form of the $b \to s\gamma$ transition.

The $b \to s\gamma$ penguin decay is of high theoretical interest. The presence of new high-mass virtual particles in the loop mediating the transition may influence the decay rate. Hence, a precision measurement of the $B \to X_s\gamma$ branching fraction is important to test the SM prediction and provide constraints on proposed theories of new particles.

The next-to-leading order theoretical calculation of the branching fraction based on the Standard Model has been performed [3], yielding a central value of:

$$\mathcal{B}(B \to X_s\gamma) = 3.70 \times 10^{-4} \tag{1.1}$$

To date experimental measurements agree with this prediction. The current world average result [4] is:

$$\mathcal{B}(B \to X_s\gamma) = (3.52^{+0.30}_{-0.28}) \times 10^{-4} \tag{1.2}$$

The measurements that contribute to this value are discussed in section 1.1. The largest experimental uncertainty, after statistical limitations, comes from a restriction on the energy of the final state photon. A minimum photon energy requirement is necessary to exclude the background dominated region of the photon energy spectrum where it is difficult to extract signal events. To extrapolate the measured region to the full photon energy

Experiment	Year	Ref.	min. E^*_γ (GeV)	$\mathcal{B}(B \to X_s\gamma) \times 10^4$
CLEO	1995	[5]	2.20	2.32 ± 0.57(stat.)± 0.35(syst.)
ALEPH	1998	[6]	2.20	3.11 ± 0.80(stat.)± 0.72(syst.)
BELLE	2001	[7]	~ 2.24	3.36 ± 0.53(stat.)± 0.42(syst.)$^{+0.50}_{-0.54}$(theo.)
CLEO	2001	[8]	2.00	3.21 ± 0.43(stat.)± 0.27(syst.)$^{+0.18}_{-0.10}$(theo.)
BABAR	2002	[9]	2.10	4.30 ± 0.50(stat.)± 0.80(syst.)± 1.3(theo.)
BABAR	2002	[10]	2.10	3.88 ± 0.36(stat.)± 0.37(syst.)$^{+0.43}_{-0.23}$(theo.)
BELLE	2004	[11]	1.80	3.55 ± 0.32(stat.)$^{+0.30}_{-0.31}$(syst.)$^{+0.11}_{-0.07}$(theo.)

Table 1.1: Previous measurements of the $B \to X_s\gamma$ branching fraction. The minimum photon energy requirement (measured in the centre-of-mass frame) used to select $B \to X_s\gamma$ events is shown for each analysis.

spectrum a signal model must be assumed, thus introducing model dependence in the final result. Suppressing the background as much as possible in order to select signal events at the lower end of the photon energy spectrum is an important objective for all $B \to X_s\gamma$ analyses.

This thesis presents an alternative measurement of the inclusive $B \to X_s\gamma$ branching fraction using 210.5 fb^{-1} of data ($\sim$ 230 million $B\overline{B}$ pairs) collected by the *BABAR* detector. In this analysis the $B \to X_s\gamma$ decay is identified by the presence of a highly energetic photon recoiling from a fully reconstructed B meson. This technique effectively eliminates the background from non-B decays, allowing extraction of signal events down to photon energies of 1.9 GeV. A summary of the analysis is given in section 1.2.

1.1 Previous Measurements

The results of previous $B \to X_s\gamma$ branching fraction analyses, together with the minimum photon energy requirements applied to select signal events, are summarized in table 1.1. The analyses each exploit different techniques to isolate signal events from background.

The first result [5] was published in 1995 by the CLEO collaboration using a sample of 2.2 million $B\overline{B}$ pairs from $e^+e^- \to \Upsilon(4S) \to B\overline{B}$ events. This measurement is a combination of results from a semi-inclusive analysis and a fully-inclusive analysis. In the semi-inclusive approach, the final states $K(n\pi)\gamma$ with $n \leq 4$ and at most one π^0 were reconstructed. Since these represent only half of the possible final states, a large model dependence was introduced to extrapolate the measured partial rate to the full decay rate. For the fully-inclusive approach only the photon was reconstructed. To reduce the large background associated with this method, topological differences between isotropic $B\overline{B}$ events and jet-like continuum events ($e^+e^- \rightarrow u\overline{u}$,$d\overline{d}$,$s\overline{s}$,$c\overline{c}$) were exploited. Event shape variables were combined into one variable using a neural network designed to discriminate signal events from background.

CLEO's result was confirmed in 1998 by the ALEPH collaboration using 0.8 million $B\overline{B}$ pairs identified in Z^0 decays [6]. In their analysis, selected events were tagged for b-quark content in one hemisphere which minimized the continuum background. The $B \rightarrow X_s\gamma$ signal in the other hemisphere was characterized by the presence of a hard photon associated with a system of high momentum and high rapidity hadrons, orginiating from a displaced secondary vertex.

The BELLE experiment published their first $B \rightarrow X_s\gamma$ branching fraction measurement [7] in 2001 based on a sample of 6 million $B\overline{B}$ decays. Their analysis used the semi-inclusive technique of reconstructing the $B \rightarrow X_s\gamma$ decay from a photon, a kaon and multiple pions.

In 2001 CLEO produced a new result [8] which superseded their original measurement, using a data sample of 10 million $B\overline{B}$ pairs. In this analysis the probability of being a $B \rightarrow X_s\gamma$ decay rather than continuum decay was computed for each event. This probability was based on the event topology, the reconstruction of expected signal modes, and the presence of a lepton in the event. B events are more likely to have a high momentum lepton in the final state than continuum events, and for signal events the lepton will originate from the non-signal B. This sophisticated approach for selecting signal events enabled CLEO to measure the shape of the photon energy spectrum and extract the HQET parameter $\overline{\Lambda}$, which is the difference in mass between the B meson and b quark.

The *BABAR* collaboration presented two preliminary $B \rightarrow X_s\gamma$ branching fraction results [9, 10] at the International Conference on High Energy Physics in 2002. One result was obtained with a semi-inclusive technique, and this incurred a large theoretical uncertainty from the extrapolation of the measured partial rate to the full decay rate. The other analysis used a fully inclusive technique. Since a large sample of 60 million $B\overline{B}$ pairs was available for this measurement, a low efficiency ($\sim 5\%$) lepton tag requirement was applied to greatly reduce the continuum background. Work is currently underway to improve the precision on both of these measurements.

The most precise $B \to X_s\gamma$ branching fraction result to date [11] was obtained by the BELLE experiment in 2004. A fully inclusive technique was applied to a data sample of ~ 150 million $B\overline{B}$ pairs. A detailed study of the B background types was performed and identified types were subtracted using simulated distributions scaled by data control samples. In addition the selection criteria were optimized to maximize the sensitivity to the signal in the photon energy region 1.8 to 1.9 GeV. This enabled the integral and shape of the photon energy spectrum to be measured down to an energy of 1.8 GeV.

1.2 Analysis Overview

The $B \to X_s\gamma$ branching fraction analysis presented in this thesis is based on the study of high energetic photons recoiling against fully reconstructed B mesons. Requiring a fully reconstructed B meson in the event is an effective way of rejecting continuum background. A semi-exclusive reconstruction algorithm is used to reconstruct as many hadronic B meson decays as possible. The reconstruction efficiency is very low ($\sim 0.3\%$), but fortunately the *BABAR* detector has collected a large data sample of approximately 230 million $B\overline{B}$ pairs which makes the analysis technique feasible.

The analysis is designed to be fully inclusive with minimal requirements on the signal photon or X_s system. A requirement that the photon energy exceeds 1.9 GeV is however necessary to exclude the region where the signal is overwhelmed by background. To suppress the background from continuum events, event shape variables that exploit the difference in event topology between continuum and $B\overline{B}$ events are used. Reducing the background from non-signal B decays is more of a challenge since their global event topology is the same as that of the signal events. The B background consists mainly of photons from asymmetric decays of π^0 s and η s, and also hadronic interactions that fake highly energetic photons. Selection criteria are designed to provide maximum rejection of this background whilst maintaining a high signal selection efficiency.

After applying the selection criteria, the remaining continuum background is removed by requiring a well reconstructed B meson in the event. To extract the $B \to X_s\gamma$ event yield, a binned χ^2 fit of the simulated signal and B background samples to the measured photon energy distribution is performed.

The analysis is carried out “blind” to avoid introducing a bias. This means that the whole analysis technique including optimization of the selection criteria is fixed using only simulated events before the measurement is performed on real (un-blinded) data.

1.3 Structure of this Thesis

The second chapter of this thesis provides the theoretical foundations relevant to the analysis. A description of the Standard Model is given and possible undiscovered particles that may exist in the loop of $b \to s\gamma$ decays are introduced. The theoretical calculation of the $B \to X_s\gamma$ branching fraction and the photon energy spectral shape are also described.

Chapter 3 describes the PEP-II B factory and the *BABAR* detector. Details of how the raw data are collected and used to reconstruct and identify particles are given.

The available data and simulated event samples used in this analysis are detailed in chapter 4. In addition, this chapter describes the semi-exclusive method for B meson reconstruction and the fitting technique used to extract the event yield of well reconstructed B meson candidates.

Chapter 5 describes the criteria used to select $B \to X_s\gamma$ events. The selection efficiency for the signal and background samples and the composition of the B background are detailed at the end of the chapter.

The methods for extracting the signal event yield and measuring the branching fraction are described in chapter 6. Results of validation studies based on simulated data, and the final un-blinded result on data are also given in this section.

Evaluation of the systematic and theoretical uncertainties associated with the result are discussed in chapter 7, and the conclusions are given in chapter 8.

Chapter 2

Theoretical Foundations

The goal of particle physics is to identify the elementary constituents of matter and understand the nature of the forces acting between them. Throughout the 1950s and 1960s a vast number of particles were discovered from scattering experiments. Later developments have concluded that these particles, and in fact all matter, are composed of a relatively small number of fundamental particles. The Standard Model of Particle Physics (SM) classifies the fundamental particles and explains the interactions between them in a quantum field theory. It is an extremely successful model which correctly predicts a wealth of particle and decay properties which no measurement to date can challenge. An overview of the Standard Model is given in this chapter, although more detailed descriptions can be found in many particle physics textbooks, such as [12].

The Standard Model is far from the "final answer" in particle physics. Theoretical predictions of particles yet to be observed include the Higgs Boson and Supersymmetry, which are introduced in this chapter. The $B \to X_s\gamma$ decay is sensitive to such new physics. Comparing precision measurements of the decay rate with the Standard Model prediction can either suggest that new physics exists, or provide constraints on proposed theories. Section 2.3 discusses the Standard Model calculation of the $B \to X_s\gamma$ branching fraction.

Experimentally the branching fraction is determined from the integral of the measured $B \to X_s\gamma$ photon energy spectrum. The Kagan and Neubert model for the spectrum is described in section 2.4. This model is used to simulate $B \to X_s\gamma$ signal events for the branching fraction measurement presented in this thesis.

2.1 The Standard Model

In the Standard Model (SM), the fundamental matter particles consist of spin-1/2 fermions which interact by exchanging spin-1 gauge bosons. These particles are structureless at resolutions reachable by current accelerators. Table 2.1 gives details of the particles and their quantum numbers (baryon number B, lepton number L, and charge Q) which are conserved in reactions.

Type	Particle	Spin ($\hbar$)	Baryon Number B	Lepton Number L	Charge Q (e)
Quarks	u (up)	1/2	1/3	0	+2/3
	d (down)	1/2	1/3	0	-1/3
	c (charm)	1/2	1/3	0	+2/3
	s (strange)	1/2	1/3	0	-1/3
	t (top)	1/2	1/3	0	+2/3
	b (bottom)	1/2	1/3	0	-1/3
Leptons	e^- (electron)	1/2	0	1	-1
	ν_e (electron neutrino)	1/2	0	1	0
	μ^- (muon)	1/2	0	1	-1
	ν_μ (muon neutrino)	1/2	0	1	0
	τ^- (tau)	1/2	0	1	-1
	ν_τ (tau neutrino)	1/2	0	1	0
Gauge Bosons	γ (photon)	1	0	0	0
	Z^0, W^+, W^- (weak bosons)	1	0	0	$0, +1, -1$
	g_i ($i = 1, .., 8$ gluons)	1	0	0	0

Table 2.1: The fundamental particles and some of their quantum numbers. The corresponding antiparticles of the quarks and leptons are dentoted by a bar (i.e. $\overline{u}$, $\overline{d}$) or opposite charge sign (i.e. e^+, μ^+) and are identical except for the reversal of the sign of their B, L and Q numbers.

Fermions come in two types: leptons and quarks. Unlike leptons which are observed separately, quarks are always bound together in groups of three called baryons (with $B = 1$, $L = 0$), or as a quark-antiquark pair called a meson (with $B = L = 0$). For example, the quark contents of B mesons are $B^+ = u\overline{b}$, $B^- = \overline{u}b$, $B^0 = d\overline{b}$ and $\overline{B}^0 = \overline{d}b$. Baryons and mesons are collectively called hadrons. Matter present today is composed of protons (uud quarks), neutrons (udd quarks) and electrons, which make up the atoms of the chemical elements. In addition, an electron anti-neutrino is produced in radioactive β-decay ($n \to pe^-\overline{\nu}_e$). All other particles can only be produced in high energy collisions.

The type of force a particle experiences depends on the charges it carries. Particles with electric charge interact electromagnetically through the exchange of a photon. All fermions carry weak isospin, so can interact weakly through the exchange of a Z, W^+ or W^- boson. Only the quarks, which carry the additional quantum number "colour charge", interact through the strong force. This force is responsible for binding quarks into colour neutral bound states and it is mediated by eight gluons. Quantum Chromo-Dynamics (QCD) is the theory that describes interactions of the strong force. Theoretical calculations of many processes, including the $B \to X_s\gamma$ decay, become very complicated when considering strong interaction effects.

All particle interactions are modelled by a quantum field theory requiring the invariance of a Lagrangian under local gauge transformations. The Lagrangian describes the fields experienced by the particles and their masses and couplings. The SM unifies the weak and electromagnetic forces in a theory with four gauge fields; γ and the massive bosons, Z, W^+ and W^-. The γ remains massless whilst the weak gauge fields acquire mass by the spontaneous breaking of electroweak gauge symmetry induced by the Higgs mechanism [13]. It is still uncertain if and at what energy scale the strong force can be unified with the electroweak model. Gravity is not included in the SM at present, but fortunately for typical particle physics processes gravitational effects are negligible.

2.1.1 The CKM matrix

When the quark model was first introduced, only the quark flavours u, d and s were required to describe known particles. From the observed rates of weak decays, it was found that the coupling constants for the vertex $W^- \to \overline{u}s$ was four or five times less than the coupling constant for $W^- \to \overline{u}d$. Furthermore, both coupling constants were smaller than the weak coupling constant, G_F, measured for the leptonic weak interaction $W^- \to \overline{\nu}_e e^-$. In 1963 Cabibbo [14] proposed that G_F should not be applied to the $W^- \to \overline{u}s$ or $W^- \to \overline{u}d$ vertices alone, but to W^- and $\overline{u}$ coupled to a superposition of s and d states given by:

$$d' = d\cos\theta_C + s\sin\theta_C \tag{2.1}$$

where θ_C is the Cabibbo mixing angle, found experimentally to be 12.8°. Thus, G_F is reduced by the factors $\cos\theta_C$ and $\sin\theta_C$ for the vertices $W^- \to \overline{u}d$ and $W^- \to \overline{u}s$ respectively.

In 1970, Glashow, Iliopolous, and Maiani (GIM) [15] predicted the existence of the c quark before its discovery, to explain the small decay rate observed for $K^0 \to \mu^+\mu^-$. They assumed that c couples to s' which is orthogonal to d' and defined as:

$$s' = -d\cos\theta_C + s\sin\theta_C \tag{2.2}$$

The coupling of the d and s quarks to the W^- boson can be expressed as:

$$\begin{pmatrix} d' \\ s' \end{pmatrix} = \begin{pmatrix} cos\,\theta_C & sin\,\theta_C \\ -sin\,\theta_C & cos\,\theta_C \end{pmatrix} \begin{pmatrix} d \\ s \end{pmatrix} \tag{2.3}$$

The GIM scheme ensures that there are no $s \leftrightarrow d$ transitions which change the flavour of the quarks, but not their charge.

When the b (bottom) quark was discovered, it was proposed that it should have a partner, the t (top) quark. Weak interactions therefore operate on three doublets of quarks:

$$\begin{pmatrix} u \\ d' \end{pmatrix} \quad \begin{pmatrix} c \\ s' \end{pmatrix} \quad \begin{pmatrix} t \\ b' \end{pmatrix} \tag{2.4}$$

In 1973 Kobayashi and Maskawa extended the Cabibbo-GIM idea to include the third generation of quarks, and introduced the CKM matrix:

$$\begin{pmatrix} d' \\ s' \\ b' \end{pmatrix} = \begin{pmatrix} V_{ud} & V_{us} & V_{ub} \\ V_{cd} & V_{cs} & V_{cb} \\ V_{td} & V_{ts} & V_{tb} \end{pmatrix} \begin{pmatrix} d \\ s \\ b \end{pmatrix} \tag{2.5}$$

The CKM matrix is unitary ($V_{CKM}V^{\dagger}_{CKM} = 1$) and the matrix elements are measured experimentally. When the unitary condition is imposed on the measured quantities, the 90% confidence limits for the magnitude of the elements are [16]:

$$|V_{CKM}| = \begin{pmatrix} 0.9741 - 0.9756 & 0.219 - 0.226 & 0.0025 - 0.0048 \\ 0.219 - 0.226 & 0.9732 - 0.9748 & 0.038 - 0.044 \\ 0.004 - 0.014 & 0.037 - 0.044 & 0.9990 - 0.9993 \end{pmatrix} \tag{2.6}$$

Leading diagonal elements are close to one, and therefore the coupling is strongest for vertices with quarks belonging to the same generation. Transitions can occur across generations, but the unitary condition imposes that the charges of the quarks must differ. This forbids the decay of a b quark into an s quark through a direct Z emission (in the form of a tree level diagram). The $b \to s\gamma$ decay can only proceed through a second order process (see section 2.2) which influences the decay rate.

CP Violation in the Standard Model

The unitary condition of CKM matrix implies that the matrix elements are not independent. The Wolfenstein parameterization [17] is a convenient way to express the matrix, and is written:

$$V_{\mathrm{CKM}} = \begin{pmatrix} 1-\frac{\lambda^2}{2} & \lambda & A\lambda^3(\rho - i\eta) \\ -\lambda & 1-\frac{\lambda^2}{2} & A\lambda^2 \\ A\lambda^3(1-\rho-i\eta) & -A\lambda^2 & 1 \end{pmatrix} + \mathcal{O}(\lambda^4)\,. \tag{2.7}$$

where λ, A, and ρ, are real and η represents a complex phase. This complex phase is the source of CP violation in weak decays of quarks [18], hence CP violation can only occur if there are at least three generations of quarks in the Standard Model.

Various relations between the CKM matrix elements arise from the unitarity condition, but the most interesting for B decays is:

$$V_{ud}V_{ub}^* + V_{cd}V_{cb}^* + V_{td}V_{tb}^* = 0. \tag{2.8}$$

This is represented by a triangle in the complex plane, known as the Unitarity Triangle. Figure 2.1(b) shows the Unitarity Triangle where all sides are divided by $|V_{cd}V_{cb}^*|$ so that the apex of the triangle represents the Wolfenstein parameters (ρ, η). For CP violation to occur η must be non-zero, hence the internal angles of the triangle must also be non-zero.

The amount of CP violation predicted by the Standard Model is too small to account for the matter-antimatter asymmetry of the Universe, although new undiscovered phenomena could enhance this. It is therefore important to obtain precise experimental measurements of the angles and sides of the Unitarity Triangle to test the SM predictions. This is the main objective of the *BABAR* experiment as the parameters can be determined from measurements of B meson decays. To date, *BABAR*'s measurements of the Unitary

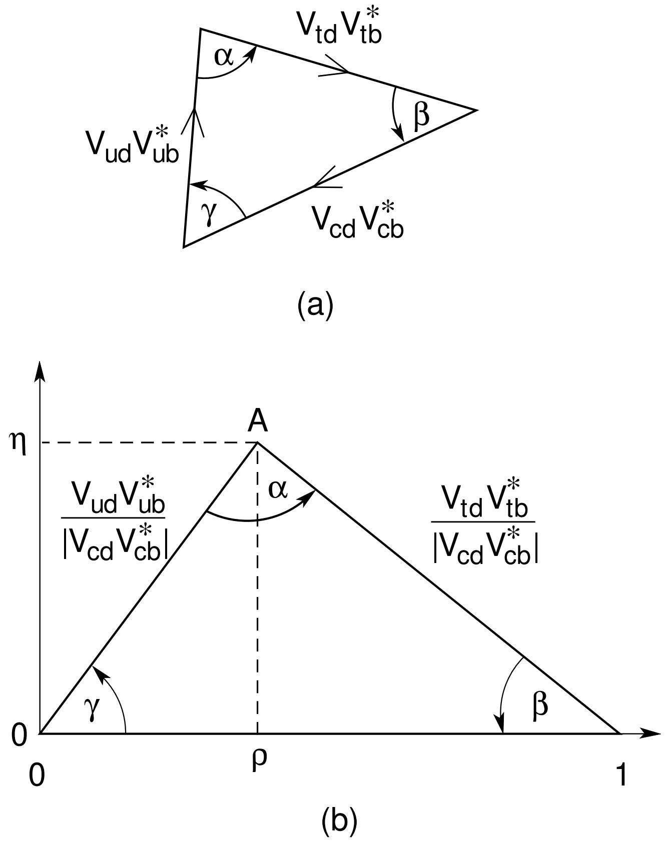

Figure 2.1: The Unitarity Triangle arising from equation 2.8: (a) unscaled and (b) with all sides divided by $|V_{cd}V_{cb}^*|$.

Triangle parameters [19] are consistent with the Standard Model.

2.1.2 Extensions to the Standard Model

In spite of the success of the Standard Model, it does not provide a complete description of nature. It fails to unify the fundamental forces, accommodate the force of gravity, predict masses of leptons or quarks, predict the CKM matrix elements, and does not explain the matter-antimatter asymmetry observed in the universe. Particle physicists aim to find something that disagrees with a prediction based on the Standard Model, or to discover entirely new particles or effects.

Two theoretical predictions of particles yet to be observed are introduced below. Their existence is expected to influence the decay rate of $b \to s\gamma$ as explained in section 2.2.

The Higgs Boson

The observed low rates for weak interactions indicate that the weak bosons exchanged must be massive. Adding mass terms for the bosons to a Lagrangian which describes the interaction, breaks gauge invariance and results in a unrenormalizable theory. The Higgs mechanism [13] generates the particle masses in a gauge invariant way by spontaneously breaking the gauge symmetry. Electroweak interactions are described by the $SU(2)_L \otimes U(1)_Y$ group, where $SU(2)$ refers to weak isospin and $SU(1)$ to weak hypercharge. This symmetry, which assumes zero mass for all particles, is spontaneously broken through particle interactions with an additional field, called the Higgs field. The Higgs field is an isospin doublet of complex scalar fields, and has a non-zero vacuum expectation value which is chosen to break both the $SU(2)$ and $SU(1)$ gauge symmetries. The weak bosons Z, W^+ and W^- acquire mass through interaction with the Higgs field, but as the vacuum state is invariant under the $U(1)_{EM}$ transformation, γ remains massless. Masses are also generated for leptons and quarks through the Higgs mechanism. Their values are only parameters of the theory and cannot be predicted.

Since all fields in quantum mechanics have particles associated with them, a particle must exist for the Higgs field: the Higgs boson. As the Higgs particle interacts with its own field it acquires mass, although its mass cannot be predicted by the theory. Proposed extensions to the SM suggest there are up to two Higgs-doublets with both neutral and charged Higgs bosons, although none have yet been discovered. The theory predicts that the coupling of the Higgs to fermions is directly in proportion to their masses, which can be tested when, and if, the Higgs is observed. This idea makes the Higgs a difficult particle to discover. The most readily experimental accessible particles are light fermions (e^-, and u, d quarks in protons and neutrons) which couple very weakly to the Higgs. The t quark couples the most readily to the Higgs but is more difficult to produce.

Supersymmetry

Supersymmetry [20] (SUSY) is a proposed symmetry which directly links spin-1/2 matter fields with spin-1 gauge boson fields. In this theory a super-partner exists for each fundamental particle which is identical to the particle except for its spin. SM fermions (quarks and leptons) each acquire a bosonic partner (squarks and sleptons), and SM bosons are assigned fermionic partners (with the same names as the bosons, but with the suffix "ino" attached, e.g. gluino, wino). There are no spin-distinctions for the particle-superpartner pairs.

SUSY solves several problems that exist in the Standard Model. An example is the Higgs "naturalness" problem, where corrections from fermion-antifermion loops result in a divergent Higgs mass. According to the theory of Supersymmetry, for every fermion-antifermion loop there exists a sfermion-antisfermion loop. Since the spins of particles in the two loops differ, their associated amplitudes have opposite signs and so almost cancel each other out. SUSY also solves the hierachy problem of why the electroweak scale (several hundred GeV), and the scale of unification of all forces (called the Planck scale $\sim 10^{19}$) are so different. In addition, it can encompass the spin-2 fields of Einstein gravity, the gravitons.

As there is no direct experimental evidence for super-partners to any of the measured SM particles, Supersymmetry cannot be an exact symmetry. If the symmetry is broken, then SUSY particles may have much greater masses than ordinary particles, hence maybe explaining why they have not been observed to date.

2.2 The $b \to s\gamma$ Decay

The unitary condition of the CKM matrix forbids the tree-level decay of a b quark to a s quark through direct Z emission. Beyond single vertex diagrams, we find that the b quark can decay to an s quark through the emission and re-absorption of a W boson. This is known as a "one loop flavour changing neutral current" (FCNC) process or, more commonly, a "penguin" process.

Figure 2.2 shows a Feynman diagram for the $b \to s\gamma$ transition. The intermediate quark may either be a t, c or u, and the photon can be emitted from any of the charged particles. The other quark in the B meson is referred to as a spectator quark as it does not participate directly in the decay, only in the fragmentation of the final hadronic system.

Penguin processes are of high interest as they are potentially sensitive to new physics. New high-mass virtual particles may enter the loop and contribute to the decay amplitude, thus raising or lowering the rate predicted by the Standard Model. For instance, a charged Higgs may be present in the loop instead of the W boson, or both particles in the loop

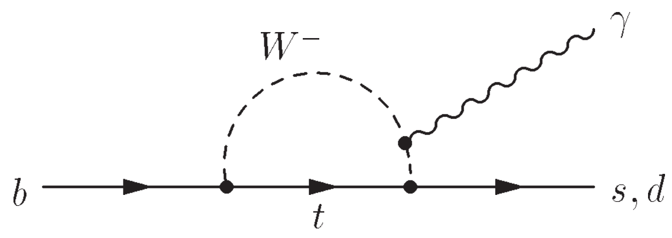

Figure 2.2: A leading order Feynman diagram for the radiative penguin $b \to s\gamma$ transition.

may be replaced by their SUSY particles, a wino and a squark. The measured decay rate for $b \to s\gamma$ can either suggest that new physics exists, or provide tight constraints on theoretical extensions of the Standard Model [21, 22]. In addition, the energy spectrum of the photon from $b \to s\gamma$ decays provides information on the mass, m_b, and Fermi momentum of the b quark inside the B meson. These parameters can be used to in conjunction with measurements of $B \to X_u l\nu$ to determine the CKM matrix element V_{ub} [23].

2.3 The $B \to X_s\gamma$ Branching Fraction

As quarks do not exist freely, the $b \to s\gamma$ branching fraction cannot be measured experimentally at the quark level. Instead, since the final state quarks hadronize, it is appropriate to measure the branching fraction of a B meson decaying to all final states containing a strange quark and a hard photon (denoted $\mathcal{B}(B \to X_s\gamma)$). Such decays are called "inclusive", to be distinguished from exclusive decays to a specific hadron state.

The full next-to-leading order (NLO) Standard Model calculation for the $B \to X_s\gamma$ branching fraction has been performed [3, 21, 22, 24]. It uses the fact that the energy released by the b quark into the final state is much larger than the QCD scale (Λ_{QCD}). This means that the final hadronic state need not be dominated by a few sharp resonances, and is instead mostly non-resonant, represented by a smooth hadronic mass spectrum. As resonances are unimportant, the QCD short-distance decay of the b quark can be factored from the subsequent long-distance fragmentation and hadronization of the decay products. This factorization is known as "parton-hadron duality", and it is used to predict the inclusive rate for $B \to X_s\gamma$ from the parton level decay rate $b \to s\gamma$.

The parton level calculation is performed perturbatively as:

$$\Gamma[b \to X_s^{parton}\gamma] = \Gamma[b \to s\gamma] + \Gamma[b \to s\gamma g] + ... \tag{2.9}$$

where the contribution from higher-order diagrams is the dominant uncertainty. The NLO terms are calculated [22] in a framework based on Operator Product Expansions (OPE), with an effective Lagrangian given by:

$$\mathcal{L}_{eff} = \mathcal{L}_{QCD\times QED}(u,d,s,c,b) + \frac{4G_F}{\sqrt{2}}V_{ts}^*V_{tb}\sum_{i=8}^{8} C_i 0_i + ... \tag{2.10}$$

where G_F is the weak coupling constant, V_{ts} and V_{tb} are CKM elements, O_i are operators and C_i are the Wilson coefficients [3, 22, 25]. The OPE works in a similar way to Fermi theory. For intermediate particles with masses exceeding m_b (i.e. t and W), the weak decay loop is contracted to a point like vertex. The operators O_i represent all possible structures of effective currents which arise when the vertex is collapsed. The Wilson coefficients C_i play the role of coupling constants at the vertex and parameterize the short-distance QCD effects arising from hard gluon exchange between the quark lines. Such effects enhance the $B \to X_s\gamma$ branching fraction by roughly a factor of three [26].

The SM prediction for the $B \to X_s\gamma$ branching fraction is determined from the theoretical decay rate for $B \to X_s\gamma$, $B \to X_c e\overline{\nu}$, and $B \to X_u e\overline{\nu}$, and the measured branching fraction for $B \to X_c e\overline{\nu}$:

$$\begin{aligned}\mathcal{B}[B \to X_s\gamma] &= \mathcal{B}[B \to X_c e\overline{\nu}]_{exp}\left(\frac{\Gamma[B \to X_u e\overline{\nu}]}{\Gamma[B \to X_c e\overline{\nu}]}\right)_{th}\left(\frac{\Gamma[B \to X_s\gamma]}{\Gamma[B \to X_u e\overline{\nu}]}\right)_{th}\\ &\backsimeq \mathcal{B}[B \to X_c e\overline{\nu}]_{exp}\left(\frac{\Gamma[b \to X_u^{parton} e\overline{\nu}]}{\Gamma[b \to X_c^{parton} e\overline{\nu}]}\right)_{NNLO}\left(\frac{\Gamma[b \to X_s^{parton}\gamma]}{\Gamma[b \to X_u^{parton} e\overline{\nu}]}\right)_{NLO}\\ &\qquad + (\text{non perturbative corrections})\end{aligned} \tag{2.11}$$

The ratios are introduced to minimize uncertainties that arise from the CKM matrix elements and the dependence on m_b. The non-perturbative corrections are calculated using operator product expansions in the framework of Heavy Quark Effective Theory (HQET) [27]. These corrections are small (of order Λ_{QCD}^2/m_b^2), but introduce dependence of the final rate on the HQET parameters: m_b, λ_1 which represents the kinetic energy of the b quark inside the B meson, and λ_2 which represents the mass difference between B and B^* mesons.

The most complete NLO calculation for the branching fraction to date [3] yields the prediction:

$$\mathcal{B}(B \to X_s\gamma)_{E_\gamma > 1.6\,\mathrm{GeV}} = (3.57 \pm 0.30) \times 10^{-4} \tag{2.12}$$

It is computed for an integral over $E_\gamma > 1.6\,\mathrm{GeV}$ in the B rest frame. This cutoff is chosen to avoid difficult non-perturbative effects at low E_γ, without introducing theoretical uncertainties associated with the E_γ spectrum at higher E_γ. Normalizing the result to the full E_γ spectrum gives a central value of:

$$\mathcal{B}(B \to X_s\gamma) = 3.70 \times 10^{-4} \tag{2.13}$$

Reference [21] presents a result that is about 11% smaller, largely due to the choice of c quark mass used to calculate the charm loop contributions. It uses the pole mass scheme for m_c whereas the $\overline{MS}$ scheme is currently preferred [22]. The correct choice of renormalization scheme for m_c and m_b is a NNLO issue that can only be resolved at the three-loop level. The NNLO calculation is currently underway [28] to solve this problem and decrease the uncertainty arising from higher order diagrams in the expansion.

2.4 The Signal Model for $B \to X_s\gamma$

The shape of the photon energy spectrum is not sensitive to new physics, however it still provides useful information. The predicted spectrum depends on the HQET parameters m_b and λ_1 as described in [29]. These parameters can be extracted from the experimentally measured photon spectrum. This procedure is not carried out in this analysis at present as more statistics are required to accurately measure the shape of the photon energy spectrum.

Without the strong force, the decay products from $b \to s\gamma$ would each be observed with momenta of about $\mathrm{m_b}/2$. In reality, the strong force causes the b quark to be confined into a B meson, and the s quark to fragment into a spectrum of K^* resonances. The b quark interacts with the spectator quark in the meson giving a scale dependence in m_b, and it also has Fermi momentum from its confinement. As a result, the energy spectrum is smeared such that $< E_\gamma > \approx\ m_b/2$ and the width is related to the Fermi momentum, p_F, of the b quark.

The predicted spectral shape is based on a description of the b quark motion. HQET incorporates this so-called "Fermi motion" by a resummation of an infinite set of corrections into a shape function describing the quark momentum distribution. This shape function is a characteristic of the inclusive decay spectra of the B meson, for all processes with light-mass final state partons. It is defined:

$$F(y') = N(1 - y'/\overline{\Lambda})^a e^{(1+a)y'/\overline{\Lambda}} \tag{2.14}$$

where $y' = y\,\mathrm{m_B}/\,\mathrm{m_b}$, $y = 2E_\gamma/m_b$, N is the normalization, $\overline{\Lambda} \approx m_B - m_b$, and a is related to the kinetic energy of the b quark inside the meson, μ_π^2 $(= -\lambda_1)$, by:

$$\mu_\pi^2/3 = \overline{\Lambda}^2/(1+a) \tag{2.15}$$

To obtain the $B \to X_s\gamma$ photon energy spectrum the shape function is convoluted with the parton-level energy spectrum, $P(y)$ where $0 \leq y \leq 1$. The calculation has been carried out by Kagan and Neubert [21] and their result is used as the signal model in this analysis.

The photon energy spectrum in the B meson rest frame is equivalent to the X_s hadronic mass spectrum through the kinematic relation:

$$E_\gamma = \frac{\mathrm{m_B^2} - \mathrm{m_{X_s}^2}}{2m_B} \tag{2.16}$$

The E_γ spectral shape predicted by Kagan and Neubert corresponds to a smooth hadronic mass spectrum. This distribution is a good representation of the resonant and non-resonant modes that make up the X_s system as the resonances are closely spaced and wide enough to overlap (see table 2.2). The only exception is the narrow $K^*(892)$ peak which stands alone, separated from the other resonances. Kagan and Neubert prescribe that the smooth m_{X_s} spectrum should be modified in the $K^*(892)$ region. Below a chosen $m_{X_s}^{cut-off}$ their spectral function is replaced with a single Briet-Wigner peak for the $K^*(892)$ resonance, normalized to equal the same fraction of the total spectrum. This is illustrated in figure 2.3(b). The value of $m_{X_s}^{cut-off}$ is determined such that the fraction replaced with $K^*(892)$ equals the ratio of the average experimental results for $B \to K^*\gamma$ and $B \to X_s\gamma$.

State X_s	m_{X_s} (GeV/c^2)	Γ_{X_s}(MeV/c^2)	E_γ (GeV)
$K(n\pi)$	≥ 0.629	continuum	≤ 2.60
$K^*(892)$	0.894	50	2.56 ± 0.01
$K_1(1270)$	1.273	90	2.49 ± 0.02
$K_1(1400)$	1.402	174	2.45 ± 0.05
$K^*(1410)$	1.412	227	2.45 ± 0.06
$K_2^*(1430)$	1.428	103	2.45 ± 0.03
$K_2(1580)$	1.580	110	2.40 ± 0.03
$K_1(1650)$	1.650	150	2.38 ± 0.05
$K^*(1680)$	1.714	323	2.36 ± 0.10
$K_2(1770)$	1.773	186	2.34 ± 0.06

Table 2.2: The accessible resonances for the X_s system in the $B \to X_s\gamma$ decay. The mass, width and corresponding photon energy is given for each resonance.

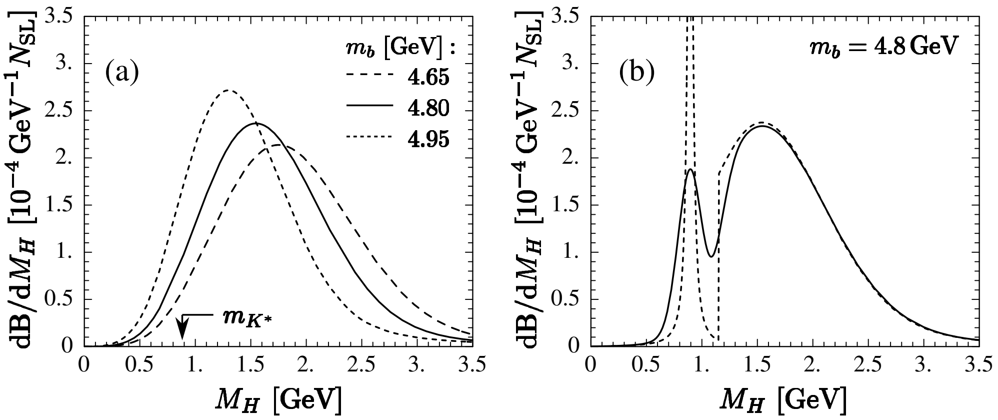

Figure 2.3: The Kagan and Neubert m_{X_s} spectra taken from [21] ($m_H = m_{X_s}$) (a) for different m_b choices and (b) modified to include the $K^*(892)$ resonance. In (b) the dashed curve shows the spectrum with an abrupt cut and the inclusion of the $K^*(892)$, and the solid curve shows the same distribution with an experimentally more realistic energy smearing of about $100\,\mathrm{MeV}$. $N_{SL} = B(B \to X_c e\overline{\nu})/10.5\%$ and is determined from experiment to be ~ 1.

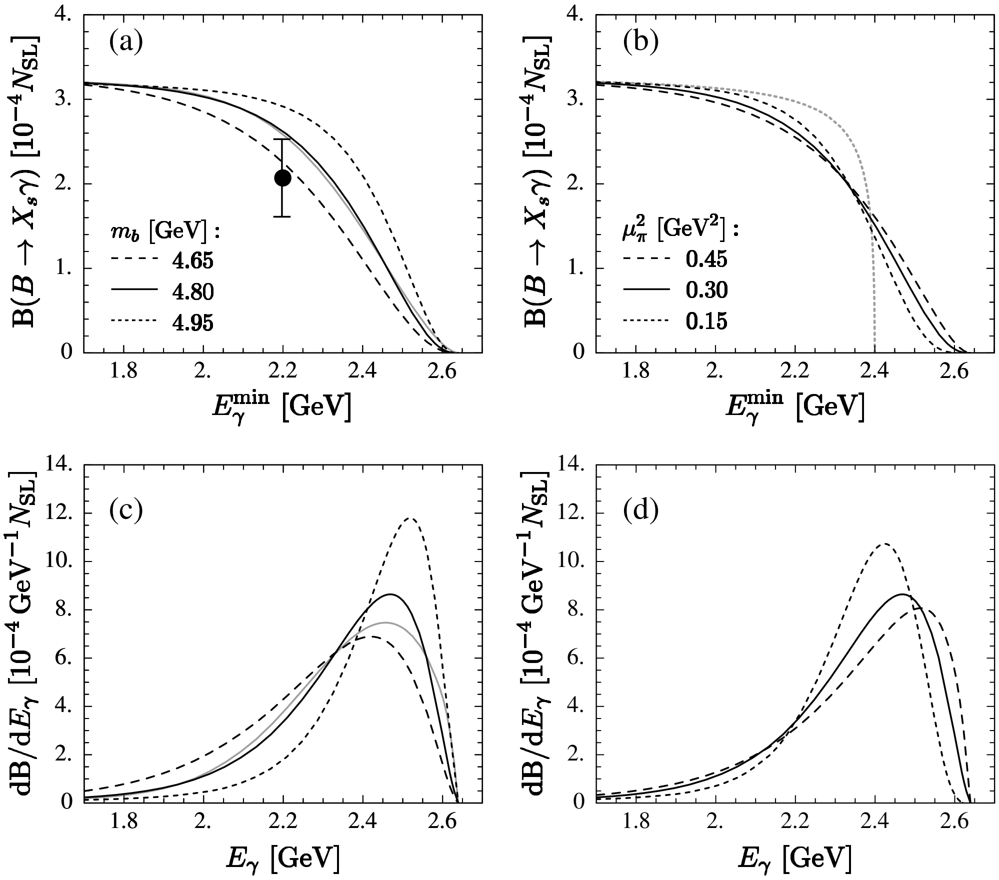

Figure 2.4: The model dependence of the E_γ spectrum in the B rest frame, taken from [21]. (a) and (b) show the integrals of the spectra ($\mathcal{B}(B \to X_s\gamma)$) as a function of the lower bound of integration E_γ^{min}, for different input values of m_b and μ_π^2 respectively. (c) and (d) show the spectra (d$\mathcal{B}$/dE_γ), for the same choices of m_b and μ_π^2. The grey lines show the spectra obtained with a Gaussian ansatz for the shape function and the data point represents the first CLEO measurement. $N_{SL} = B(B \to X_c e\overline{\nu})/10.5\%$ and is determined from experiment to be ~ 1.

The E_γ spectrum is dependent on two parameters, m_b and μ_π^2. The lower plots of figure 2.4 show the spectral shape for different choices of these parameters. The dependence on m_b is found to be much stronger than on μ_π^2, and so to evaluate the model dependence Kagan and Neubert suggest that m_b should be varied between 4.65 and 4.95 GeV/c^2 whilst keeping $\mu_\pi/\overline{\Lambda}$ constant. This procedure is used to obtain the theoretical uncertainty for the branching fraction measurement which arises from its dependence on the model used to simulate signal events (see section 7.7). To obtain the branching fraction result, the values of the model parameters used for the signal simulation are: $m_b = 4.80\,\mathrm{GeV}/c^2$, $\mu_\pi^2 = 0.30\,\mathrm{GeV}^2$, $m_B = 5.2788\,\mathrm{GeV}/c^2$ and $m_{X_s}^{cut-off} = 1.02\,\mathrm{GeV}/c^2$.

The photon energy spectrum is model-dependent, whereas the $B \to X_s\gamma$ branching fraction is much better understood theoretically. The total branching fraction is determined from the integral of the E_γ spectrum over the entire kinematic range. Hence, an ideal measurement would have uniform selection efficiency across the spectrum with no requirements on the photon energy. Due to the large background present at low E_γ, photons from $B \to X_s\gamma$ decays can only be selected above an E_γ^{min} threshold. To obtain the total branching fraction, the signal model is used to extrapolate the measured E_γ spectrum into the unmeasured region. Figure 2.4 illustrates that the model dependence is increased as the E_γ^{min} threshold is raised. It is therefore important to keep the E_γ^{min} threshold as low as possible to avoid incurring a large theoretical uncertainty on the total branching fraction. Suppressing the background as much as possible in order to extract signal events at low E_γ is the main objective for all experimental $B \to X_s\gamma$ branching fraction analyses.

2.5 Summary

The Standard Model described in this chapter is an extremely successful description of nature, but at present it is known to be incomplete. The Higgs Boson is expected to exist within the framework of the Standard Model, but to date this has not been detected. Proposed extensions to the Standard Model also predict the existence of additional fundamental particles to those observed. The $b \to s\gamma$ penguin transistion is sensitive to such new physics as these particles may exist in the loop mediating the transition and contribute to the decay rate. The theoretical NLO calculation of the $B \to X_s\gamma$ branching fraction based on the Standard Model has been discussed in this chapter. All current measurements (see section 1.1) agree with this prediction. This result can be used to provide constraints on proposed theories of new particles, hence it is important to improve the precision of both theoretical and experimental results to further test the agreement.

The integral of the $B \to X_s\gamma$ photon energy spectrum is used to obtain the branching fraction result. The shape of this spectrum, although insensitive to new physics, does depend on the HQET parameters, m_b (the b quark mass) and λ_1 (the kinetic energy of the b quark inside the meson). These parameters can be extracted from a measurement of the spectral shape, and used with measurements of $B \to X_u l\nu$ to determine the CKM matrix element V_{ub}. The $b \to s\gamma$ transition is therefore of great theoretical importance.

Chapter 3

PEP-II and the *BABAR* Experiment

The *BABAR* detector is located in the interaction region of the PEP-II asymmetric e^+e^- storage ring at the Stanford Linear Accelerator Center (SLAC). PEP-II is a high luminosity B factory where electron and positron beams collide at the $\Upsilon(4S)$ resonance to produce pairs of $B\overline{B}$ mesons (both charged and neutral). The primary goal of the *BABAR* experiment is to investigate minute differences between the decay of B and $\overline{B}$ mesons and hence to better the understanding of the matter-antimatter asymmetry in nature by exploring the mechanism of CP violation (see section 2.1.1). Secondary goals of the experiment are to obtain precision measurements for decays of B and D mesons and τ leptons, to determine elements of the CKM matrix, and to search for rare decays. To achieve these aims a high integrated luminosity of data is necessary, as well as a detector capable of precise tracking, calorimetry and particle identification.

The data used for the analysis presented in this thesis consists of approximately 230 million $B\overline{B}$ decays recorded with the *BABAR* detector in the years 1999 to 2004. This chapter gives an overview of how these events were produced and collected. It contains a brief description of the accelerator and the different components of the *BABAR* detector. A more detailed description of these topics can be found in [30, 31, 32, 33]. Details of how the raw data collected are used to reconstruct and identify particles are given in section 3.3.

$e^+e^- \rightarrow$	Cross-Section (nb)
$b\overline{b}$	1.05
$c\overline{c}$	1.30
$u\overline{u}$,$d\overline{d}$,$s\overline{s}$	2.09
$\tau^+\tau^-$	0.94
$\mu^+\mu^-$	1.16
e^+e^-	$\sim$ 40

Table 3.1: Production cross sections at the $\Upsilon(4S)$ resonance, taken from [33]. The numbers quoted are effective cross-sections, expected within the experimental acceptance of the *BABAR* detector.

3.1 The PEP-II B Factory

The PEP-II B factory is an asymmetric e^+e^- collider that operates at a centre-of-mass energy of $10.58\,\mathrm{GeV}$. This energy corresponds to the mass of the $\Upsilon(4S)$ resonance, which decays almost exclusively to $B\overline{B}$ pairs. Other particles are also produced in these collisions. Table 3.1 shows the cross-sections to all possible final states produced at the $\Upsilon(4S)$ collision energy (on-resonance data). Approximately 10% of collisions are produced with a centre-of-mass energy $40\,\mathrm{MeV}$ below the $\Upsilon(4S)$ peak (off-resonance data). At this energy the production of B mesons is kinematically suppressed. All other particles are produced as before, thus providing a control sample of $e^+e^- \rightarrow u\overline{u}, d\overline{d}, s\overline{s}, c\overline{c}$ (continuum) events, and $\tau^+\tau^-$ events, that can be used to directly study this background.

The PEP-II B factory is called an "asymmetric" e^+e^- collider due to the unequal energies of the electron (9 GeV) and positron (3.1 GeV) beams. The centre-of-mass of the system produced by the collision is not at rest in the laboratory frame, but boosted with a Lorentz boost factor of $\beta\gamma = 0.56$ in the direction of the electron beam. This results in a spatial separation of $\sim 250\,\mu$m between the decay vertices of the two B mesons, from which their relative decay times can be determined. This enables time dependent CP violation measurements to be made [34].

Figure 3.1 shows a sketch of the PEP-II B factory. Electrons are produced with a polarized electron gun and accelerated in bunches down SLAC's 3km long linear accelerator (linac) by a series of klystrons. The klystrons produce microwaves that create oscillating electric and magnetic fields in the copper cavities of the linac. These oscillating fields are synchronized with the arrival of the bunches to provide the optimal acceleration. Some

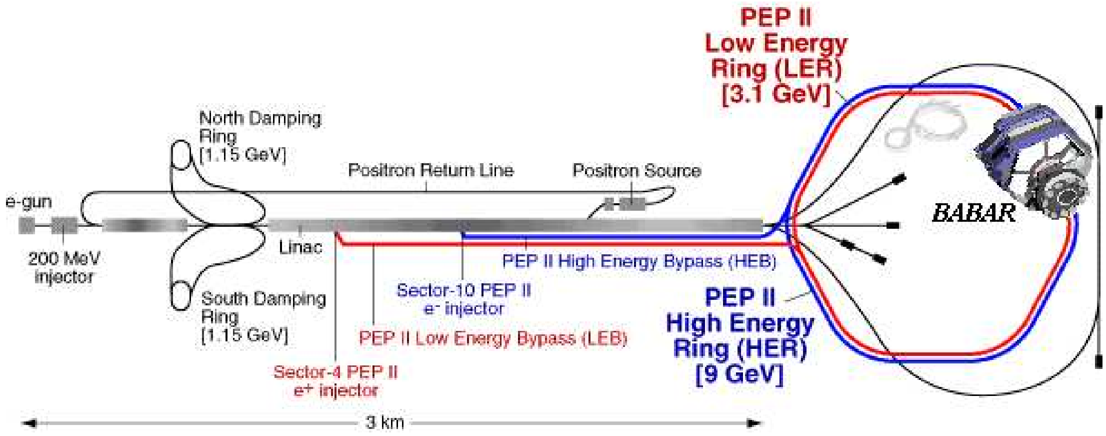

Figure 3.1: A detailed map of the PEP-II B factory.

electrons are diverted from the linac to collide with a tungsten target and produce e^+e^- pairs. The positrons are collected, and returned to the start of the linac where they are accelerated out of phase with the electrons.

The electrons and positrons reach energies of 9 GeV and 3.1 GeV respectively, and are then injected in opposite directions into the 800 m diameter PEP-II storage rings; a high energy ring (HER) for electrons, and low energy ring (LER) for positrons. The beams are stored in the rings until they reach the desired currents, and then are brought into a head-on collision at the interaction point. The *BABAR* detector wraps around this area to record the subsequent reactions. Its horizontal axis is off-set from the collision axis by about 20 mrad to minimize the pertubation of the beams by the detector's solenoidal field. Quadrupole and dipole magnets are used to focus the beams before the collision, and separate them afterwards to minimize beam-beam interactions.

PEP-II has achieved a peak luminosity of $9.21 \times 10^{33}\,\mathrm{cm}^{-2}\mathrm{s}^{-1}$ using 1558 bunches with currents of 1550mA in the HER and 2450mA in the LER. This exceeds the design luminosity of $3 \times 10^{33}\,\mathrm{cm}^{-2}\mathrm{s}^{-1}$. The success of PEP-II has enabled *BABAR* to collect an integrated luminosity of 244.1 fb^{-1} of data by the end of 2004, of which 210.5 fb^{-1} are used in this analysis.

3.2 The *BABAR* Detector

To achieve the goals of the experiment, the *BABAR* detector must satisfy several requirements:

- It must have a large angular acceptance region to collect as many of the decay fragments as possible. Due to the Lorentz boost of the decay products from a collision, optimizing the detector acceptance results in an asymmetric detector, with increased instrumentation in the forward (electron) direction.

- Excellent resolution is required for the transverse momentum* of charged tracks in the range $60\,\mathrm{MeV}/c < p_t < 4\,\mathrm{GeV}/c$, and for the energy of photons in the range $20\,\mathrm{MeV} < E < 5\,\mathrm{GeV}$. These particles must also be reconstructed with high efficiency.

- Excellent vertex resolution is needed to measure the decay time difference between B and $\overline{B}$ mesons. Vertex reconstruction must be particularly effective close to the electron beam axis, since the boost leads to most inital particles travelling in this region.

- Leptons (e, μ), and hadrons (K, π, p) over a wide momenta range must be identified accurately and efficiently, especially for the reconstruction of exclusive states, and for flavour-tagging B mesons [34].

The *BABAR* detector was designed to provide all the above features. It consists of a typical set of detector sub-systems arranged concentrically around the beampipe, as illustrated in figure 3.2. The charged particle tracking system is made up of two detectors; the silicon vertex tracker (SVT), and the drift chamber (DCH). A detector of internally reflected Cherenkov light (DIRC) is used to identify charged hadron particle types, and a CsI(Th) electromagnetic calorimeter is used for electron and photon detection. These sub-systems are placed inside a 1.5 Tesla solenoidal magnetic field, to deflect charged particles to enable momentum and charge determination. Finally, the solenoid is surrounded by an instrumented flux return (IFR) for muon and neutral hadron identification.

Each of the sub-systems of the *BABAR* detector, ordered from the inside out, are described in this section.

*The transverse momentum p_t is measured with respect to the longitudinal axis of the detector.

3.2.1 The *BABAR* Coordinate System

The z-axis of the detector points along the longitudinal axis of the drift chamber. This is slightly offset from the electron beam by 20 mrad (to minimize the perturbation of the beams caused by the solenoidal field.) The x-axis points horizontally away from the centre of the PEP-II rings, and the y-axis points upwards. The origin (0,0,0) is defined as the nominal interaction point (IP) of the collision. The whole detector is offset from this point by 0.37 m in the direction of the positron beam. This is to maximize the geometrical acceptance for the boosted $\Upsilon(4S)$ decays that travel in the forward (electron) direction.

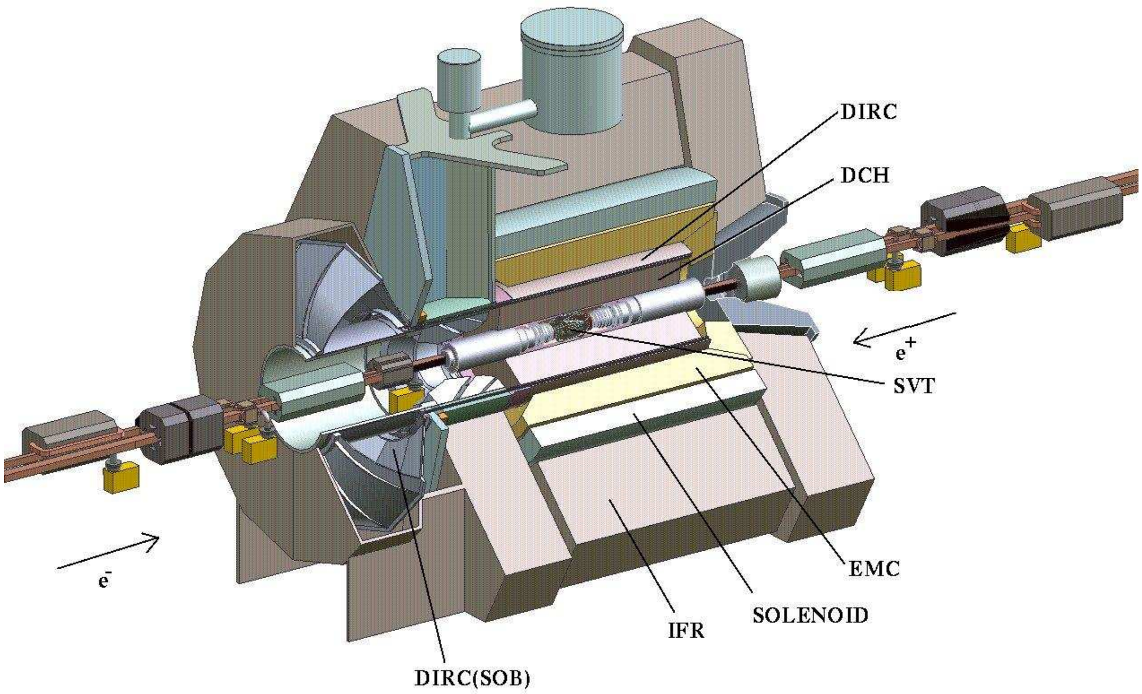

Figure 3.2: A three dimensional view of the *BABAR* detector showing all of its subsystems.

3.2.2 The Silicon Vertex Detector (SVT)

The Silicon Vertex Tracker (SVT) is designed to provide vertex information for the decay of short lived particles, and precision trajectory measurements for charged particles just outside the beam pipe. It is also the only tracking device for particles with insufficient transverse momentum ($p_t < 100\,\mathrm{MeV}/c$) to reach the DCH in the presence of the $1.5\,\mathrm{T}$ magnetic field. It consists of five concentric layers of double-sided silicon strip detectors. As a charged particle passes through the SVT it creates a signal in each silicon strip it encounters, enabling its trajectory to be determined. From measurements of the pulse shape for each hit, the ionization rate, $\mathrm{d}E/\mathrm{d}x$, is also determined and this can be used for particle identification.

Figure 3.3 shows the arrangement of the silicon strip layers in the SVT. The inner three layers are located as close as possible to the beam pipe to achieve the best resolution on the z position of the B meson decay vertices. They are each made up of six modules assembled in a straight line. The two outer layers are close together, but at much larger radii to obtain the coordinate and angle measurements needed to link tracks in the SVT to those in the DCH. They consist of 16 and 18 detector modules respectively which are arched to provide maximum coverage and the smallest possible angle of incidence. The strips on opposite sides of all modules are othogonal to each other, with those closest to the beam axis running perpendicular to it (to provide z-information), and the outer strips running parallel to the beam pipe (to provide ϕ-information).

The total active area of the SVT is 0.96 m^2, consisting of about 150 000 strip readout channels which cover 90% of the solid angle ($0.35 < \theta_{lab} < 2.62\,\mathrm{rad}$). The efficiency for a charged particle passing through this area to leave a single hit is 97%. For perpendicular tracks, the spatial hit resolution is $30 - 40\mu\mathrm{m}$ for the two outer layers and $10 - 15\mu\mathrm{m}$ for the three inner layers.

3.2.3 The Drift Chamber (DCH)

The Drift Chamber (DCH) is the main tracking system for measurements of the momenta and angles of charged particles. Its longitudinal section is shown in figure 3.4.

The chamber contains 40 radial layers of hexagonal drift cells which provide up to 40 measurements of spatial coordinates and ionization loss per track. The layers are grouped into 10 superlayers, with sequential layers staggered by half a cell, as shown in figure 3.5. This enables left-right ambiguity resolution within each superlayer, even if one of the four signals is missing. Each cell contains one sense wire with an applied potential of 1960V, surrounded by six field wires kept at ground potential. To obtain longitudinal position information, the wires in six of the superlayers are positioned with

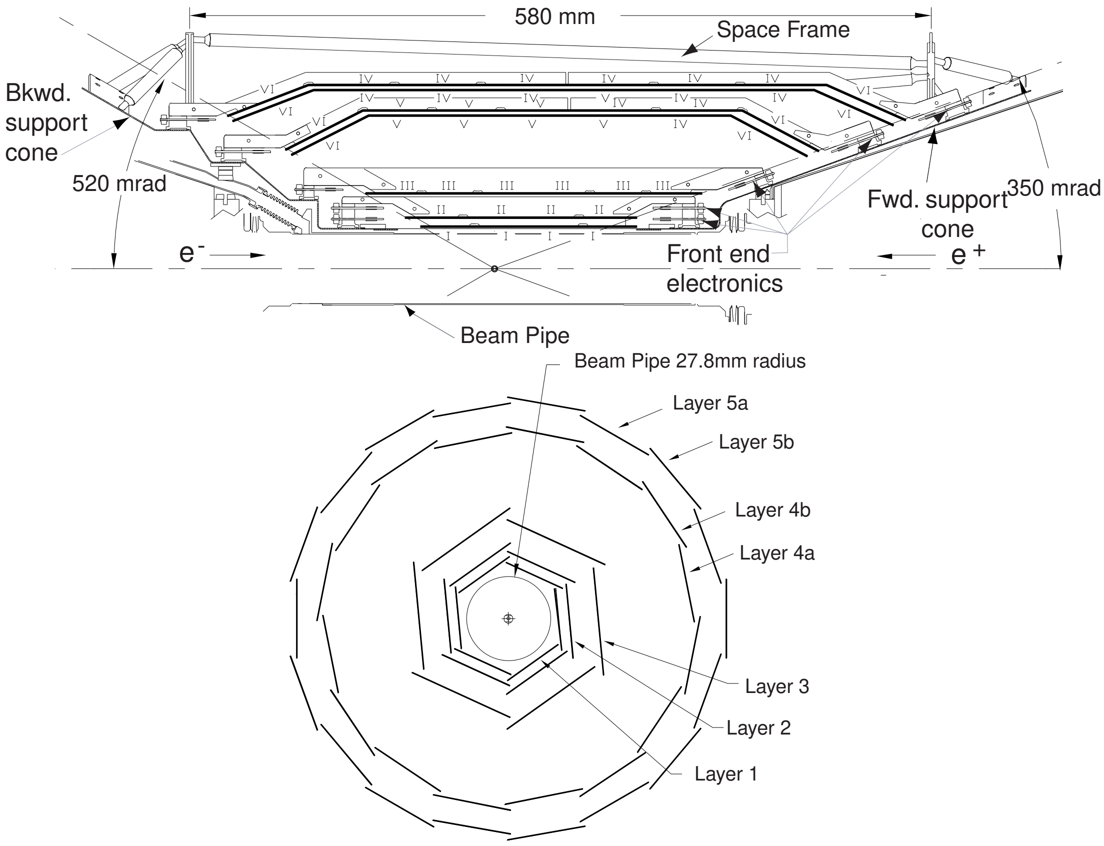

Figure 3.3: The longitudinal and cross sectional view of the SVT.

various slight tilts towards the z-axis, increasing with radii from ± 45 to ± 76 mrad. The readout electronics are located at the backward endplate of the chamber to minimize the material in the forward region, since this is the direction favoured by the boosted $\Upsilon(4S)$ decay particles.

The chamber is filled with an 80:20 helium:isobutane gas mixture, which helps reduce multiple scattering. A DCH hit is produced when a charged particle passes through a drift cell, ionizing the gas in its immediate vicinity. This creates a pulse of charge which is collected by the sense wire. The charge collected in the cells crossed, enables the trajectory of the track to be measured, as well as its ionization loss, $\mathrm{d}E/\mathrm{d}x$, which is used for particle identification. The position resolution of the DCH for tracks at medium drift distances (about 5mm), is approximately 100 μm in the transverse plane and 1 mm in the z-direction. The momentum of tracks in the DCH is limited to $100\,\mathrm{MeV}/c$ by the inner radius of the chamber.

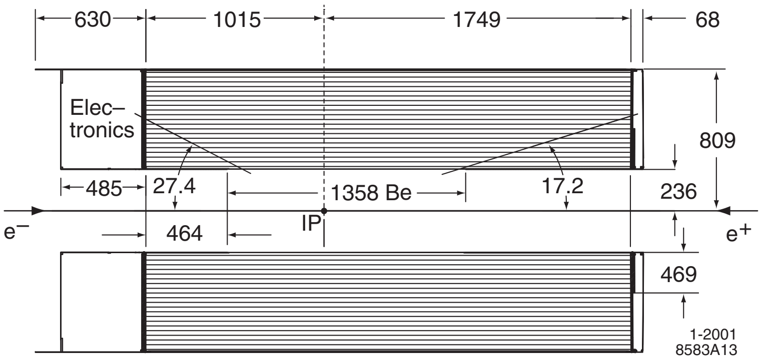

Figure 3.4: The longitudinal section of the DCH. All dimensions are given in mm.

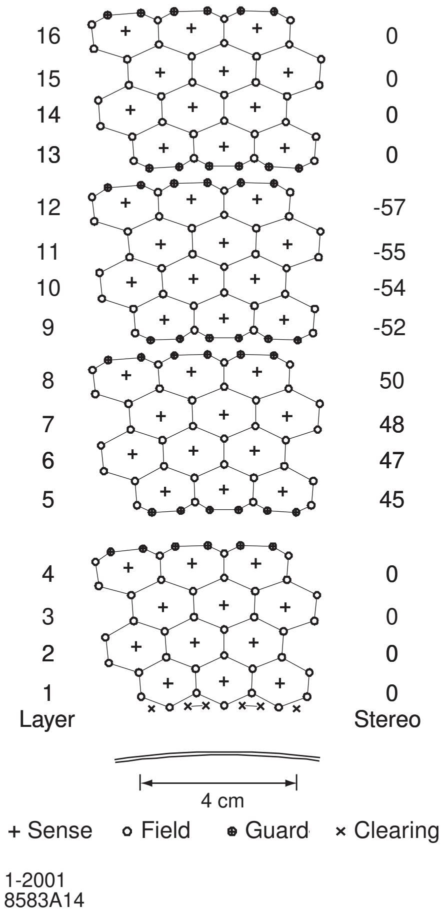

Figure 3.5: The layout of the drift cells for the four innermost superlayers of the DCH.

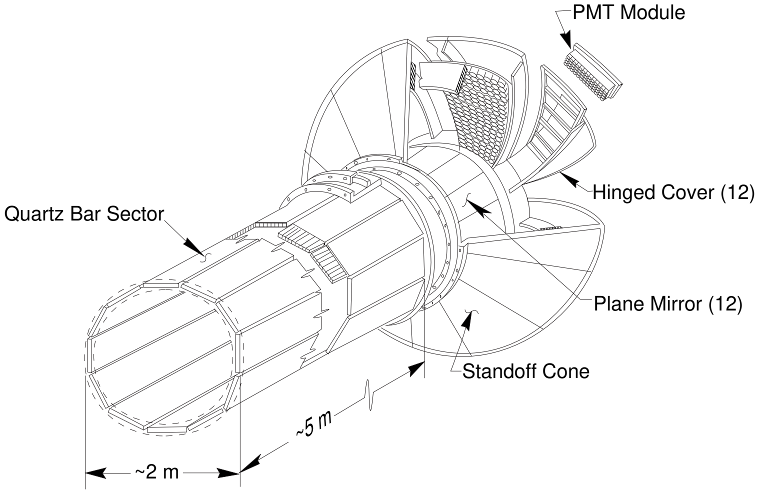

Figure 3.6: The geometrical structure of the DIRC system.

3.2.4 The Cherenkov Light Detector (DIRC)

The Detector for Internally Reflected Cherenkov Radiation (DIRC) is used for particle identification, in particular for separating pions from kaons. The DIRC exploits the principle that charged particles emit Cherenkov light when passing through a medium, if their velocity $\beta = p/E$ is larger than the speed of light in the medium or equivalently $\beta > 1/n$ where n is the refractive index of the medium. The angle of emission with respect to the particle direction is given by $\cos\theta_C = 1/\beta n$. Since one particle typically produces many Cherenkov photons, a light cone is observed. From measuring the opening angle θ_C of the cone, the speed of the particle can be determined. Combining this information with the track angle and momentum measurements from the DCH, allows determination of the particle mass, and hence its type. The information from the DIRC is used in particle identification as explained in section 3.3.2.

Figure 3.6 shows the geometrical structure of the DIRC. It consists of 144 bars of synthetic fused silica quartz with refractive index $n = 1.473$, arranged in a 12-sided polygonal barrel. When a charged particle passes through the quartz, the Cherenkov light emitted is totally internally reflected inside the bars. All photons arriving at the forward end are relected with a mirror, so only the backward end of the bars are instrumented. At this end the photons enter a standoff box filled with purified water. The refractive index of the water is $n = 1.346$, close to that of the quartz bars, to reduce internal reflection at the interface. At the back wall of the water chamber are an array of 10752 densely packed

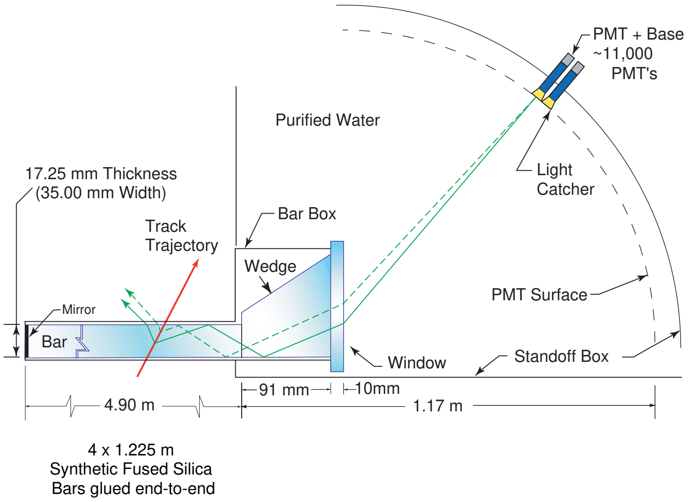

Figure 3.7: A diagram showing the quartz to water to PMT transition of Cherenkov photons inside the DIRC.

photomultiplier tubes (PMTs) to detect the Cherenkov light pattern. A typical photon path through the quartz bars and standoff box into the PMTs is shown in figure 3.7.

The DIRC imaging uses 3-dimensional position information and the arrival time of the signal, to associate the conic image with a DCH trajectory of a crossing particle. For di-muon events, the resolution on the Cherenkov angle is typically 10.2 mrad, and the arrival time resolution is about 1.7 ns.

3.2.5 The Electromagnetic Calorimeter (EMC)

The Electromagnetic Calorimeter (EMC) is designed to measure electromagnetic showers with high precision over a wide energy range; 20 MeV to the kinematic limit of 9 GeV. This sub-system is particularly important for an inclusive measurement of the $B \to X_s\gamma$ branching fraction which is obtained from the energy spectrum of high energetic photons $(1.9 - 2.7\,\mathrm{GeV})$. The four-momentum for photons is entirely determined from EMC measurements, and so excellent energy and angular resolution are necessary. The EMC also measures energy deposits from charged particles and neutral hadrons, and the shape of the electromagnetic showers can be used for particle identification.

The EMC is composed of 6580 Thallium-doped CsI crystals. 57600 crystals are arranged in 48 identical rings in a cylindrical barrel, and the rest are located in 8 rings in a conical forward endcap, as shown in figure 3.8. The system covers the polar angle region

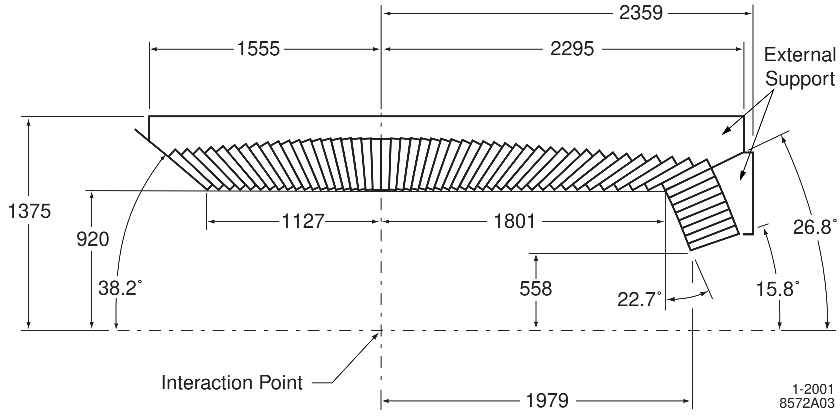

Figure 3.8: A longitudinal cross section of the top half of the EMC, showing the arrangement of the 56 crystal rings. All dimensions are given in mm.

$0.277 < \theta_{lab} < 2.456$ rad, resulting in a 90% coverage of the solid angle.

The crystals have tapered trapezoidal longitudinal cross sections that increase in length from 29.6 cm in the backward region to 32.4 cm in the forward direction to avoid shower leakage where higher energy particles are expected. When a charged particle passes through a crystal it deposits energy, initiating a shower of particles. The shower is eventually absorbed, causing the crystal to scintillate. Each crystal has two silicon pin diodes to detect the scintillation light which is directly proportional to the energy deposited.

Typically, a particle deposits its energy in a number of adjacent crystals called a "cluster". Clusters are required to contain at least one crystal with an energy deposit $> 10\,\mathrm{MeV}$, and adjacent crystals are included if they have deposits $> 1\,\mathrm{MeV}$, or if they neighbour a crystal with a deposit $> 3\,\mathrm{MeV}$. The total energy of a cluster must exceed $20\,\mathrm{MeV}$. The cluster's centroid is determined using a logarithmic centre-of-gravity method. Trajectories of charged particles are projected from the DCH to the face of the EMC, and if their impact point is consistent with a cluster centroid, the track is matched to that cluster. All unmatched clusters are defined to be neutral.

The angular resolution of the EMC is determined by the transverse crystal size, and the distance from the interaction point. It is also energy dependent, as shown in figure 3.9(a) for a π^0 sample. It is parametrized as:

$$\sigma_\theta = \sigma_\phi = \frac{(3.9 \pm 0.1)\mathrm{mrad}}{\sqrt{\mathrm{E}(\,\mathrm{GeV})}} + (0.0 \pm 0.04)\mathrm{mrad} \tag{3.1}$$

Calibration of the EMC

It is important to set the energy scale of the calorimeter with high precision and to determine any short or long-term changes in its response. The following calibration procedures are carried out regularly to ensure this:

- A charge injection system linearizes the response of the front-end electronics to better than 0.1%.

- Since the light yield varies considerably between crystals, and changes over time due to radiation damage, the energy scale is calibrated for individual crystals. Furthermore, as the absorbed radiation dose is non-uniform along the crystal axis, the calibration is performed at different energies, corresponding to different shower penetrations. At low energies, an absolute calibration is carried out by flushing the aluminium tubes in front of the crystals with a liquid radioactive source that emits 6.1 MeV test photons. This method results in a precision of 0.5% for the energy scale of individual crystals. At higher energies (3-9 GeV), the calibration is performed with a sample of Bhabha events. The energy deposited as a function of polar angle of the e^+e^-, is constrained to match simulated predictions, resulting in a precision of 0.4%.

- To determine the energy of the incident particle, the energy deposited in a cluster must be corrected for energy losses due to shower leakage and absorption in the material between and in front of the crystals. The correction is obtained as a function of the cluster energy and polar angle. For cluster energies below 800 MeV, the correction is derived from π^0 decays, where the reconstructed π^0 mass is compared to the π^0 nominal mass. Corrections of the order 5% are applied to cluster deposits. At higher energies, the correction is estimated from single photon simulation, and also from radiative Bhabha events where the e^+ and e^- momenta and the photon direction constrain the photon energy. Typical corrections are again about 5%.

Figure 3.9(b) shows the cluster energy resolution of the EMC measured from different samples. At low energy (6.13 MeV), the energy resolution is obtained with the same radioactive source that is used in calibration, yielding $\sigma_E/E = 5.0 \pm 0.8\%$. At high energy (7.5 GeV), the Bhabha measurements give $\sigma_E/E = 1.9 \pm 0.07\%$. A fit to the

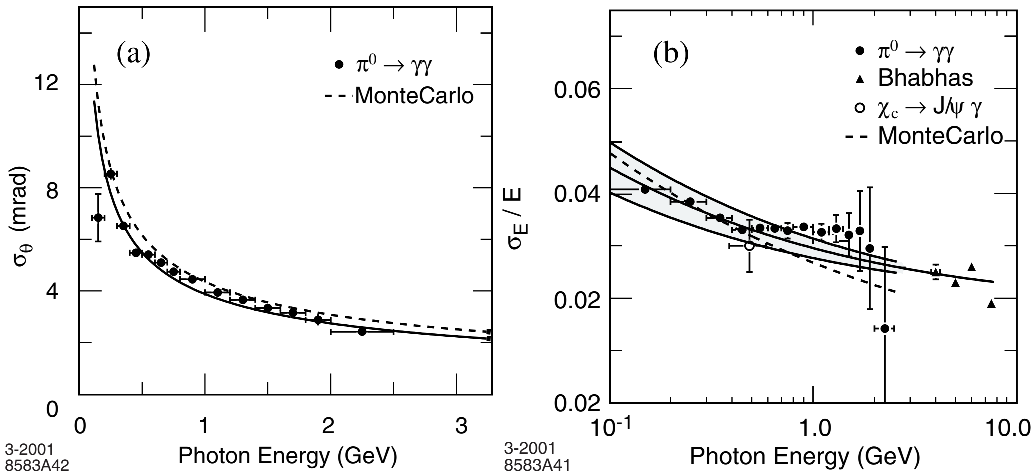

Figure 3.9: (a) The angular resolution of the EMC for photons from π^0 decays. The solid curve is a fit to equation 3.1. (b) The energy resolution measured for photons and electrons from various processes. The solid central curve is a fit to equation 3.2, and the outer curves denote the error of the fit [32].

energy dependence results in an energy resolution given by:

$$\frac{\sigma_E}{E} = \frac{(2.3 \pm 0.3)\%}{\sqrt[4]{E(\,\mathrm{GeV})}} \oplus (1.9 \pm 0.1)\% \tag{3.2}$$

For high energy photons in the range $1.9-2.7\,\mathrm{GeV}$, which are used to obtain the $B \to X_s\gamma$ branching fraction, the energy resolution is approximately 3%.

3.2.6 The Instrumented Flux Return (IFR)

The Instrumented Flux Return (IFR) is designed to identify muons, and to detect neutral hadrons over a wide range of momenta and angles. It uses the steel flux return of the magnet as a muon filter and hadron absorber. The steel is segmented, and Resistive Plate Chambers (RPCs) with two-coordinate readout are installed in the gaps. The RPCs are filled with a gas mixture of argon, freon and a small amount of isobutane. As a particle passes through the IFR it undergoes nuclear reactions in the steel bulk. Products from these interactions cause ionization in the RPC's gas chamber, which is detected by aluminium capacitive readout strips.

The IFR subdetector is shown in figure 3.10. It consists of a barrel section and forwarded and backward end doors that provide access to the inner parts of the detector. The

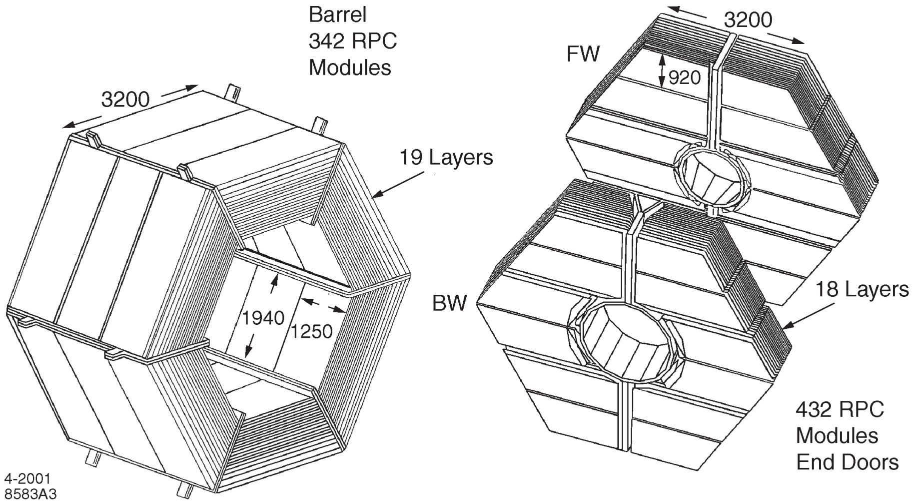

Figure 3.10: The barrel and forward (FW) and backward (BW) end doors of the IFR. The shape of the RPC modules and their dimensions in mm are shown.

segmented steel plates increase in thickness from 2 cm on the inner side of the IFR, to 10 cm on the outer, and are separated by 3.5 cm in the barrel and 3.2 cm elsewhere. This segmentation was chosen to optimize the detection of K_L^0 particles, which improves with finer segmentation. Since K_L^0 s typically interact within the first few layers only, a more cost-effective coarser segementation is used for the outer layers. There are 19 layers of planar RPCs installed in the barrel, and 18 layers in each of the end doors. In addition, two layers of cylindrical RPCs are installed between the EMC and the magnet to detect particles leaving the EMC.

In the barrel section, each RPC plane is divided into three modules. There are 32 read-out strips per module that are perpendicular to the beam axis to measure the z position, and 96 orthogonal strips to measure the position in ϕ. From longitudinal and transverse interaction patterns in the segmented steel, it is possible to determine if the particle is a muon or a hadron by its penetration depth. To identify neutral hadrons, a reconstruction algorithm identifies cluster deposits in the IFR. If the IFR clusters do not match any charged tracks extrapolated from the DCH, the hadron is assumed to be neutral.

3.2.7 The Trigger System

The *BABAR* trigger system handles the full beam-beam interaction rate, and decides which events should be kept for physics analysis. It is required to select a minimum of 99% of all $B\overline{B}$ events, 95% of continuum events and 90% of $\tau^+\tau^-$ events. It must be robust enough to operate in extreme background conditions, or with dead or noisy electronics, and should not contribute more than 1% to dead time.

The trigger system consists of two levels of filtering events: a hardware level 1 trigger (L1T) and a software level 3 trigger (L3T).

The L1T is designed purely to reduce background. The trigger decision is based on tracks in the DCH above a momentum threshold, showers in the EMC, and tracks detected by the IFR. Information from the SVT is not used in the decision as it cannot be processed fast enough. Each of the subsystems used generates summary data on the position and energy of particles known as "trigger primitives", and these are sent to a global trigger (GLT). The GLT processes all trigger primitives and decides which events to keep. This decision is made within 12 μs after the e^+e^- collision. The output rate of the L1T is less than 2 kHz, from an input PEP-II collision rate of 238 MHz.

The L3T performs a second stage reduction. It selects events which are of highest interest for physics, and reduces the rate of events to be stored permanently to less than 100 Hz. It also identifies and flags events needed for the luminosity determination, and for diagnostic and calibration purposes. The L3T software has access to the complete event data, including timing information, and filters on track parameters, cluster energies and event topologies. This information is combined to form more complex selection criteria for rejecting background events. The processing time per event for the L3T decision is approximately 4 ms.

3.3 Particle Reconstruction and Identification

This section describes how raw data collected by the detector sub-systems is used to reconstruct and identify particle types.

3.3.1 Reconstruction

The data used for physics analysis is stored in the form of track and neutral cluster objects.

A track is formed from the trail of hits detected in the SVT and DCH as a charged particle passes through. The single hits are combined into track segments by pattern recognition algorithms if their event times correspond. First, tracks are reconstructed from the DCH hits using algorithms which also consider tracks that do not pass through the entire DCH, or do not originate from the IP. These are then extrapolated into the SVT where suitable track segments are added. The Kalman filter method [35] is applied to the set of DCH and SVT hits for each possible track. This method takes into account local variations in the detector material and the magnetic field. Finally, an attempt is made to reconstruct tracks that are only found in one tracking system, and thus recover those scattered by the support material.

A cluster is defined as an isolated deposit of energy in the EMC. Pattern recognition algorithms are used to identify these, and to distinguish between single clusters with one energy maximum, and merged clusters with more than one local energy maximum (known as "bumps"). The algorithms also determine if a bump is generated by a charged or neutral particle by attempting to match its centroid with a charged track that is projected to the inner face of the calorimeter. All unmatched bumps are assumed to stem from photons, and angles and momenta are assigned to be consistent with photons originating from the interaction point. Pairs of photon candidates likely to originate from a π^0 are combined to reconstruct π^0 candidates (see section 4.2.1). To distinguish true photons from neutral hadrons which also deposit energy in the EMC, cluster shape variables are used (see section 5.1.2).

All tracks and neutral bumps used in this analysis are subjected to a set of selection criteria to ensure their quality. These requirements are described in section 5.1.

3.3.2 Identification

Particle identification is important in this analysis as it is used for the semi-exclusive reconstruction of the B meson. The various sub-detector systems provide information to distinguish between electrons, muons, kaons and pions.

- The SVT and DCH provide $\mathrm{d}E/\mathrm{d}x$ information. Figure 3.11 shows $\mathrm{d}E/\mathrm{d}x$ versus momentum in the DCH along with Bethe-Bloch predictions for different particle types.

- The DIRC measures the opening angle (θ_C) of a Cherenkov light cone, which is related to the speed of the charged particle (see section 3.2.4). Together with angle and momentum measurements from the DCH, this information is used for particle

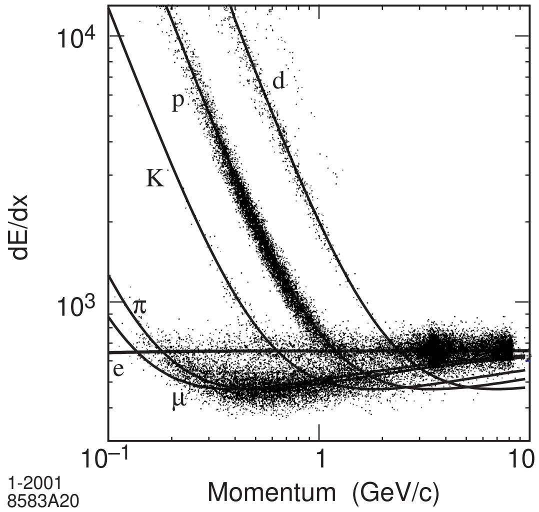

Figure 3.11: Measurements of $\mathrm{d}E/\mathrm{d}x$ in the DCH versus the track momentum. The curves show the Bethe-Bloch predictions obtained from control samples of particles with different masses.

identification, in particular pion-kaon separation for particles with momentum $> 0.7\,\mathrm{GeV}/c$ where $\mathrm{d}E/\mathrm{d}x$ information does not provide good separation.

- The shower shape and amount of energy deposited in the EMC helps identify electrons, muons and hadrons.
- The IFR uses transverse and longitudinal interaction patterns in the segmented steel to distinguish between muons and hadrons.

Electrons

Electrons are identified using a likelihood based selector [36] that combines information from the DCH, DIRC, and EMC. The main discriminating variable used in the selector is the ratio of energy deposited in the EMC to track momentum (E/p). This quantity should be close to unity for electrons since they deposit all their energy in the calorimeter. Other criteria considered are: $\mathrm{d}E/\mathrm{d}x$ information from the DCH, the angle θ_C and number N_C of Cherenkov photons from the DIRC, the lateral moment of the EMC cluster (defined in section 5.1.2), the number of crystals belonging to the cluster, and the azimuthal distance $\Delta\phi$ between the cluster centroid and the impact point of the track on the EMC.

The likelihood based selection results in an electron identification efficiency exceeding 90%, and a misidentification probability of order 0.05% for pions and 0.2% for kaons.

Muons

Since muons are minimum ionising particles that penetrate deep into the detector, their identification is based mainly on information collected by the IFR. The muon selection criteria are described below.

- The energy deposit in the EMC must be consistent with a minimum ionising particle, $50\ \mathrm{MeV} < E < 400\ \mathrm{MeV}$.
- The track must leave a signal in at least two IFR layers, $N_L \geq 2$.
- The number of interaction lengths λ traversed from the IP to the last RPC layer with an associated IFR cluster is required to satisfy $\lambda \geq 2.2$.
- The difference $\Delta\lambda$ between the number of traversed interaction lengths measured, and the same quantity predicted for a muon with the same angle and momentum, must satisfy $\Delta\lambda < 1.0$ for tracks with momentum $p_{lab} > 1.2\ \mathrm{GeV}/c$, and $\Delta\lambda < (|p_{lab}| - 0.5)/0.7$ for tracks with $0.5 < p_{lab} < 1.2\,\mathrm{GeV}/c$.
- The average number of RPC strips hit per layer must be less than 8. In addition, the standard deviation of the distribution of RPC strips hit per layer is required to be less than 4.
- The IFR deposits are combined to form a track and are fitted to a third degree polynomial, with the requirement $\chi^2/DOF < 3$.
- The IFR cluster centroids are compared to the position of a DCH track extrapolated to the IFR, and an agreement of $\chi^2/DOF < 5$ is required.
- The *continuity* of an IFR cluster is defined as $T_C = \frac{N_L}{L-F+1}$, where N_L is the total number of layers hit, and F and L are the first and last layers hit respectively. $T_C > 0.3$ is required for muon tracks in the forward end cap ($0.3 < \theta_{\mathrm{lab}} < 1.0\,\mathrm{rad}$), to remove beam background.

The muon identification efficiency is approximately 70% for muons with momentum exceeding 1.5 GeV/c, but drops to 50% for momenta below 0.9 GeV/c. The misidentification probability is of the order 3% for pions and 1% for kaons.

Kaons

A likelihood based selector [37] which combines information from the SVT, DCH and the DIRC is used to identify kaons. Probability density functions are calculated for each subdetector, and their product is taken to form the kaon likelihood. A kaon-pion separation of at least 2σ is achieved for particles with momenta up to $0.6\,\mathrm{GeV}/c$ in the SVT and $0.7\,\mathrm{GeV}/c$ in the DCH. For particles with higher momenta, the Cherenkov angle and number of Cherenkov photons measured from the DIRC are the main source of information for kaon identification. The kaon-pion separation achieved with the DIRC information ranges from 8σ for momenta of $2\,\mathrm{GeV}/c$ to 4σ at $4\,\mathrm{GeV}/c$.

Pions

Each track that is not identified as an electron, muon or kaon by the methods outlined in this section is assumed to be a pion and the corresponding mass assignment is made.

3.4 Data Recorded

Improvements to the detector are typically made during major shutdown periods which occur yearly. The data taking periods between these shutdowns are known as "Runs" and the detector conditions are roughly constant throughout each run. The data samples used in this analysis were recorded between 1999 and mid-2004, and are referred to as runs 1, 2, 3 and 4. An integrated luminosity of $210.5\,\mathrm{fb}^{-1}$ of on-resonance data was taken during this period, corresponding to approximately 230 million $\Upsilon(4S) \to B\overline{B}$ events. Such a large sample was collected thanks to the increasing luminosity delivered by PEP-II over the years of data taking. A sample of this size is vital for this analysis due to the low efficiency for reconstructing B meson decays.

Chapter 4

B meson reconstruction

This analysis is based on the study of high energy photons recoiling from fully reconstructed B mesons. The algorithm used to reconstruct a B decay (called semi-exclusive reconstruction) is explained in detail in this chapter. The technique, although having a low reconstruction efficiency for selecting a B candidate ($\sim 0.3\%$), provides several advantages for studying $B \to X_s\gamma$ decays:

- As the 4-vector of the $\Upsilon(4S)$ resonance and the fully reconstructed B (B_{reco}) are measured, the 4-vector of the recoil B (B_{recoil}) can be deduced. Hence, all kinematic quantities, including the photon energy, can be defined in the B_{recoil} rest frame. Other inclusive $\mathcal{B}(B \to X_s\gamma)$ analyses (for example [5, 6, 8, 10, 11]) measure the photon energy spectrum in the overall centre-of-mass frame, where the Lorentz boost of the B meson introduces additional smearing of the distribution.

- Background events, where particles from the B_{recoil} or continuum events ($e^+e^- \to u\overline{u}$,$d\overline{d}$,$s\overline{s}$,$c\overline{c}$) are used to reconstruct a fake B_{reco} candidate, are subtracted directly from the data sample. Their contribution is estimated by performing a fit to the data. No simulated events or off-resonance data are required to model this background, removing any model dependence, or dependence on the statistically limited off-resonance sample. Furthermore, background events from lepton pair ($e^+e^- \to e^+e^-$, $\mu^+\mu^-$, $\tau^+\tau^-$) and $e^+e^- \to \gamma\gamma$ processes are suppressed by requiring that the B_{reco} candidate is fully reconstructed in a hadronic decay mode.

- The branching fraction measurement does not require an estimate of the total luminosity of the data sample or the B reconstruction efficiency, only the number of reconstructed B mesons in the original sample. This reduces the systematic uncertainty on the measurement.

- By fully reconstructing the decay of one B meson, the charge and flavour of both B mesons can be determined. This enables one to measure the $B \to X_s\gamma$ branching fraction and the direct CP asymmetry (α_{CP}) separately in charged and neutral B decays when more statistics become available.

4.1 Data and Simulated Event Samples

The data and simulated samples used in this analysis are listed in table 4.1. The number of generated events, assumed branching fraction and equivalent luminosity are provided for each sample. Also given are the yields of reconstructed B decays, obtained from the technique explained in section 4.2.4.

4.1.1 Data

A data sample with an integrated luminosity of 210.5 fb^{-1} collected between 1999 and 2004 is used for this analysis. This data set corresponds to approximately 230 million $B\overline{B}$ pairs. Such a large data set is vital for this analysis due to the small efficiency for reconstructing hadronic B decays with the semi-exclusive method.

An off-resonance data sample of 9.6 fb^{-1} collected between 1999 and 2002 is used to verify the background subtraction method. This sample is produced from e^+e^- collisons with a centre-of-mass energy 40 MeV below the $\Upsilon(4S)$ resonance, where the production of B mesons is kinematically suppressed.

4.1.2 Simulation

A Monte-Carlo simulation technique was used to produce simulated events required for studying particle behaviour in the detector. The process begins with event generation, which uses EvtGen [38] for the generation of B decays to exclusive final states, and JetSet [39] for continuum events and inclusive B decay simulation. For these events to be

Sample	Number of Events ($\times 10^3$)	Number of B_{reco} Events	Cross Section or $\mathcal{B}$	Lumi (fb^{-1})
Data				
On-Resonance Data	-	625000 ± 1600	-	210.5
Off-Resonance Data	-	-	-	9.6
Background				
$e^+e^- \to u\overline{u}$,$d\overline{d}$,$s\overline{s}$	440000	-	2.09 nb	210.5
$e^+e^- \to c\overline{c}$	273700	-	1.30 nb	210.5
$e^+e^- \to \Upsilon(4S) \to B^0\overline{B}^0$	460600	1140000 ± 1630	0.547 nb	842.0
$e^+e^- \to \Upsilon(4S) \to B^+B^-$	472400	1820000 ± 2170	0.547 nb	863.6
Generic Signal				
$B^0 \to K^{*0}(892)\gamma$	436	450 ± 29	4.01×10^{-5}	9938.6
$B^{\pm} \to K^{*\pm}(892)\gamma$	458	777 ± 39	4.03×10^{-5}	10388.3
$B^0 \to X_s^0\gamma$ (KN480) with:				
full m_{X_s} range	305	-	3.52×10^{-4}	792.0
m_{X_s} 1.0-1.2 GeV	236	-	3.52×10^{-4}	612.8
m_{X_s} 1.2-1.4 GeV	246	-	3.52×10^{-4}	638.8
m_{X_s} 1.4-1.6 GeV	234	-	3.52×10^{-4}	607.7
m_{X_s} 1.6-1.8 GeV	236	-	3.52×10^{-4}	612.8
m_{X_s} 1.8-2.0 GeV	226	-	3.52×10^{-4}	586.9
m_{X_s} 2.0-2.2 GeV	220	-	3.52×10^{-4}	571.3
m_{X_s} 2.2-2.4 GeV	200	-	3.52×10^{-4}	519.4
m_{X_s} 2.4-2.6 GeV	218	-	3.52×10^{-4}	566.1
m_{X_s} 2.6-2.8 GeV	228	-	3.52×10^{-4}	592.1
m_{X_s} 2.8-3.0 GeV	226	-	3.52×10^{-4}	586.9
$B^0 \to X_s^0\gamma$ weighted total	305	404 ± 13	3.52×10^{-4}	792.0
$B^{\pm} \to X_s^{\pm}\gamma$ (KN480) with:				
full m_{X_s} range	282	-	3.52×10^{-4}	732.3
m_{X_s} 1.0-1.2 GeV	204	-	3.52×10^{-4}	529.7
m_{X_s} 1.2-1.4 GeV	204	-	3.52×10^{-4}	529.7
m_{X_s} 1.4-1.6 GeV	204	-	3.52×10^{-4}	529.7
m_{X_s} 1.6-1.8 GeV	204	-	3.52×10^{-4}	529.7
m_{X_s} 1.8-2.0 GeV	204	-	3.52×10^{-4}	529.7
m_{X_s} 2.0-2.2 GeV	204	-	3.52×10^{-4}	529.7
m_{X_s} 2.2-2.4 GeV	223	-	3.52×10^{-4}	579.1
m_{X_s} 2.4-2.6 GeV	262	-	3.52×10^{-4}	680.4
m_{X_s} 2.6-2.8 GeV	267	-	3.52×10^{-4}	693.3
m_{X_s} 2.8-3.0 GeV	260	-	3.52×10^{-4}	675.2
$B^{\pm} \to X_s^{\pm}\gamma$ weighted total	282	509 ± 16	3.52×10^{-4}	732.3
Cocktail Signal				
$B \to K^*\gamma$	214	13200 ± 151	4.02×10^{-5}	4866.0
$B \to X_s\gamma$ (KN465)	398	35600 ± 258	3.52×10^{-4}	1033.5
$B \to X_s\gamma$ (KN480)	406	35500 ± 255	3.52×10^{-4}	1054.3
$B \to X_s\gamma$ (KN495)	418	34300 ± 252	3.52×10^{-4}	1085.5

Table 4.1: Data and simulated samples used in this analysis. The number of generated events, number of B_{reco} events (see figures 4.7 - 4.8), and the luminosity of each sample are shown. The generator cross section or branching ratio is given for the simulated samples. Signal events are generated as $e^+e^- \to \Upsilon(4S) \to B\overline{B}$ with a signal decay for one B meson, and a generic or cocktail decay for the other.

Signal Sample	m_b (GeV/c^2)	μ_π^2 (GeV ^{2})
KN465	4.65	0.52
KN480	4.80	0.30
KN495	4.95	0.14

Table 4.2: The input parameters used for signal generation.

compared to real data, the response of the *BABAR* detector at each period of data taking must be simulated. The GEANT4 [40] package is used for this task. The simulated samples are produced such that they each approximately match the data sample in terms of detector and background conditions.

Signal events

The signal model used for simulation is described in section 2.4. Exclusive resonant $B \to K^*(892)\gamma$ samples, and inclusive non-resonant $B \to X_s\gamma$ samples are produced, and are combined according to the Kagan and Neubert prescription [21]. The branching fractions used for the resonant and non-resonant components are the current experimental averages [4] and are listed in table 4.1.

The Kagan-Neubert model [21] is used for simulation of the non-resonant samples. These are generated with different sets of input parameters (the b quark mass m_b, and kinetic energy μ_π^2) in order to study the effect of model dependence on the analysis efficiency. The samples are referred to as KNXXX where "XXX" is the generator value of m_b expressed in MeV/c^2 and divided by 10. Table 4.2 shows the input parameters for each sample.

KN480 is the non-resonant model used for the extraction of the branching fraction result. Simulated KN480 samples in bins of the mass of the X_s system (m_{X_s}) of width 200 MeV/c^2 are produced for use in other $\mathcal{B}(B \to X_s\gamma)$ analyses at *BABAR*. To use all the available statistics, the binned m_{X_s} samples are scaled and added to a sample of KN480 events covering the whole m_{X_s} spectrum. The scale factors are computed such that the combined sample provides the same photon energy spectrum as the KN480 model. This is illustrated in figure 4.1.

Two different types of signal samples are produced. For each type, one B meson decays according to the chosen signal model, and the other B decays either by what is

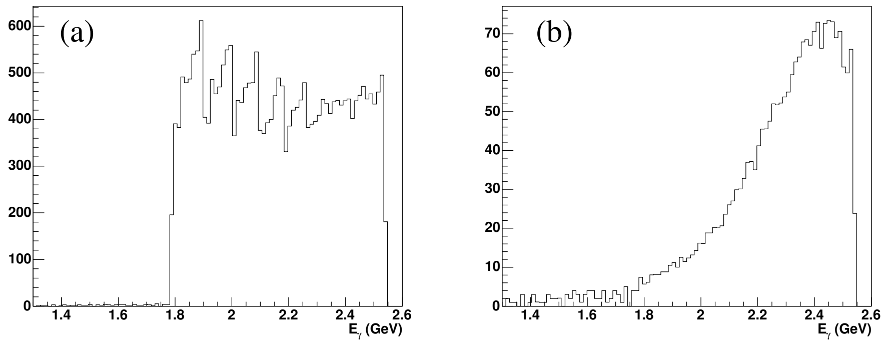

Figure 4.1: The photon energy spectrum of the combined KN480 samples (a) before and (b) after the samples are scaled.

named a *generic* decay, or a *cocktail* decay. In a generic decay the B can decay via any possible decay mode that is observed in real data. For the cocktail signal sample, the non-signal B decays only by one of a subset of the hadronic decay modes used in the semi-exclusive reconstruction. This enhances the efficiency for reconstructing a hadronic B decay in the event, resulting in a higher statistics sample. The cocktail samples are used to study the effect of model dependence on the signal selection efficiency.

$B\overline{B}$ events

Approximately 850 fb^{-1} of generic $B\overline{B}$ events are simulated, where both B mesons decay without restrictions. It is possible that either B meson may decay via the signal decay mode as these decays are included in the event generator. In this sample the resonant signal component consists of both $B \to K^*\gamma$ decays, with a branching fraction of 4.5×10^{-5} and $B \to K_2^*\gamma$ decays, with a branching fraction of 1.66×10^{-5}. The non-resonant branching fraction is set to 2.674×10^{-4} such that the total branching fraction is 3.29×10^{-4} in agreement with the Kagan-Neubert theoretical prediction [21]. When used to study the B background, $B \to K^*\gamma$, $B \to K_2^*\gamma$, and $B \to X_s\gamma$ events are removed from this sample.

Continuum events

The simulated continuum samples consist of $e^+e^- \to u\overline{u}$, $d\overline{d}$, $s\overline{s}$, $c\overline{c}$ events. Continuum and $B\overline{B}$ event samples of equal luminosity are combined to represent the data for optimization of the selection criteria (see section 5.3.1), and validation of the signal extraction method (see section 6.2). The continuum sample is also used to train a Fisher discriminant (see section 5.3.4) to reduce this type of background.

4.2 Semi-Exclusive Reconstruction

Semi-exclusive reconstruction is aimed at successfully reconstructing as many hadronic B meson decays as possible. Since the dominant B decays involve B^0 mesons decaying to charged $D^{(*)}$ mesons and $B^{\pm}$ mesons decaying into neutral $D^{0(*)}$ mesons, only these decay processes are considered.

The method involves exclusively reconstructing the $D^{(*)}$ meson candidate then adding a hadronic system $X^{\pm}$ to form a B meson candidate, where $B_{reco} \rightarrow D^{(*)}X^{\pm}$. The $X^{\pm}$ consist of combinations of π^{+}, π^{0}, K^{+} and K_{S}^{0} candidates with a total charge of ± 1.

The semi-exclusive reconstruction method is described in this section. More details on this procedure can be found in [41].

4.2.1 Meson Reconstruction

Pions and kaons are reconstructed using the methods described below. The kinematic information from these particles is used to reconstruct the $D^{(*)}$ and the hadronic system.

π^{+}, K^{+} identification

BaBar standard selection criteria (described in section 3.3.2) are used to identify electron, muon, and charged kaon tracks. Electron and muon tracks are discarded for the reconstruction of the B_{reco} . Charged tracks that pass the kaon selection are assigned the kaon mass, and those remaining are treated as charged pions.

π^{0} reconstruction

π^{0} candidates are formed from pairs of neutral clusters in the EMC with energy greater than 30 MeV and a lateral moment (defined in section 5.1.2) less than 0.8. The reconstructed π^{0} is required to have an invariant mass in the range 110 - 155 MeV/c^{2}, and an energy of at least 200 MeV.

Merged π^0 s, where the γ daughters are merged into a single EMC cluster are also identified as π^0 candidates. The identification is based on a measurement of the energy and second moment* of the cluster, as described in [42].

K_S^0 reconstruction

Only the decay $K_S^0 \rightarrow \pi^+\pi^-$ is reconstructed. The K_S^0 candidates are formed by pairing pion tracks of opposite charge, and a vertex fitting algorithm is applied to search for a vertex common to the two tracks. The K_S^0 candidate is required to have an invariant mass between 0.486 and 0.510 GeV/c^2 ($\sim 4\,\sigma$).

4.2.2 D Reconstruction

The decay modes used for reconstructing the D(*) meson candidates are listed along with their measured branching fractions in table 4.3.

D^0 reconstruction

The decay modes† $D^0 \rightarrow K^-\pi^+$, $D^0 \rightarrow K^-\pi^+\pi^0$, $D^0 \rightarrow K^-\pi^+\pi^+\pi^-$ and $D^0 \rightarrow K_S^0\pi^+\pi^-$ are used for D^0 reconstruction. The charged tracks are required to have a minimum momentum of 200 MeV/c for the $D^0 \rightarrow K^-\pi^+$ mode, and 150 MeV/c for the remaining decay modes. The invariant mass of the D^0 must lie within $\pm 3\sigma$ of the nominal D^0 mass, where σ is determined from fitting the mass distribution of each decay mode reconstructed, and ranges from 5.0 - 8.3 MeV/c^2. The candidate must have momentum in the $\Upsilon(4S)$ frame in the range 1.3 - 2.5 GeV/c. A looser lower momentum requirement of 1.0 GeV/c is applied if the D^0 is used to reconstruct a D^{*+} or a D^{*0}. The lower momentum requirement is used to reduce combinatorics, and the upper bound is motivated by the kinematic limit of a D^0 from a $B \rightarrow D^0X$ decay, or a $B \rightarrow D^{*+}X$ decay with $D^{*+} \rightarrow D^0\pi^+$. A vertex fit to the D^0 decay products is then performed and a χ^2 probability of greater than 0.1% is required.

*The second moment of a cluster is defined $S = \sum_i E_i \triangle\alpha_i^2 / \sum_i E_i$ where the sum is over all crystals in the cluster with energy E_i and angular distance from the cluster centre $\triangle\alpha_i$.

†The charged conjugate decays are implied throughout this document.

Decay mode	$\mathcal{B}(\%)$
$D^{*+} \to D^0\pi^+;\, D^0 \to K^-\pi^+$	2.55 ± 0.06
$D^{*+} \to D^0\pi^+;\, D^0 \to K^-\pi^+\pi^+\pi^-$	5.0 ± 0.2
$D^{*+} \to D^0\pi^+;\, D^0 \to K^-\pi^+\pi^0$	8.8 ± 0.6
$D^{*+} \to D^0\pi^+;\, D^0 \to K^0_S\pi^+\pi^-$ ($K^0_S \to \pi^+\pi^-$)	1.35 ± 0.08
$D^+ \to K^-\pi^+\pi^+$	9.1 ± 0.6
$D^+ \to K^-\pi^+\pi^+\pi^0$	6.4 ± 1.1
$D^+ \to K^0_S\pi^+$ ($K^0_S \to \pi^+\pi^-$)	0.94 ± 0.06
$D^+ \to K^0_S\pi^+\pi^-\pi^+$ ($K^0_S \to \pi^+\pi^-$)	2.38 ± 0.31
$D^+ \to K^0_S\pi^+\pi^0$ ($K^0_S \to \pi^+\pi^-$)	3.5 ± 1.0
$D^{*0} \to D^0\pi^0;\, D^0 \to K^-\pi^+$	2.35 ± 0.12
$D^{*0} \to D^0\pi^0;\, D^0 \to K^-\pi^+\pi^+\pi^-$	4.6 ± 0.3
$D^{*0} \to D^0\pi^0;\, D^0 \to K^-\pi^+\pi^0$	8.1 ± 0.7
$D^{*0} \to D^0\pi^0;\, D^0 \to K^0_S\pi^+\pi^-$ ($K^0_S \to \pi^+\pi^-$)	1.2 ± 0.1
$D^{*0} \to D^0\gamma;\, D^0 \to K^-\pi^+$	1.44 ± 0.19
$D^{*0} \to D^0\gamma;\, D^0 \to K^-\pi^+\pi^+\pi^-$	2.82 ± 0.18
$D^{*0} \to D^0\gamma;\, D^0 \to K^-\pi^+\pi^0$	5.0 ± 0.4
$D^{*0} \to D^0\gamma;\, D^0 \to K^0_S\pi^+\pi^-$ ($K^0_S \to \pi^+\pi^-$)	0.7 ± 0.1
$D^0 \to K^-\pi^+$	3.80 ± 0.09
$D^0 \to K^-\pi^+\pi^+\pi^-$	7.46 ± 0.31
$D^0 \to K^-\pi^+\pi^0$	13.1 ± 0.9
$D^0 \to K^0_S\pi^+\pi^-$	2.03 ± 0.12

Table 4.3: D meson decay modes used in the analysis and their corresponding branching fractions as in [16].

D^+ reconstruction

The decay modes $D^+ \to K^-\pi^+\pi^+$, $D^+ \to K^-\pi^+\pi^+\pi^0$, $D^+ \to K^0_S\pi^+$, $D^+ \to K^0_S\pi^+\pi^0$ and $D^+ \to K^0_S\pi^+\pi^-\pi^+$ are used for D^+ reconstruction. For the $D^+ \to K^-\pi^+\pi^+$ and $D^+ \to K^-\pi^+\pi^+\pi^0$ modes, the kaon is required to have a minimum momentum of 200 MeV/c, and the pion momentum must exceed 150 MeV/c. For the remaining three modes, all the charged tracks are required to have a minimum momentum of 200 MeV/c. The invariant mass of the D^+ must lie within $\pm 3\sigma$ of the nominal D^+ mass, where σ is determined from fitting the mass distribution of each decay mode reconstructed, and ranges from 6.7 - 10.0 MeV/c^2. The D^+ candidate must have a momentum in the $\Upsilon(4S)$ frame greater than 1.0 GeV/c for the decays with up to three particles in the final state, and greater than 1.6 GeV/c for decays with four particles. Furthermore, an upper boundary of 2.5 GeV/c for the momentum of the D^+ candidate is required as this is the kinematic limit for the decay $B \to D^+X$. A vertex fit is performed to the D^+ decay products and a

χ^2 probablility greater than 0.1% is required.

D^{*0} reconstruction

To reconstruct D^{*0} mesons, D^0 candidates are combined with a photon or a π^0 with momentum less than 450 MeV/c in the $\Upsilon(4S)$ frame. The chosen π^0 must have a momentum greater than 70 MeV/c, whereas the photon is required to have an energy exceeding 100 MeV. For $D^{*0} \to D^0\pi^0$ decays, the mass difference between the D^{*0} and D^0 (Δm) is required to be within 4 MeV/c^2 of the nominal value, and for $D^{*0} \to D^0\gamma$ decays, Δm must be within the range 127 - 157 MeV/c^2.

D^{*+} reconstruction

D^{*+} candidates are formed by combining D^0 candidates with a charged pion with momentum greater than 70 MeV/c in the $\Upsilon(4S)$ frame. Only D^* candidates where $D^* \to D^0\pi^+$ are reconstructed, since events with a $D^{*+} \to D^+\pi^0$ decay enter in the $B \to D^+X$ category. A vertex fit is carried out which must converge. The selected D^* candidates are required to have a Δm within $\pm 3\sigma$ of the nominal value.

4.2.3 B Candidates

The semi-exclusive reconstruction algorithm begins with the reconstruction of a D candidate (known as the *pre-seed*), then adds a charged track to form a *seed.* As $B^0 \to D^{(*)+}X$ and $B^+ \to D^{(*)0}X$ decays are the only processes considered, the seed for a B^0 candidate consists of a charged $D^{(*)}$ and an oppositely charged track, whereas charged B seeds are composed of a charged track and a $D^{(*)0}$.

Next, neutral particles and pairs of oppositely charged tracks are added iteratively to reconstruct the B candidate. The hadronic system $X^\pm$ that is combined with the $D^{(*)}$ is formed of $n_1\pi^\pm, n_2K^\pm, n_3K^0_S$ and $n_4\pi^0$, such that $(n_1 + n_2) \leq 5$, $n_3 \leq 2$ and $n_4 \leq 2$. The limit on the composition is necessary to reduce the combinatoric background in high multiplicity decay modes.

From possible combinations of particles a total of 52 X states are considered (listed in table 4.4). These include submodes (described in section 4.2.5), where some reconstructed X systems are split into ranges of invariant mass with different signal to back-

$X^{\pm}$ composition	Number of (sub)modes
h	2
$h+\pi^0$	4
$3h$	6
$h+2\pi^0$	4
$3h+\pi^0$	7
$3h+2\pi^0$	6
$5h$	6
$5h+\pi^0$	6
$K_S^0+h(+\pi^0,+2\pi^0)$	5
$K_S^0+3h(+\pi^0)$	5
$2K_S^0+3h$	1
TOTAL	52

Table 4.4: Possible composition of $X^{\pm}$ for the (sub)modes $B \to D^{(*)}X^{\pm}$ reconstructed with the semi-exclusive method. The letter h represents a charged pion or charged kaon.

ground ratios. A summary of the pre-seeds and the number of decay (sub)modes for each B decay is given in table 4.5. The $B^0 \to D^+X$ channel has an additional decay mode to include $D^{*+} \to D^+\pi^0$ which is not reconstructed as a pre-seed.

4.2.4 Kinematic Variables ΔE and M_{ES}

Two kinematic variables, ΔE and M_{ES}, are used to identify good B candidates. The mis-reconstructed B candidates are those originating from continuum events, or where particles from both B mesons are used to reconstruct the B_{reco} .

The *energy difference* ΔE is defined as:

$$\Delta E = E_B^* - \sqrt{s}/2 \tag{4.1}$$

where E_B^* is the B meson energy in the centre of mass frame and $\sqrt{s}$ is the beam energy. ΔE is approximately zero for good B_{reco} candidates. The resolution of ΔE depends on the detector momentum resolution and particle identification, as assigning the wrong mass for a particle results in a shift in ΔE. Hence it is affected by the number of neutral pions and the charge track multiplicity of the final state. For modes with many π^0 s, the ΔE distribution is asymmetrical with a longer tail at negative ΔE. Figure 4.2 shows examples of the ΔE distribution of two different reconstructed modes in the data.

Channel	Pre-seed mode	No. of B (sub)modes	Total No. of (sub)modes
$B^- \to D^0 X$	$D^0 \to K^-\pi^+$	52	208
	$D^0 \to K^-\pi^+\pi^0$	52	
	$D^0 \to K^0_S\pi^+\pi^-$	52	
	$D^0 \to K^-\pi^+\pi^+\pi^-$	52	
$\overline{B}^0 \to D^+ X$	$D^+ \to K^-\pi^+\pi^+$	53	265
	$D^+ \to K^-\pi^+\pi^+\pi^0$	53	
	$D^+ \to K^0_S\pi^+$	53	
	$D^+ \to K^0_S\pi^+\pi^0$	53	
	$D^+ \to K^0_S\pi^+\pi^-\pi^+$	53	
$B^- \to D^{*0} X$	$D^{*0} \to D^0\pi^0$, $D^0 \to K^-\pi^+$	52	416
	$D^{*0} \to D^0\pi^0$, $D^0 \to K^-\pi^+\pi^0$	52	
	$D^{*0} \to D^0\pi^0$, $D^0 \to K^0_S\pi^+\pi^-$	52	
	$D^{*0} \to D^0\pi^0$, $D^0 \to K^-\pi^+\pi^+\pi^-$	52	
	$D^{*0} \to D^0\gamma$, $D^0 \to K^-\pi^+$	52	
	$D^{*0} \to D^0\gamma$, $D^0 \to K^-\pi^+\pi^0$	52	
	$D^{*0} \to D^0\gamma$, $D^0 \to K^0_S\pi^+\pi^-$	52	
	$D^{*0} \to D^0\gamma$, $D^0 \to K^-\pi^+\pi^+\pi^-$	52	
$\overline{B}^0 \to D^{*+} X$	$D^{*+} \to D^0\pi^+$, $D^0 \to K^-\pi^+$	52	208
	$D^{*+} \to D^0\pi^+$, $D^0 \to K^-\pi^+\pi^0$	52	
	$D^{*+} \to D^0\pi^+$, $D^0 \to K^0_S\pi^+\pi^-$	52	
	$D^{*+} \to D^0\pi^+$, $D^0 \to K^-\pi^+\pi^+\pi^-$	52	
TOTAL			1097

Table 4.5: Summary of the semi-exclusive (sub)modes reconstructed.

Once all possible reconstructed modes are identified, a requirement on ΔE is applied to each mode to select good B_{reco} candidates. The ΔE selection criteria range from $-45 < \Delta E < 30$ MeV for modes without a π^0, to $-90 < \Delta E < 60$ MeV for modes with at least one π^0 in the final state. Details of the chosen ΔE ranges can be found in [41].

The *beam energy-substituted mass* (M_{ES}) is defined as:

$$M_{ES} = \sqrt{s/4 - |\vec{p}^{\,*}_B|^2} \tag{4.2}$$

where $\vec{p}^{\,*}_B$ is the B candidate momentum in the centre of mass frame. The M_{ES} distribution is approximately Gaussian around the B rest mass for B candidates whose reconstructed final state involves charged tracks only. For final states with π^0 s, the distribution can have larger tails on the lower side as these particles may not be fully contained in the EMC.

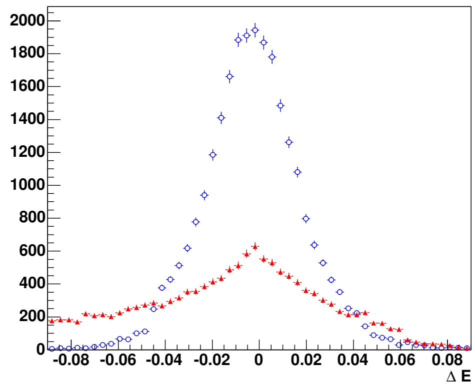

Figure 4.2: ΔE distributions of the reconstructed modes $B \to D^0\pi(D^0 \to K\pi)$ (blue circles) and $B \to D^*\pi\pi^0\pi^0(D^* \to D^0 \to K\pi\pi^0)$ (red triangles) in the data sample, requiring $M_{ES} > 5.27\,\mathrm{GeV}/c^2$.

Fitting the M_{ES} distribution

A fit to the M_{ES} distribution can be used to estimate the size of the combinatorial background, arising from mis-reconstructed B candidates. The background shape in M_{ES} can be fitted with an ARGUS [43] function:

$$g(M_{ES}; N, m_{max}, \xi) = N M_{ES}\sqrt{1-(M_{ES}/m_{max})^2}e^{-\xi(1-(M_{ES}/m_{max})^2)} \tag{4.3}$$

where the normalization N, and parameter ξ are determined from the fit. The endpoint of the ARGUS distribution, m_{max}, is fixed to 5.29 GeV/c^2 as constrained by the beam energy. The ARGUS shape describes well both continuum and $B\overline{B}$ background M_{ES} distributions as shown in figure 4.3.

The signal B component of the M_{ES} distribution is parameterised by a Crystal Ball function [44], defined as:

for $M_{ES} > m_0 - \sigma\alpha$

$$f(M_{ES}; N, m_0, \sigma, \alpha, n) = N\frac{1}{\sqrt{2\pi}\sigma}e^{-\frac{1}{2}\frac{(M_{ES}-m_0)^2}{\sigma^2}} \tag{4.4}$$

for $M_{ES} \le m_0 - \sigma\alpha$

$$f(M_{ES}; N, m_0, \sigma, \alpha, n) = N\frac{1}{\sqrt{2\pi}\sigma}\left(\frac{n}{\alpha}\right)^n e^{-\frac{\alpha^2}{2}}\frac{1}{\left(\frac{(m_0-M_{ES})}{\sigma}+\frac{n}{\alpha}-\alpha\right)^n} \tag{4.5}$$

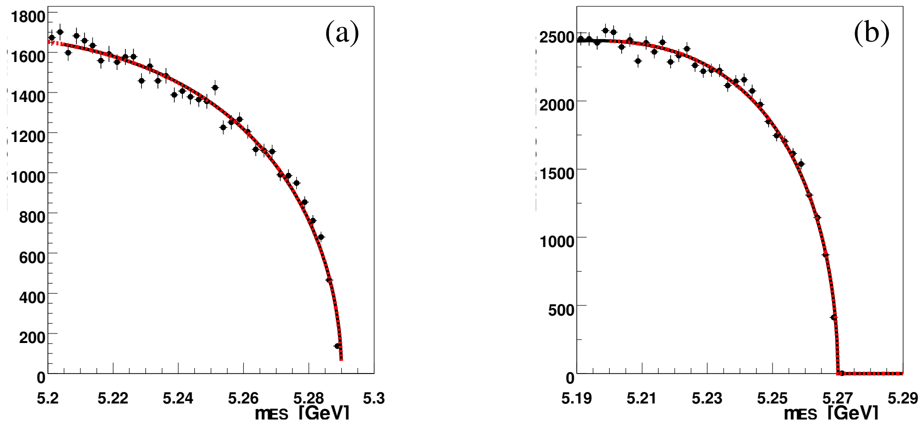

Figure 4.3: M_{ES} distribution fitted with an ARGUS function for B candidates in (a) simulated $B\overline{B}$ background (i.e. B^0 reconstructed as B^+) and (b) off-resonance data (40 MeV below the $\Upsilon(4S)$ mass). The off-resonance sample contains continuum events only.

The Crystal Ball function is a Gaussian distribution with a power law lower tail. The α parameter is the cross-over point of these two components, measured in units of width (σ) away from the peak. The parameter n is related to the length of the tail. The tail component is necessary to fit signal B candidates with neutral pions in the final state.

An example of a fit to the M_{ES} distribution is shown in figure 4.4 for modes with only one π in the X system. The region $M_{ES} < 5.27$ GeV/c^2 is known as the "sideband region" and assumed to contain only combinatorial background. The peaking region ($M_{ES} > 5.27$ GeV/c^2) contains both signal B events and combinatorial background. In this region the background yield is estimated to be the area within the ARGUS function. The remaining area beneath the Crystal Ball function is the measured signal yield.

The fit procedure involves first fitting the range $5.2 < M_{ES} < 5.265$ GeV/c^2 with an ARGUS function, to extract the error boundaries of the N and ξ parameters. The full M_{ES} range ($5.2 < M_{ES} < 5.3$ GeV/c^2) is then fitted using an ARGUS plus Crystal Ball function. The N and ξ parameters of the ARGUS are restricted to be within the error boundaries extracted from the inital ARGUS fit. In addition, the tail parameter n of the Crystal Ball is fixed to 5. All other parameters are floated. The chosen value for n is obtained from a M_{ES} fit to the signal sample with no constraints on the fit parameters. It is necessary to fix this parameter to ensure all the fits converge.

To validate the fitting method, the variation in the extracted signal yield when increasing amounts of continuum background are added to the KN480 signal sample was studied.

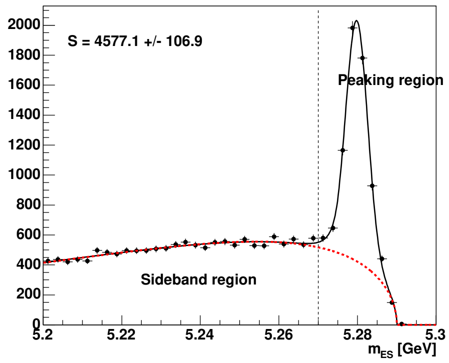

Figure 4.4: A M_{ES} distribution fitted with an ARGUS and Crystal Ball function for the reconstructed mode $B \to D^{(*)}\pi$ in the data. The vertical line separates the sideband region and peaking region. S is the measured signal yield.

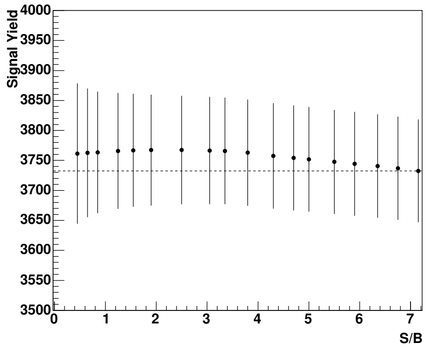

Figure 4.5: Signal yield extracted from a M_{ES} fit versus the signal to background ratio (S/B) of the fitted sample. The KN480 signal sample plus increasing amounts of simulated continuum events are used for this study. The horizontal line represents no continuum added.

Figure 4.5 shows the results of this study for the chosen fit procedure. The extracted signal yield is plotted for signal to background ratios (S/B) ranging from 0.47 (below the minimum ratio encountered in this analysis), to 7.17 (where no continuum events are added to the sample). There is no significant variation in the extracted signal yield as the continuum background is increased. Alternative fitting methods studied resulted in a variation with S/B and so were rejected.

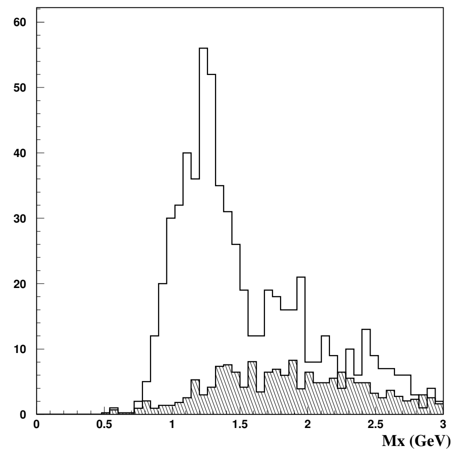

Figure 4.6: M_X distribution for $B \to D^{(*)}\pi\pi\pi$, taken from [41]. The hatched histogram shows the background, and the open histogram is the signal, evaluated from fitting the M_{ES} distribution for each M_X bin.

4.2.5 B Candidate Selection

As this process is aimed at producing a sample of reconstructed B decays that is as pure as possible, it is important to separate modes with high combinatorial background from cleaner modes. By studying the invariant mass distribution M_X of the X system and looking for resonances in the signal and background shape, high background modes can be split into low and high background submodes. For example, the mode $B \to D^{(*)}\pi\pi\pi$ is split into two submodes ($M_X < 1.5$ GeV$/c^2$ and $1.5 < M_X < 2.0$ GeV$/c^2$) without requiring that the submode has a precise resonance structure. Figure 4.6 shows the M_X distribution of signal and background for the reconstructed $B \to D^{(*)}\pi\pi\pi$ mode.

For events with more than one B_{reco} candidate the best candidate must be chosen. Two types of multiple candidates are possible:

- *Multiple candidates in the same (sub)mode.* The candidate with $|\Delta E|$ closest to zero is selected.
- *Multiple candidates in different (sub)modes.* The mode with the highest purity is selected. Purity is defined as the fraction of signal events in the region $M_{ES} > 5.27\,\mathrm{GeV}/c^2$ extracted from a fit to the M_{ES} distribution.

The (sub)modes are then ranked according to an a-priori probability given by their purity. The (sub)modes are added in order of highest purity to form the sample, and an integrated purity, I, is defined as the purity of the overall sample. In this analysis modes are added only if the integrated purity remains above 0.34. This value has been optimized for the analysis as described in section 5.3.1.

In addition to the requirement on integrated purity, 31 reconstructed B decay modes with a high combinatoric background are removed. The rejected modes have significance < 100, where significance is defined as $S^2/(S+B)$ where S is the signal yield and B is the background yield, extracted from a fit to the M_{ES} distribution. The M_{ES} distributions from data of the remaining B modes used in this analysis are shown in appendix A.

4.3 B_{reco} Event Yield

The recipe for reconstructing and selecting B candidates has been described in this chapter. To extract the yield of good B_{reco} candidates in data or simulated samples, a fit to the M_{ES} distribution is performed. The fit procedure has been discussed in section 4.2.4 and is referred to several times throughout this document. It is effective for removing the combinatorial background, and forms the first stage in the process of extracting the $B \to X_s\gamma$ signal event yield (described in section 6.1.1).

Figures 4.7 - 4.8 show fitted M_{ES} distributions of selected B candidates for the data and simulated event samples. The B_{reco} event yields are obtained from these fits, and are listed in table 4.1. More charged than neutral B decay modes are reconstructed, as the B_{reco} selection efficiency is higher for charged samples. The absolute B_{reco} selection efficiency is not required to obtain the branching fraction measurement, only the number of good B_{reco} candidates in the orginal sample. For data, the B_{reco} event yield is about 625000 events.

The next chapter describes the signal photon selection criteria, designed to suppress background from other B decays, and reduce the continuum background before the fit to M_{ES} is performed. Suppression of both background types reduces the statistical error of the branching fraction result.

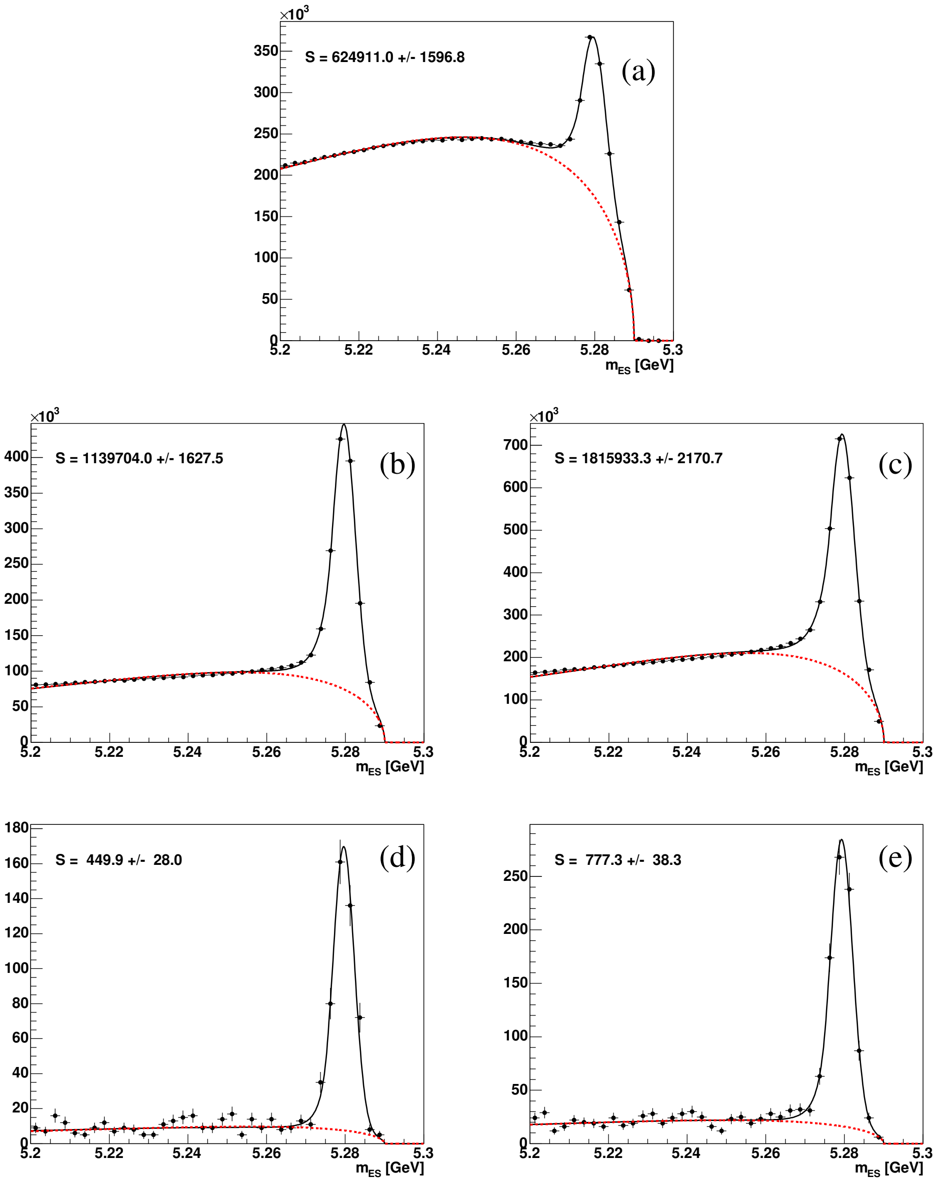

Figure 4.7: Fitted M_{ES} distributions to extract the B_{reco} event yields for the (a) data, (b) simulated generic $B^0\overline{B}^0$, (c) simulated generic B^+B^-, (d) simulated signal $B^0 \to K^{*0}(892)\gamma$ and (e) simulated signal $B^{\pm} \to K^{*\pm}(892)\gamma$ samples, with integrated purity greater than 0.34. In each case, S refers to the fitted number of signal events.

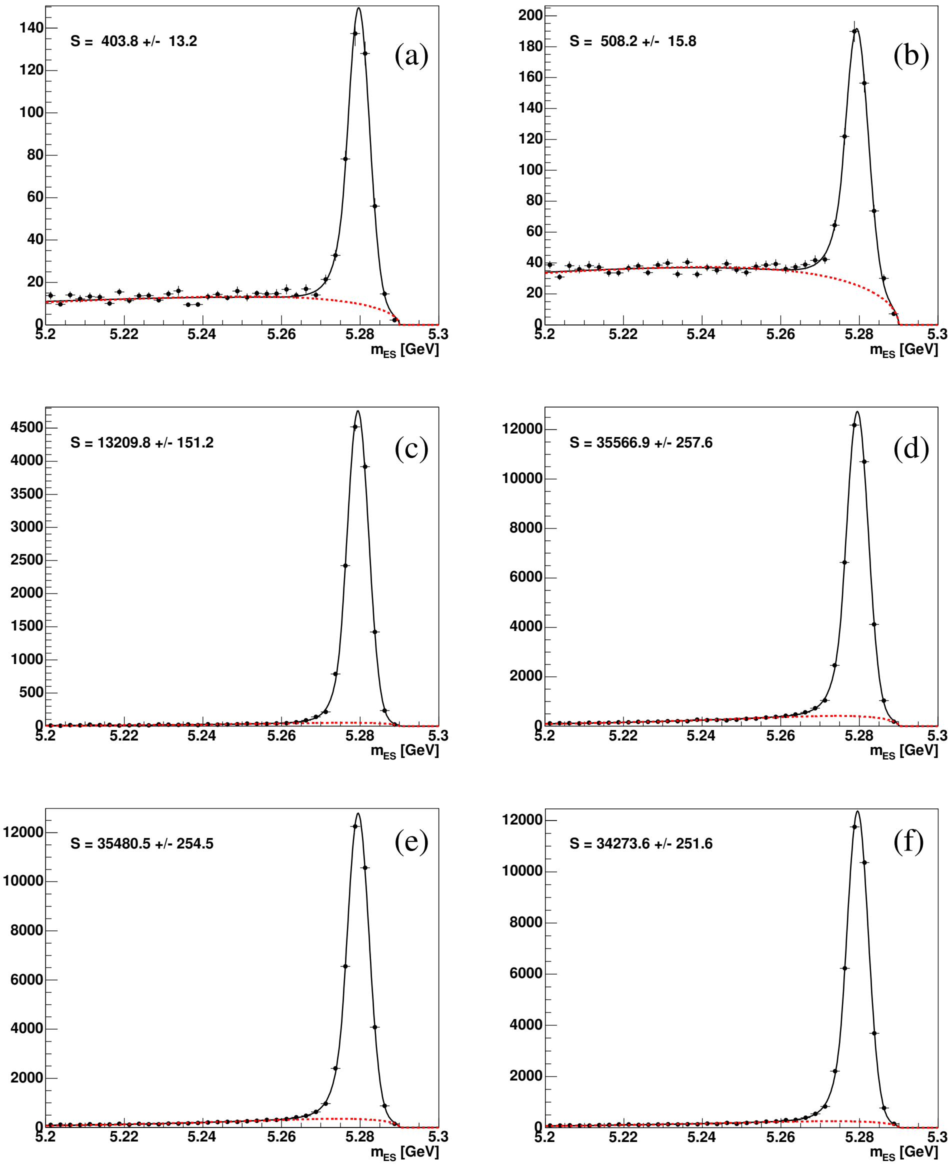

Figure 4.8: Fitted M_{ES} distributions to extract the B_{reco} event yields for the (a) $B^0 \to X_s^0\gamma$ (KN480), (b) $B^{\pm} \to X_s^{\pm}\gamma$ (KN480), (c) cocktail $B \to K^*\gamma$, (d) cocktail $B \to X_s\gamma$ (KN465), (e) cocktail $B \to X_s\gamma$ (KN480), and (f) cocktail $B \to X_s\gamma$ (KN495) simulated signal samples with integrated purity greater than 0.34. In each case, S refers to the fitted number of signal events.

Chapter 5

Selection of $B \to X_s\gamma$ candidates

A signal event is identified by the presence of a highly energetic photon in the final state of the B_{recoil} . This chapter describes the identification of charged and neutral candidates belonging to the B_{recoil} , and the criteria required to select a $B \to X_s\gamma$ event. The selection is aimed at providing the maximum rejection of background events whilst maintaining a high signal efficiency. Each of the quantities used to distinguish signal from background is described in section 5.3, and the selection optimization procedure is explained in section 5.3.1. The remaining B background composition after the selection, as estimated from simulation, is detailed at the end of the chapter.

5.1 Recoil Selection

The reconstructed charged tracks and photons of the recoil B are subjected to a set of initial criteria to ensure the quality of their reconstruction and reduce the number of fake candidates. These requirements were studied in detail for the *BABAR* $|V_{ub}|$ analysis [45] that uses the same semi-exclusive reconstruction method to identify B candidates.

5.1.1 Track Quality Selection

For tracks, the aim is to select “good” tracks stemming from an e^+e^- collision, as opposed to those from background interactions. Charged tracks used in this analysis must satisfy the requirements below. The criteria are summarized in table 5.1.

- The distance of closest approach to the beam spot must be less than 1.5 cm in the

$x - y$ plane and less than $10\,\mathrm{cm}$ along the z axis. This requirement removes tracks that do not originate from close to the interaction point.

- To remove poorly reconstructed tracks, at least one DCH hit is required for tracks with transverse momentum $p_t > 0.2\,\mathrm{GeV}/c$. This criteria is not applied to low momentum tracks since slow pions (produced for example in $D^* \to D^0\pi$ decays) would be rejected.
- The momentum of all tracks must be less than $10\,\mathrm{GeV}/c$. This requirement removes reconstructed tracks that are not compatible with the beam energies.
- Tracks are required to be within the polar angle acceptance of the detector ($0.410 < \theta_{lab} < 2.54$ rad) where the tracking efficiency is well-understood.

Description	Selection criteria
closest approach to beam spot	$\lvert d_{xy}\rvert < 1.5\,\mathrm{cm}$, $\lvert d_z\rvert < 10\,\mathrm{cm}$
minimum number of DCH hits	$N_{DCH} > 0$ if $p_t > 0.2\,\mathrm{GeV}/c$
maximum momentum	$p_{lab} < 10\,\mathrm{GeV}/c$
geometrical acceptance	$0.410 < \theta_{lab} < 2.54$ rad

Table 5.1: Summary of the track selection criteria.

5.1.2 Photon Quality Selection

Photons are identified as being local maxima of energy depositions in the EMC which are not matched to any track. For these, the aim is to eliminate those from bremsstrahlung, fakes from hadronic interactions, and unmatched clusters from charged particles.

The following criteria are applied to select "good" reconstructed photons from the B_{recoil} . The selection requirements are summarized in table 5.2. For the $B \to X_s\gamma$ candidate photon, a dedicated selection designed to separate signal from background is applied as described in section 5.3.

- To ensure the energy deposit is fully contained within the EMC, only clusters within the polar angle range $0.410 < \theta_{lab} < 2.409$ rad are considered.
- A mimimum energy requirement, $E_\gamma^{\mathrm{lab}} > 80\,\mathrm{MeV}$, is applied to remove low energy photons associated with beam related backgrounds.

- The lateral moment (LAT) of a shower is a useful variable for rejecting background from hadronic interactions in the EMC (notably from K_L's or neutrons) that fake photons. LAT is defined as:

$$LAT = \frac{\sum_{i=3}^{N} E_i r_i^2}{\sum_{i=3}^{N} E_i r_i^2 + E_1 r_0^2 + E_2 r_0^2} \tag{5.1}$$

  where N is the number of crystals within the cluster, and E_i are the crystal energies in descending order. The r_i are the distances of crystal i to the centre of the cluster, and r_0 is the average distance between two crystals (approximately 5 cm for the *BABAR* calorimeter).

  The value of LAT is defined to be in the range 0 to 1. LAT is small for electromagnetic showers where most of the shower's energy is deposited within a few crystals, and higher for hadronic showers where the energy deposit is less localised. This difference is enhanced by the two crystals with the highest energy deposits being omitted in the numerator, and by multiplying by squared distances from the shower cluster centre. LAT is required to be in the range $0.05 < LAT < 0.5$ for good photons.

- Another variable which discriminates against hadronic interactions is the ratio of the energy deposited in the 9 crystals closest to the cluster centroid, to the energy deposited in the 25 closest crystals ($S9/S25$). For electromagnetic showers $S9/S25$ is close to 1, whereas $S9/S25$ is smaller for hadronic showers as they deposit their energy in a larger number of crystals. For good photons $S9/S25$ is required to be greater than 0.9.

- Inefficiencies can occur in the track - cluster matching algorithm. If a cluster deposit is found close to a charged track but not matched to it, the deposit may be mistaken for a neutral cluster. If this occurs, the energy deposited is double counted. These clusters are removed by placing requirements on the distances in ϕ (dϕ) and θ (dθ) to all tracks without a matched cluster. The rejection criteria is summarized in table 5.2.

Description	Selection criteria
	Select clusters if:
geometrical acceptance	$0.410 < \theta_{lab} < 2.409\,\mathrm{rad}$
neutral energy	$E_\gamma > 80\,\mathrm{MeV}$
LAT	$0.05 <$LAT< 0.5
$S9/S25$	$S9/S25 > 0.9$
	Reject clusters if:
unmatched cluster	$\lvert d\theta\rvert < 30$ mrad, and
	$-30 < d\phi < 70$ mrad (to positive track)
	$-70 < d\phi < 30$ mrad (to negative track)

Table 5.2: Summary of the neutral selection criteria.

5.2 Sources of Background

As the $B \to X_s\gamma$ branching fraction [4] is so small, this analysis is carried out in the presence of large backgrounds from other processes. Fortunately the energy of photons from $B \to X_s\gamma$ decays is high enough to significantly suppress these backgrounds as no other hadronic B decays are expected to yield a direct photon in this energy range.

One of the main purposes of fully reconstructing one B is to eliminate background from continuum events ($e^+e^- \to u\overline{u}$,$d\overline{d}$,$s\overline{s}$,$c\overline{c}$). Before applying any selection criteria the continuum background component dominates (see figure 5.1). In order to minimize the statistical error of the branching fraction measurement, it is important to suppress this background as much as possible prior to fitting the M_{ES} distribution to subtract the combinatorial background.

Continuum events have a "dijet" topology in the $\Upsilon(4S)$ frame, whereas B mesons, by virtue of their low momentum, decay isotropically (as illustrated in figure 5.2). Event shape variables that exploit the difference in topology between continuum events and B decays can be used to reduce this background.

Suppressing background from non-signal B decays is more of a challenge since the global event topology is identical to that of the signal events. The B background consists of photons from asymmetric decays of inclusively produced mesons (i.e. π^0's or η's), and hadronic interactions in the EMC that fake highly energetic photons.

A small background contribution ($\sim 4\%$) from $b \to d\gamma$ decays is expected. This cannot be separated from the signal in a fully inclusive analysis. Its magnitude is estimated from theoretical predictions (as described in section 7.8) and subtracted from the final

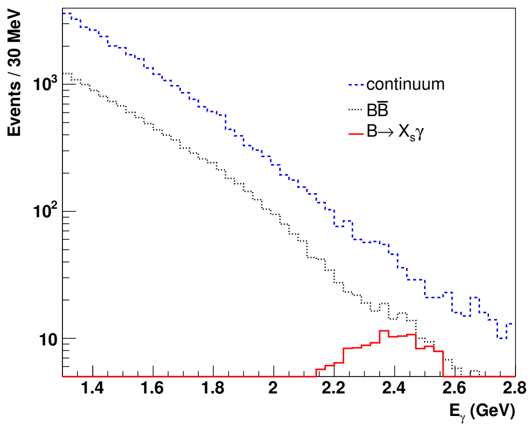

Figure 5.1: The photon energy spectrum in the B_{recoil} frame for simulated continuum, $B\overline{B}$ and signal samples, requiring an integrated purity greater than 0.34 and M_{ES} $> 5.27\,\mathrm{GeV}/c^2$. The samples are normalized to 210.5 fb^{-1}.

measurement. $B \to X_c\gamma$ is not a penguin decay process, and produces final state photons with substantially lower energy than in $B \to X_s\gamma$ decays, so a negligible amount of this type of background is expected.

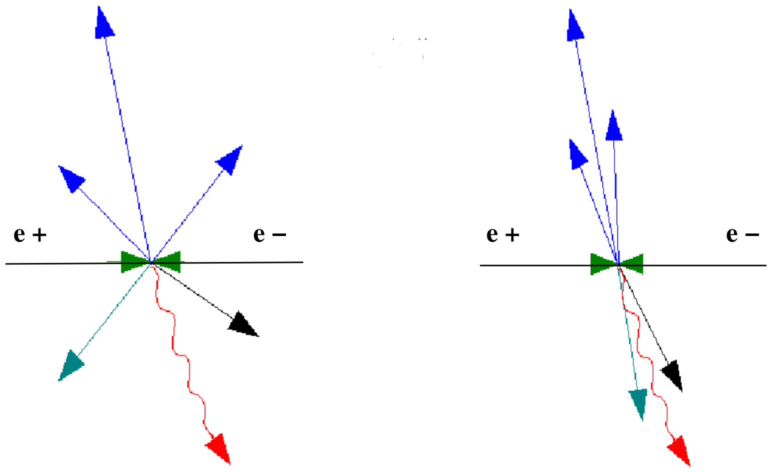

Figure 5.2: Topology of a $B\overline{B}$ event (left) and a continuum event (right) in the $\Upsilon(4S)$ rest frame. The candidate photon is also shown.

5.3 $B \to X_s\gamma$ Photon Selection

The event selection is aimed at minimizing the background from continuum and non-signal B decays whilst maintaining a high signal efficiency. To achieve this the selection requirements are optimized using the process described in section 5.3.1. Ideally, the selection must avoid introducing dependence on the model used for the simulation of the photon energy spectrum. This means that the criteria should not limit the photon energy and the selection efficiency should be independent of photon energy. These requirements should also be true for the mass of the X_s system (m_{X_s}) which is related to the photon energy by equation 2.16. The $B \to X_s\gamma$ selection criteria used in this analysis are described in this section and are summarized in table 5.4.

5.3.1 Optimization Procedure

The main selection criteria are optimized in order to minimize the statistical error of the branching fraction measurement. The optimization procedure involves varying the cut values of the discriminating variables and maximizing the significance, $S^2/(S + B)$. In this case, S is the signal event yield for the branching fraction measurement, extracted as described in section 6.1.1. As this is a blind analysis, simulated continuum and $B\overline{B}$ background samples are combined to model the data, normalized to the same luminosity. $(S + B)$ is the integral of the fitted M_{ES} distribution in the region $M_{ES} > 5.27\ \mathrm{GeV}/c^2$ for the simulated data sample.

The optimization is performed iteratively, since optimal values of some cuts depend on others. To begin, the requirements used in a previous analysis [46] are used. At each stage of optimization, all selection criteria are applied except the particular one being studied. This requirement is relaxed, and the significance is determined as a function of the cut value. The value that gives the maximum significance is chosen for the cut, and this is fixed for the subsequent optimization of the next variable. The cycle over all variables is repeated until no further changes to the cut values are necessary. Three iterations were sufficient to obtain stable cut values.

The optimization procedure is applied to the following variables: LAT, bump separation, E_{γ_2}, M_{π^0}, M_η and M_ρ. Each variable is described in section 5.3.2 where details of the chosen cut values are given. The integrated purity (defined in section 4.2.5) is also

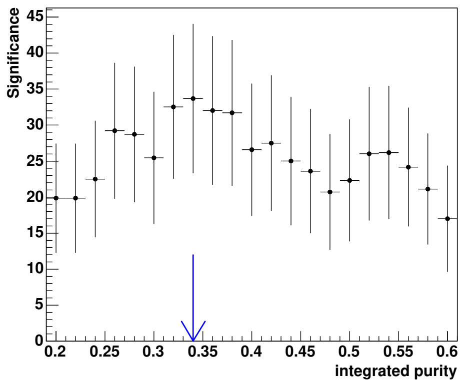

Figure 5.3: An optimization plot showing how significance $S^2/(S+B)$ varies with the minimum integrated purity requirement. The arrow indicates the chosen cut value.

optimized with these variables. Figure 5.3 shows how significance varies with cut value for the integrated purity in the final round of optimization. For samples used in this analysis, an integrated purity greater than 0.34 is required as this value yields the maximum significance.

5.3.2 Selection Criteria

The following describes the selection of the high energy photon from the $B \to X_s\gamma$ decay, and hence is applied to photons from the B_{recoil} .

Photon Energy

Due to rising background at the lower end of the photon spectrum (as seen in figure 5.1), the measured signal yield used to calculate the branching fraction is obtained from photons with energy $E_\gamma > 1.9\,\mathrm{GeV}$ in the B_{recoil} rest frame. This cut-off is chosen to avoid large systematic uncertainties from using simulation to estimate the B background. In the future, with more statistics available and improved techniques to reduce the background, it is anticipated that one will be able to measure the photon spectrum to lower energies.

The region $1.3 < E_\gamma < 1.9\,\mathrm{GeV}$ is used to obtain the background normalization coefficient for the calculation of the branching fraction (see section 6.1.1). If there is more than one photon candidate from the B_{recoil} with energy exceeding $1.3\,\mathrm{GeV}$, the most energetic is selected. Multiple candidates occur in $\sim 1.5\%$ of events with $E_\gamma > 1.3\,\mathrm{GeV}$

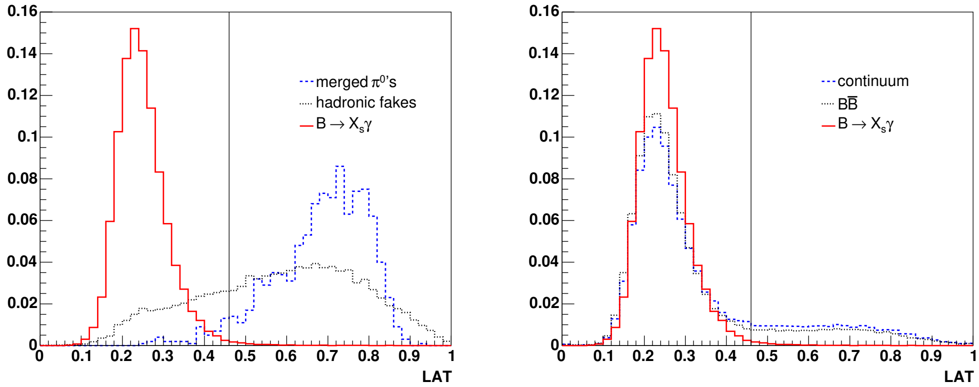

Figure 5.4: Distributions of LAT scaled to unit area for simulated signal and background samples. The vertical line shows the maximum accepted value of LAT.

and only $\sim 0.2\%$ of events with $E_\gamma > 1.9\,\mathrm{GeV}$.

Cluster Criteria

The EMC cluster of which the photon is composed must be of good quality (i.e. it must not contain any dead or noisy crystals), and consist of at least 4 crystals to ensure that the photon is well reconstructed. The cluster must be fully contained within the EMC ($0.410 < \theta_{lab} < 2.409$ rad).

Unmatched Clusters

Cluster deposits found close to a track but not matched to it are removed. The criteria to reject unmatched clusters are detailed in table 5.4. These requirements are the same as those applied to non-signal photons from the B_{recoil} as described in section 5.1.2.

Lateral Moment (LAT)

The variable LAT is defined in section 5.1.2. To reduce background from hadronic interactions in the EMC that fake a photon signature, LAT is required to be less than 0.46 for signal photon candidates. This requirement also helps to suppress background from merged π^0 s, where the energy deposits from the photon decay products are so close that they are indistinguishable as separate clusters. Figure 5.4 shows the LAT distribution for signal photons, hadronic fakes and merged π^0 s, and also for simulated signal and

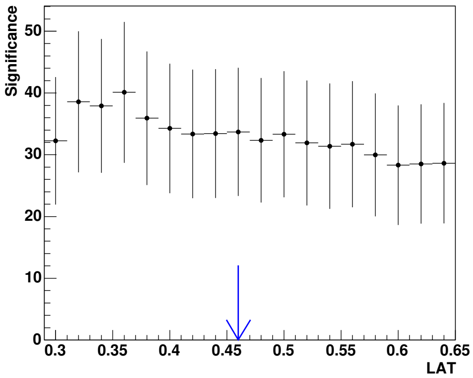

Figure 5.5: An optimization plot showing how significance $S^2/(S+B)$ varies with the cut value of the LAT requirement. The arrow indicates the chosen cut value.

background event samples.

The LAT optimization plot is shown in figure 5.5. Instead of the cut value that provides the maximum significance, the requirement LAT< 0.46 is chosen to avoid cutting in the region where the agreement between data and simulation is poor (see section 7.6).

Photon Isolation

Signal events have a lower multiplicity than continuum and B background events, so requiring that the selected photon is isolated from other energy deposits in the EMC helps discriminate against background. Figure 5.6a shows the distance from the photon to its nearest bump (defined in section 3.3.1) in the EMC for signal, continuum and B background events. The bump separation requirement is optimized as described in section 5.3.1. Instead of the cut value that yields the highest significance, the cut is relaxed to a minimum bump distance $> 50\,\mathrm{cm}$. This is to reduce the dependence on the model used to simulate signal events, as this variable is dependent on the multiplicity of the X_s system which is related to the photon energy.

π^0 and η vetos

The principal source of background comes from the decays $\pi^0 \to \gamma\gamma$ and $\eta \to \gamma\gamma$. This background can be suppressed by eliminating photon candidates that are part of a photon pair with an invariant mass close to the π^0 or η mass.

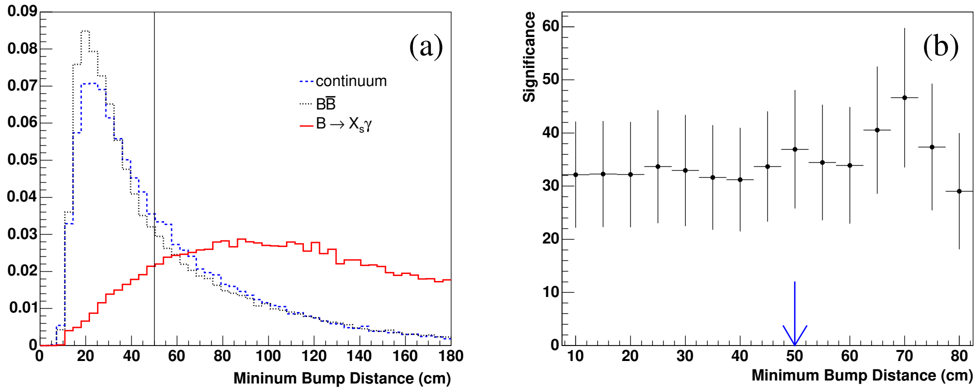

Figure 5.6: (a) Distribution of the distance (in cm) at the EMC between the high energy photon candidate and the nearest other bump, for simulated signal and background samples. Each distribution is scaled to unit area. The vertical line shows the minimum accepted bump separation distance. (b) An optimization plot showing how significance $S^2/(S+B)$ varies with the minimum bump distance requirement. The arrow indicates the chosen cut value.

To identify π^0 decays, photon candidates are paired with any other photon in the event and the pair with an invariant mass closest to the π^0 mass is selected as the π^0 candidate. A minimum energy requirement of the second photon is necessary to exclude reconstructed π^0 s where one daughter photon may be poorly reconstructed or associated with beam related background. As the first photon is highly-energetic, the second is restricted by kinematics to have low energy. The minimum cluster energy requirement of 80 MeV for "good" reconstructed photons is too high in this case. Instead, the energy of the second photon (E_{γ_2}) must exceed 35 MeV. If a reconstructed π^0 satisfies this requirement and has an invariant mass in the range $110 < M_{\pi^0} < 160\,\mathrm{MeV}/c^2$ the photon candidate is assumed to come from a π^0 decay and is rejected. The chosen values for the minimum photon energy and M_{π^0} window are optimized as described in section 5.3.1. These cut values give the highest significance, as shown in the optimization plots in figure 5.7.

The same procedure for reconstructing π^0 candidates can be applied to reconstructing η s. Figure 5.8 shows the invariant mass distribution of η candidates with a minimum photon energy requirement of $315\,\mathrm{MeV}$. Unfortunately, after applying all other signal selection criteria, the optimization procedure showed no gain from including η veto requirements. A range of minimum photon energies and invariant mass windows for η candidates were studied, and each combination gave a negligible improvement in significance.

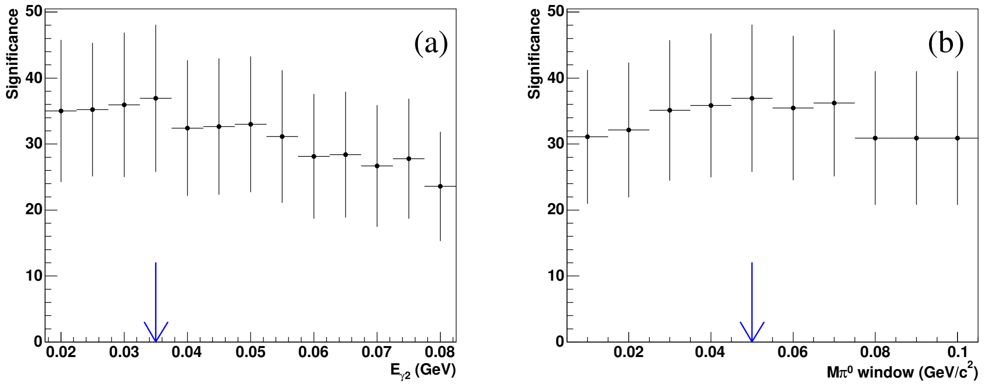

Figure 5.7: Optimization plots showing how significance $S^2/(S+B)$ varies with the cut value of (a) energy of the second π^0 photon and (b) the M_{π^0} window around the π^0 mass. The arrows indicate the chosen cut values.

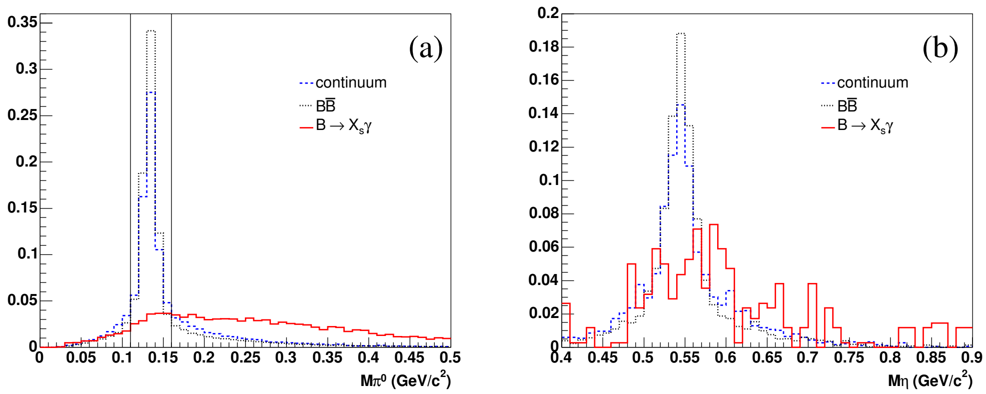

Figure 5.8: (a) The invariant mass distribution of reconstructed π^0 candidates with photon energies $> 35\,\mathrm{MeV}$. The vertical lines show the range removed by the π^0 veto requirement. (b) The invariant mass distribution of reconstructed η candidates with photon energies $> 315\,\mathrm{MeV}$. All distributions are scaled to unit area.

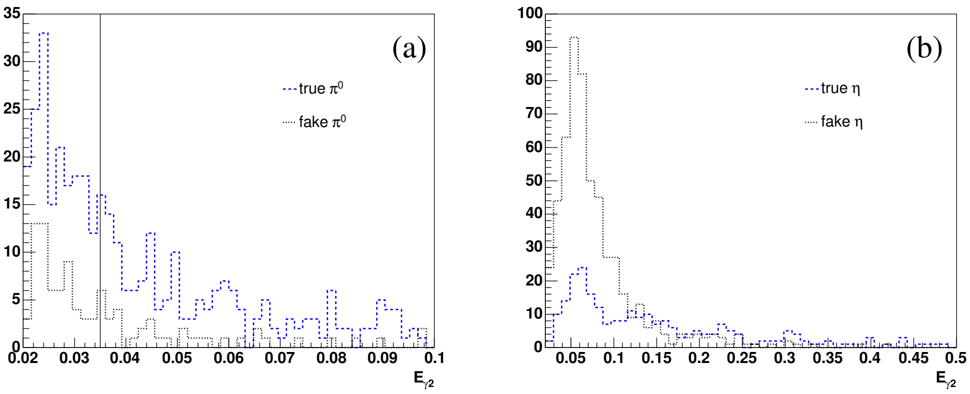

Figure 5.9: (a) Energy of the second photon for π^0 candidates with $110 < M_{\pi^0} < 160\,\mathrm{MeV}/c^2$, for real and fake π^0 s. The vertical line shows the minimum accepted photon energy for π^0 candidates. (b) Energy of the second photon for η candidates with $508 < M_\eta < 588\,\mathrm{MeV}/c^2$, for real and fake η s. All other signal selection criteria are applied.

Figure 5.9 shows the energy distribution of second photons for π^0 (η) candidates, for both real and fake π^0 s (η s) within the M_{π^0} (M_η) veto window. All other selection criteria are applied, but the continuum background subtraction is not performed. For π^0 s, the majority of candidates within the veto window are real π^0 s, whereas for η s most of the reconstructed candidates are not η particles. The η veto requirements do not help reduce background from η decays after all other selection criteria, and so are not applied in this analysis.

ρ veto

After applying the criteria described above, the B background is still dominated by photons from π^0 decays (see table 5.7). 64% of these are from π^0 s where the second photon is soft ($E_{\gamma_2} < 100$ MeV) and is not reconstructed even though it is within the calorimeter region of acceptance. Furthermore, 70% of these events are from decays in which the π^0 is generated by a ρ decay (notably, $B \to D^*\rho, \rho \to \pi^0\pi^+, \pi^0 \to \gamma_1\gamma_2$). In order to reject such events, a ρ veto is applied.

Since the lost photon is soft ($E_{\gamma_2} < 100$ MeV) the direction and energy of the π^0 can

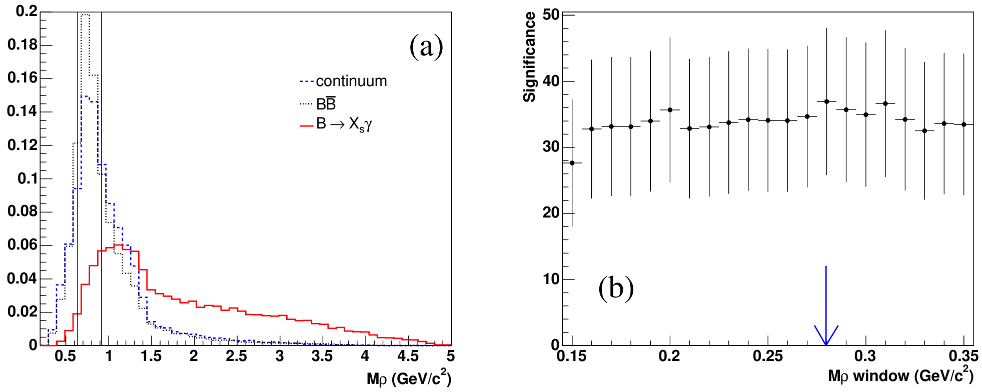

Figure 5.10: (a) The distribution of M_ρ for signal and background samples, scaled to unit area. The vertical lines show the range removed by the ρ veto requirement. (b) An optimization plot showing how significance $S^2/(S+B)$ varies with cut value of the M_ρ window around the ρ mass. The arrow shows the chosen M_ρ window for the ρ veto requirement.

be approximated by the direction and energy of the energetic photon ($E_\gamma > 1.3\,\mathrm{GeV}$):

$$(\theta, \phi, E)_{\pi^0} \sim (\theta, \phi, E)_\gamma \tag{5.2}$$

The absolute value of the π^0 three vector momentum is computed as:

$$|\vec{P_{\pi^0}}| = \sqrt{E_{\pi^0}^2 - M_{\pi^0}^2} \tag{5.3}$$

The π^0 is paired with all particles identified as charged pions belonging to the B_{recoil} . In addition, for charged B decays, charge correlation is applied since the ρ and B have the same charge in a two body decay. The pair with an invariant mass $M(\pi^0, \pi)$ closest to the ρ mass is selected as the ρ candidate. Figure 5.10 shows the invariant mass distribution of ρ candidates (M_ρ), and an optimization plot for the M_ρ veto criteria. Events are vetoed if $636 < M_\rho < 916\,\mathrm{MeV}/c^2$.

5.3.3 Event Shape Variables

There are many variables that exploit the differences in event topology to distinguish between $B \to X_s\gamma$ and background events. The event shape variables used in this analysis are described below. As the variables are correlated, instead of making separate requirements on each one it is advantageous to combine them into a single discriminant variable according to the Fisher discriminant algorithm (see section 5.3.4).

Thrust

The thrust axis of an event $\hat{T}$, is the direction which maximizes the sum of the longitudinal momenta $\mathbf{p}$ of the particles. Thrust T, is related to $\hat{T}$ by

$$T = \frac{\sum_i |\hat{T} \cdot \mathbf{p}_i|}{\sum_i |\mathbf{p}_i|}. \tag{5.4}$$

T ranges from 0.5 for an isotropic event to 1 for a highly directional event. For continuum events the decay products of the B candidate lie in one of the two back to back jets (see figure 5.2), hence the decay axis of the B candidate is approximately collinear with the thrust axis of the rest of the event. For true B decays, the decay axis of the B candidate and thrust axis of the rest of the event are uncorrelated.

The thrust variables used in this analysis are shown in figure 5.11 and consist of:

- the thrust of the event computed with all particles (T), with only neutral particles (T_{neu}) and with only the decay products of the B_{reco} candidate ($T_{B_{reco}}$). For each variable the distribution peaks closer to 1 for continuum events due to their dijet topology.

- the absolute cosine of the angle between the thrust axis of the B_{reco} and the B_{recoil} ($|cos(\theta_{TBB})|$). This distribution peaks at 1 for continuum events and should be flat for B decays as the two thrust axes are uncorrelated.

- the absolute cosine of the angle between the photon and thrust axis of the B_{recoil} ($|cos(\theta_{\gamma T_{B_{recoil}}})|$). This distribution peaks towards 1 for $B \to X_s\gamma$ events since the thrust axis is in the same direction as the photon.

Fox-Wolfram Moments

The Fox-Wolfram moments H_n, are defined [47] as:

$$H_n = \sum_{i,j} \frac{|\mathbf{p}_i|.|\mathbf{p}_j|}{E_{\text{vis}}^2} P_n(cos\theta_{ij}), \tag{5.5}$$

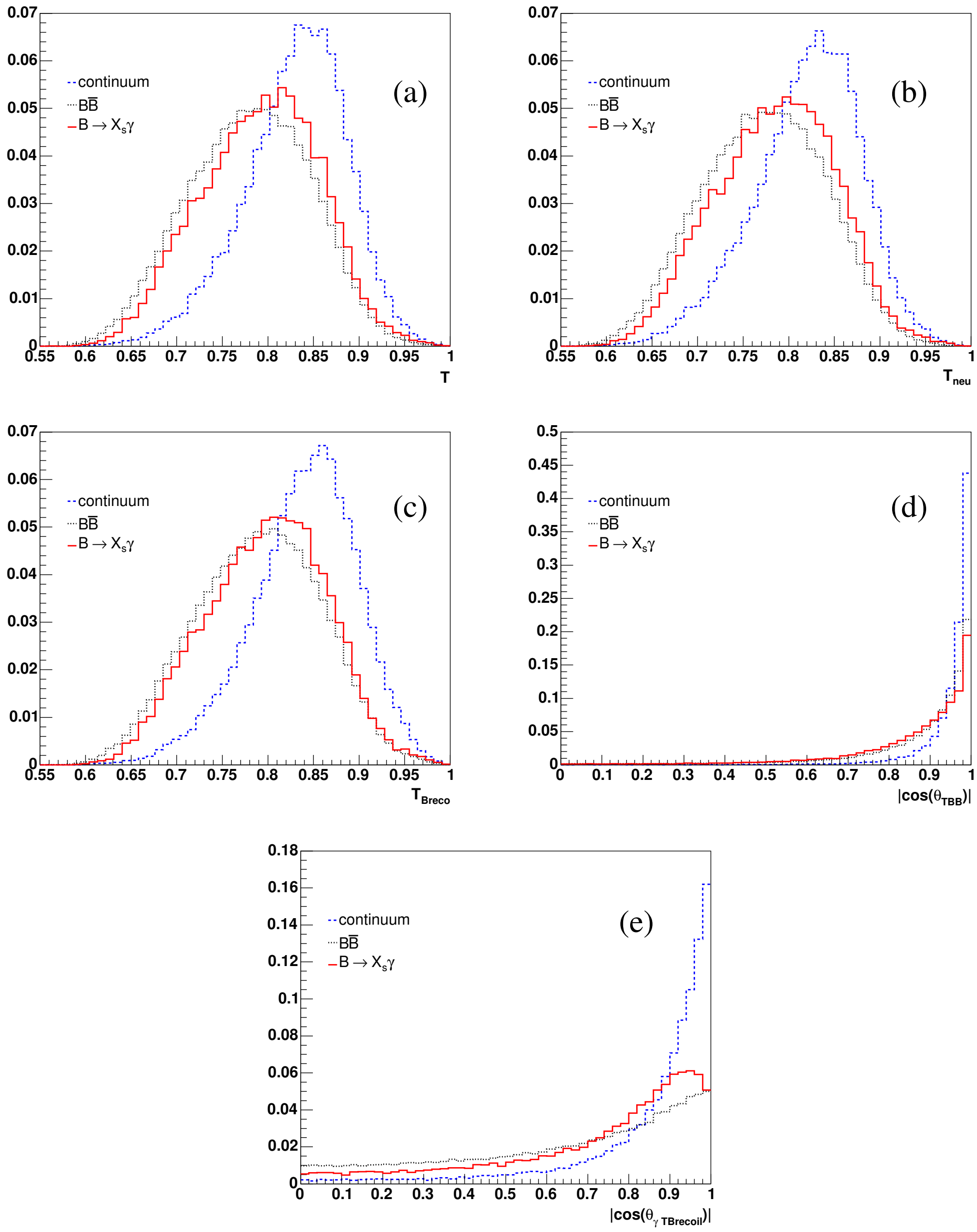

Figure 5.11: Distributions of (a) T (b) T_{neu} (c) $T_{B_{reco}}$ (d) $|cos(\theta_{TBB})|$ and (e) $|cos(\theta_{\gamma T_{B_{recoil}}})|$ for signal and background samples scaled to unit area.

where P_n are the Legendre polynomials, $\mathbf{p}_{i,j}$ are the momenta of particles i and j, θ_{ij} is the opening angle between these particles, and E_{vis} is the total visible energy of the event.

Energy and momentum conservation requires that $H_0 = 1$, neglecting particle masses. In this analysis the ratio of the second to zeroth Fox-Wolfram moment $R_2 = \frac{H_2}{H_0}$, is used as the discriminating variable. R_2 is largest for continuum events where the particle momenta are aligned along one axis. The distributions of R_2 computed with all the particles in the event, and R_2^{neu} computed with only neutral particles, are shown in figure 5.12.

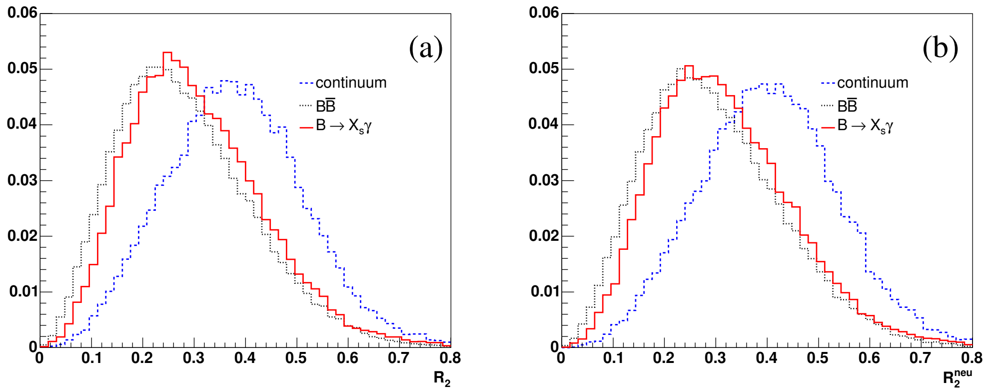

Figure 5.12: Distributions of (a) R_2 and (b) R_2^{neu} for signal and background samples. All distributions are scaled to unit area.

B_{reco} angle

The direction of a B meson from an $\Upsilon(4S)$ decay has a $\sin^2(\theta_B)$ angular distribution with respect to the beam axes in the $\Upsilon(4S)$ frame due to angular momentum conservation. The distribution of the cosine of the B_{reco} angle is shown in figure 5.13. For continuum events this distribution is flat.

Energy Flow Variables

The energy flow variables are defined as the energy sum of reconstructed particles whose momentum vectors lie within the regions: (1) $\alpha < 30°$, (2) $30° < \alpha < 140°$ and (3) $\alpha > 140°$, where α is the angle to the candidate photon. The candidate photon is excluded from the energy sum. The variables are computed with: (a) all particles in the $\Upsilon(4S)$ frame, (b) only B_{recoil} particles in the $\Upsilon(4S)$ frame, and (c) only B_{recoil} particles in the B_{recoil} rest

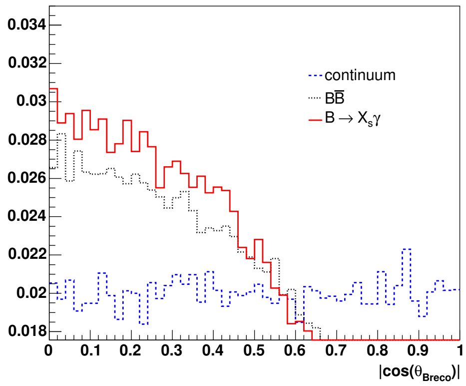

Figure 5.13: The distribution of $|\cos(\theta_{B_{reco}})|$ for signal and background samples. All distributions are scaled to unit area.

frame. The notation used to label the variables is E_{ij}, where the index i represents the α regions (1-3), and j denotes the reference frame and particles included in the energy sum (a-c), as defined above. Figure 5.14 shows the distributions of the energy flow variables for signal and background samples.

The energy flow variables are effective for discriminating against background. For continuum events, more energy is expected in the $\alpha < 30^\circ$ and $\alpha > 140^\circ$ regions when all particles are considered due to the dijet event topolgy. These jets are back to back in the $\Upsilon(4S)$ frame. In contrast, more energy is expected in the $30^\circ \leq \alpha \leq 140^\circ$ region for $B\overline{B}$ events that decay isotropically.

When including only B_{recoil} particles in the energy sum, the situation differs. For $B \to X_s\gamma$ signal events, little energy is expected to flow in the $\alpha < 30^\circ$ region, since the signal photon is excluded from the energy sum. More energy flows in the backward region $\alpha > 140^\circ$, since the photon and X_s system are omitted back to back in the B_{recoil} rest frame. In the $\Upsilon(4S)$ frame, the photon and X_s system are not directly back-to-back due to the momentum of the B_{recoil} . The variables computed in the $\Upsilon(4S)$ frame (E_{1b}, E_{2b}, E_{3b}) provide some alternative information for discriminating signal events from background to those computed in the B_{recoil} frame (E_{1c}, E_{2c}, E_{3c}), when all are combined using the Fisher discriminant algorithm.

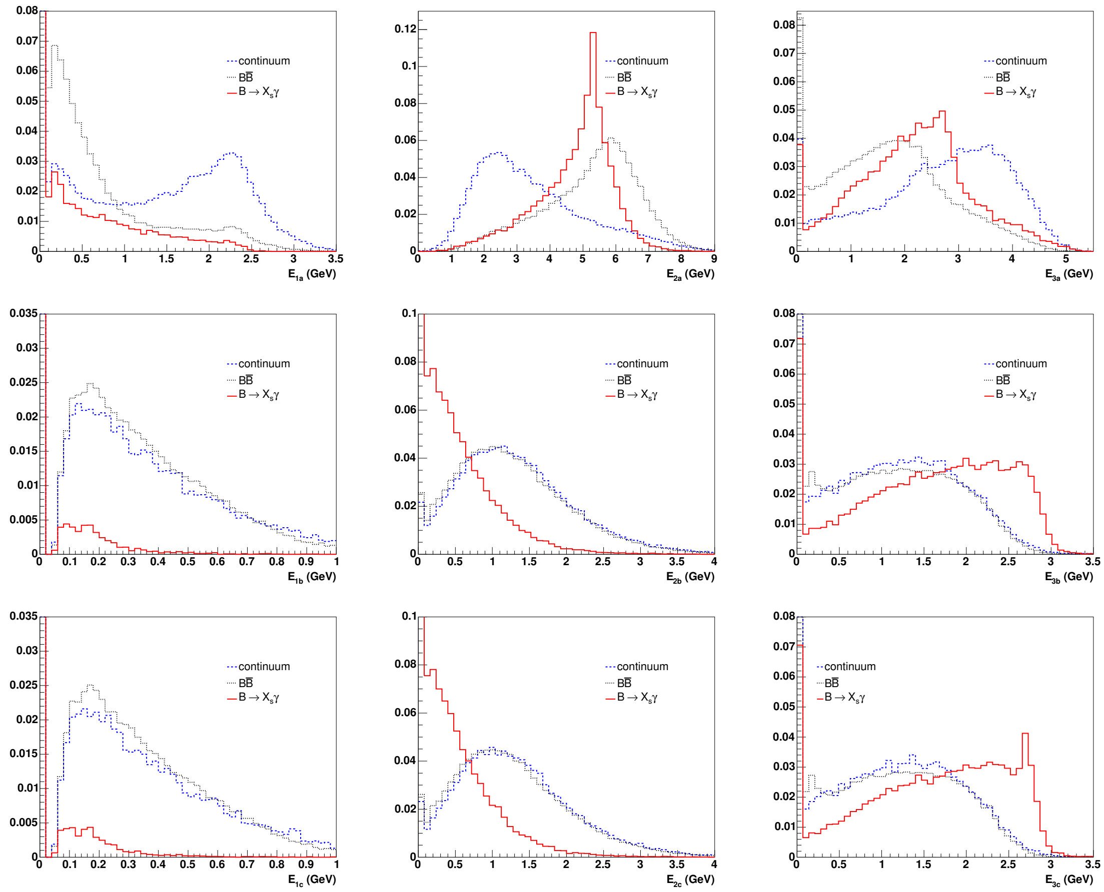

Figure 5.14: Distributions of the energy flow variables for signal and background samples. Top row: E_{1a}, E_{2a}, E_{3a} computed with all particles in the $\Upsilon(4S)$ frame. Middle row: E_{1b}, E_{2b}, E_{3b} computed with B_{recoil} particles in the $\Upsilon(4S)$ frame. Bottom row: E_{1c}, E_{2c}, E_{3c} computed with B_{recoil} particles in the B_{recoil} frame. All distributions are scaled to unit area.

5.3.4 The Fisher Discriminant

Linear discriminant techniques fully exploit the rejection power of variables that have linear correlations. Using the Fisher discriminant algorithm [48] the event shape variables described in section 5.3.3 are combined linearly. The algorithm determines the coefficients of the combination in a way that optimizes the discrimination between signal and background events.

The process can be visualized in the N-dimensonal space that the N input variables span. Each event occupies one point in the variable space. As every input variable has some discriminating power, signal and background events cluster in separate regions of the space. The Fisher discriminant algorithm determines an N-1 dimensional hyperplane that provides maximum separation between the two classes of events. Projecting the events onto this hyperplane yields a linear combination of the variables. The Fisher discriminant is given by:

$$\mathcal{F} = -O + \sum_{i=1}^{N} C_i V_i \tag{5.6}$$

where V_i are the N input variables, C_i are their coefficients and O is an offset to centre the Fisher discriminant at zero. Events that are signal-like have positive Fisher values, whereas background-like events have negative Fisher values.

The coefficients are defined as:

$$C_i = \sum_{j=1}^{N} \frac{\overline{b}_i - \overline{s}_i}{S_{ij} + B_{ij}} \tag{5.7}$$

where $\overline{s}_i$ and $\overline{b}_i$ are the mean values of the signal and background distributions for each variable and S_{ij} and B_{ij} are the covariance matrices of the variables for signal and background events.

Several combinations of discriminant variables were studied as input variables to the Fisher algorithm, in addition to those described in section 5.3.3. Energy flow cones around the photon forward and background direction were considered, along with thrust variables with alternative angle and particle combinations. To avoid introducing model dependence, variables with a strong linear correlation to the energy of the signal photon, or m_{X_s} system, were rejected. The linear coefficient of correlation, ρ, between the discriminant variable and photon energy, or multiplicity of the X_s system, is chosen to be less than 0.30

for suitable input variables. These requirements led to only the 17 variables described in section 5.3.3 being used. The correlation coefficients are shown in table 5.3 for these event shape variables.

The Fisher coefficients are computed using the *BABAR* Cornelius++ package [49], which requires equal sized signal and background event samples to train the Fisher, and independent samples for testing. Since the event shape variables mainly discriminate between signal and continuum background, only samples of these event types are employed for training. As the topology is identical for $B\overline{B}$ and signal events, including $B\overline{B}$ events in the background training sample introduces a dependence of the Fisher variable on the multiplicity of the X_s system. This dependence must be avoided, since the mass of the X_s is directly related to the photon energy by equation 2.16.

Signal and continuum samples of approximately 7500 events satisfying the signal selection criteria (excluding the π^0 and ρ vetos), are passed to the training algorithm. The π^0 and ρ veto requirements are not applied to the these samples to increase the statistics available. As the Fisher input variables are uncorrelated with the veto variables, the Fisher discriminant is still optimal after applying the veto criteria.

The coefficients of the Fisher variables are shown in table 5.3. An offset of 0.0698 is required to centre the Fisher distribution at zero. Figure 5.15 shows the distribution of the Fisher variable for signal and background samples, and the discrimination power for rejecting continuum background. A minimum value of 0.0 is required for the Fisher variable as this provides a good separation of signal and background events.

5.4 Remaining Background

A summary of the criteria for selecting $B \to X_s\gamma$ events is listed in table 5.4. Table 5.5 shows the cumulative selection efficiencies for signal and background samples. From an initial sample requiring integrated purity > 0.34, $M_{ES} > 5.27$ GeV$/c^2$, and $E_\gamma > 1.3$ GeV, 63% of signal events remain after the selection criteria, whereas the $B\overline{B}$ sample is reduced to 0.96% and the continuum sample to 0.43%. This illustrates how effective the requirements are at suppressing background.

The remaining continuum background is subtracted by performing a fit to the M_{ES} distribution of the B_{reco} . For the B background, simulation is required to estimate its

Variable	$\rho\ E_\gamma$	$\rho\ X_s$ Multiplicity	Fisher Coefficient
T	0.027	-0.063	1.4258
T_{neu}	0.036	-0.070	0.7311
$T_{B_{reco}}$	-0.028	0.085	-0.7813
$\|cos(\theta_{TBB})\|$	-0.097	0.070	-0.6579
$\|cos(\theta_{\gamma T_{B_{recoil}}})\|$	0.129	-0.059	-0.3620
R_2	0.031	-0.058	0.2711
R_2^{neu}	0.023	-0.052	-1.2205
$\cos(\theta_{B_{reco}})$	0.012	0.060	-0.3236
E_{1a}	-0.067	0.042	-0.0428
E_{2a}	-0.148	0.134	0.2164
E_{3a}	0.138	0.132	-0.0169
E_{1b}	-0.090	0.109	-0.8670
E_{2b}	-0.148	0.134	-0.8628
E_{3b}	-0.138	0.132	-0.3727
E_{1c}	-0.088	0.109	0.1907
E_{2c}	-0.286	0.263	0.1915
E_{3c}	0.212	0.141	0.4777

Table 5.3: Linear correlation coefficients with E_γ or the multiplicity of the X_s system, and the Fisher coefficients, are shown for the input variables. The correlation coefficients are computed from the simulated signal sample, and the Fisher coefficients are obtained using the *BABAR* Cornelius++ package [49]. An offset of 0.0698 is required to centre the Fisher distribution at zero.

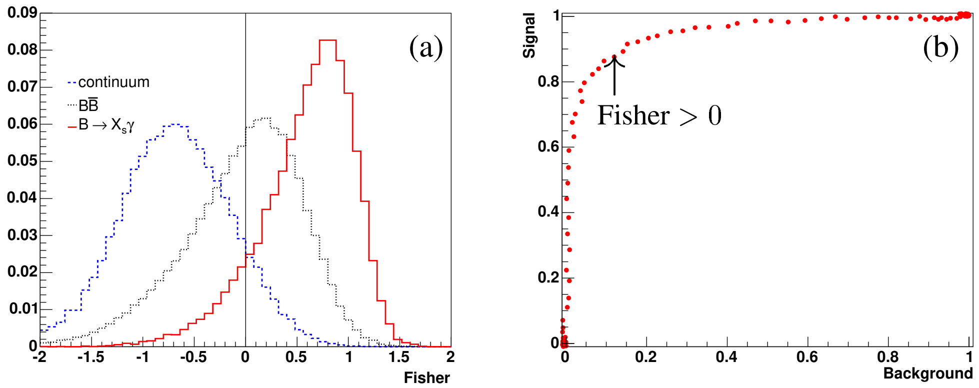

Figure 5.15: (a) The Fisher distribution for signal and background samples scaled to unit area. The vertical line shows the minimum accepted value. (b) Signal efficiency versus continuum background efficiency for various minimum Fisher requirements, computed using the Fisher training samples.

contribution. It is important to understand the composition of this background in order to reduce it as much as possible. To identify the B background types, the reconstructed candidate photons are matched to their true generated particles. Table 5.6 shows the true identity of the fake photon candidates for the B background sample after the addition of each requirement. The LAT criteria is most effective at reducing background from merged π^0 s and hadronic interactions in the EMC that fake photon candidates.

Table 5.7 shows the true origin of real candidate photons in the B background. The dominant background is from π^0 decays. The π^0 veto requirement removes mainly photons from $\pi^0 \rightarrow \gamma\gamma$ decays where both photons are reconstructed, and the ρ veto helps suppress background where only one photon is reconstructed.

The remaining B background yield after the signal selection is identified in the bottom row of tables 5.6 and 5.7. It consists mainly of photons from π^0 and η decays that are not removed by the veto requirements alone. To reduce the statistical error on the branching fraction measurement, new methods need to be studied to suppress this background. The remaining B background component in the data is estimated using a binned χ^2 fit of simulated signal and background samples to the measured photon spectrum. This procedure is explained in the next chapter.

Description	Requirement
B_{reco} Purity	integrated purity > 0.34
Photon Energy	$E_\gamma > 1.9\,\mathrm{GeV}$
Cluster Criteria	$N_{crystals} \geq 4$
	$0.410 < \theta_\gamma < 2.409\,\mathrm{rad}$
Unmatched Clusters	reject if $\lvert d\theta \rvert < 30\,\mathrm{mrad}$, and
	$-30 < d\phi < 70\,\mathrm{mrad}$ (to positive track)
	$-70 < d\phi < 30\,\mathrm{mrad}$ (to negative track)
Lateral Moment	LAT < 0.46
Photon Isolation	minimum bump distance $> 50\,\mathrm{cm}$
π^0 veto	$110 < M_{\pi^0} < 160\,\mathrm{MeV}/c^2$
	$E_{\gamma_2} > 35\,\mathrm{MeV}$
ρ veto	$636 < M_\rho < 916\,\mathrm{MeV}/c^2$
Fisher	Fisher > 0.0

Table 5.4: Summary of selection criteria for $B \to X_s\gamma$ events.

	Cumulative Efficiencies		
Requirement	$B \to X_s\gamma$ (%)	$B\overline{B}$ (%)	continuum (%)
$E_\gamma > 1.9\,\mathrm{GeV}$	91.3 ± 4.5	8.31 ± 0.10	8.62 ± 0.17
Cluster Criteria	87.5 ± 4.3	7.93 ± 0.09	8.19 ± 0.16
Unmatched Clusters	87.5 ± 4.3	7.88 ± 0.09	8.15 ± 0.16
Lateral Moment	86.9 ± 4.3	5.42 ± 0.08	5.15 ± 0.13
Photon Isolation	75.5 ± 3.9	2.54 ± 0.05	2.61 ± 0.09
π^0 veto	73.3 ± 3.8	2.17 ± 0.05	2.37 ± 0.09
ρ veto	68.6 ± 3.6	1.43 ± 0.04	1.92 ± 0.08
Fisher	63.0 ± 3.4	0.96 ± 0.03	0.43 ± 0.04

Table 5.5: Cumulative selection efficiencies for signal, $B\overline{B}$ and continuum samples requiring integrated purity > 0.34, $M_{ES} > 5.27$ GeV$/c^2$ and a reconstructed photon with $E_\gamma > 1.3$ GeV.

Requirement	Event Yields of Fake Photon Candidates e^-	μ^-	π^0	K_L^0	π^+	K^+	n	p
$E_\gamma > 1.3\,\mathrm{GeV}$	3001	35	1008	470	1402	228	12827	1124
$E_\gamma > 1.9\,\mathrm{GeV}$	221	6	242	12	85	23	2521	158
Cluster Criteria	197	5	240	12	77	22	2502	156
Unmatched Clusters	161	4	240	12	73	22	2500	151
Lateral Moment	152	4	24	6	35	16	618	78
Photon Isolation	119	1	20	3	16	16	233	24
π^0 veto	110	1	20	3	15	5	216	23
ρ veto	75	1	11	2	10	5	144	15
Fisher	34	0	7	2	2	0	76	3

Table 5.6: The B background composition of fake photon candidates obtained from $1075\,\mathrm{fb}^{-1}$ of simulated $B\overline{B}$ events requiring integrated purity > 0.34, $M_{ES} > 5.27$ GeV/c^2 and a reconstructed photon with $E_\gamma > 1.3$ GeV. The criteria in the table are applied with all preceeding requirements. Reconstructed photon candidates are matched to their true generated particle type and the yields of each type are shown.

Requirement	Event Yields of the Origin of Photon Candidates π^0 (1γ)	π^0 (2γ)	π^0 $(e^+e^-\gamma)$	η	ω	η'
$E_\gamma > 1.3\,\mathrm{GeV}$	12261	49073	327	9697	895	294
$E_\gamma > 1.9\,\mathrm{GeV}$	935	2736	17	469	23	18
Cluster Criteria	893	2651	15	453	22	18
Unmatched Clusters	893	2651	15	453	22	18
Lateral Moment	844	2609	15	450	22	18
Photon Isolation	702	656	9	376	17	17
π^0 veto	675	385	8	352	17	16
ρ veto	390	207	5	299	11	15
Fisher	316	156	4	222	11	12

Table 5.7: The origin of true photon candidates in the B background, obtained from the same sample as table 5.6. Reconstructed particles that decay to produce a true photon candidate are matched to their generated particle type and the yields of each type are shown. The π^0 category is split into π^0 s with only one photon reconstructed, both photons reconstructed and $\pi^0 \to e^+e^-\gamma$ decays.

Chapter 6

Measurement of $\mathcal{B}(B \to X_s\gamma)$

In this chapter the method for measuring the branching fraction of $B \to X_s\gamma$ decays is explained. Candidate $B \to X_s\gamma$ events are extracted from the data sample using the selection described in chapter 5. The combinatorial background is subtracted using a fit to the M_{ES} distribution of the B_{reco} candidate. The remaining background (from other B decays) is estimated using a binned χ^2 fit of signal and background simulated samples to the measured photon energy distribution. Simulated event samples are used to validate the method. The final branching fraction result is presented in this chapter.

6.1 Measurement Technique

The formula used to extract the branching fraction is:

$$\mathcal{B}(B \to X_s\gamma) + \mathcal{B}(B \to X_d\gamma) = \frac{N_{sig}^{true}}{N_B^{true}} = \frac{N_{sig}}{N_B^{meas}\epsilon} = \frac{(N^{meas} - C_b N^{bkgd})}{N_B^{meas}\epsilon} \tag{6.1}$$

where:

- N_{sig} is the signal event yield, extracted as described in section 6.1.1.
- N^{meas} is the number of B_{reco} events in data which pass the signal selection criteria (detailed in chapter 5). It comprises signal events and B background events which peak in M_{ES}.
- N^{bkgd} is the B_{reco} event yield of non-signal B decays that peak in M_{ES}. C_b is the normalization coefficient for this component determined from a binned χ^2 fit to the

measured photon energy distribution.

- N_B^{meas} is the B_{reco} event yield in data of events with an integrated purity greater than 0.34 that peak in M_{ES}.

- ϵ is the efficiency for selecting $B \to X_s\gamma$ events and is measured from the simulated signal sample.

The $B \to X_d\gamma$ component is estimated from theoretical input and subtracted from the final result. According to the Standard Model prediction the $B \to X_s\gamma$ and $B \to X_d\gamma$ branching fractions are in the ratio $|V_{td}/V_{ts}|^2$. Assuming the same efficiency for $B \to X_d\gamma$ and $B \to X_s\gamma$ decays, a correction of $(-4.0 \pm 1.6)\%$ must be applied to extract $\mathcal{B}(B \to X_s\gamma)$.

6.1.1 Extraction of the Signal Event Yield (N_{sig})

After applying the signal selection criteria (detailed in chapter 5) many background events still remain. The combinatorial background is subtracted from a fit to the M_{ES} distribution of the B_{reco} in bins of photon energy of width 0.1 GeV. Figures 6.1 - 6.3 show the M_{ES} fits for data, simulated signal and simulated non-signal $B\overline{B}$ events that satisfy the signal selection criteria, excluding the E_γ requirement. Events with $1.3 < E_\gamma < 1.9\,\mathrm{GeV}$ which pass the rest of the selection are also used in the method of signal extraction, but these do not contribute directly to the measured signal yield.

To ensure the data are well described by the simulation, the simulated components are scaled to the same ratio of charged to neutral B events as observed in the data. The samples are scaled before the fits to M_{ES} in bins of E_γ are performed. The yield of charged and neutral B decays is obtained by identifying the charge of the B_{reco} candidate from its decay products. Figure 6.4 shows the M_{ES} fits used to extract the number of charged and neutral B events in the data and simulated samples. For the simulated samples (detailed in table 4.1), a scale factor of 1.16 is required for charged signal events and 0.97 for charged B background events, so that the charged to neutral event ratio matches the data.

Background events from non-signal B decays are present in the peaking component of the M_{ES} distribution. This contribution cannot be subtracted from a fit to M_{ES}, so is estimated using a binned χ^2 fit to the photon energy spectrum. The measured E_γ

distribution N_i^{meas}, is fitted bin-by-bin to the sum of two distributions; the signal N_i^{sig} and peaking background N_i^{bkgd}:

$$\mu_i = C_s N_i^{sig} + C_b N_i^{bkgd} \tag{6.2}$$

The shapes of these distributions are determined from simulation and are shown in figures 6.1(q), 6.2(q) and 6.3(q).

The normalization factors C_s and C_b of the signal and peaking background are obtained from the binned χ^2 fit. The χ^2 function is:

$$\chi^2(C_s, C_b) = \sum_i \left(\frac{N_i^{meas} - \mu_i(C_s, C_b)}{\sqrt{\delta N_i^{meas2} + \delta N_i^{sim2}}} \right)^2 \tag{6.3}$$

where N_i^{meas} is the number of observed events, and δN_i^{meas} and δN_i^{sim} are the statistical errors from the M_{ES} fits to data and the simulated samples respectively.

The last bin of each E_γ distribution is chosen to contain events with $1.9 < E_\gamma < 2.7\,\mathrm{GeV}$. The signal yield is determined from this bin only, as:

$$N^{sig} = N_{last}^{meas} - C_b N_{last}^{bkgd}. \tag{6.4}$$

The B_{reco} event yields extracted from the binned M_{ES} fits in the range $1.9 < E_\gamma < 2.7\,\mathrm{GeV}$ (plots (g) - (n) of figures 6.1- 6.3) are not considered in the χ^2 fit in order to minimize the dependence of the branching fraction result on the shape of the simulated signal E_γ distribution. These yields are used to extract an approximate background subtracted photon energy distribution ($N_i^{meas} - C_b N_i^{bkgd}$), assuming a uniform selection efficiency in E_γ.

6.1.2 Extraction of the B_{reco} Event Yield (N_B^{meas})

The B_{reco} event yield is obtained from a fit to the M_{ES} distribution of the B_{reco} for data, requiring an integrated purity greater than 0.34 and no other selection criteria. The fit is shown in figure 6.4(g), and the measured B_{reco} event yield is is 624911 $\pm$ 1597.

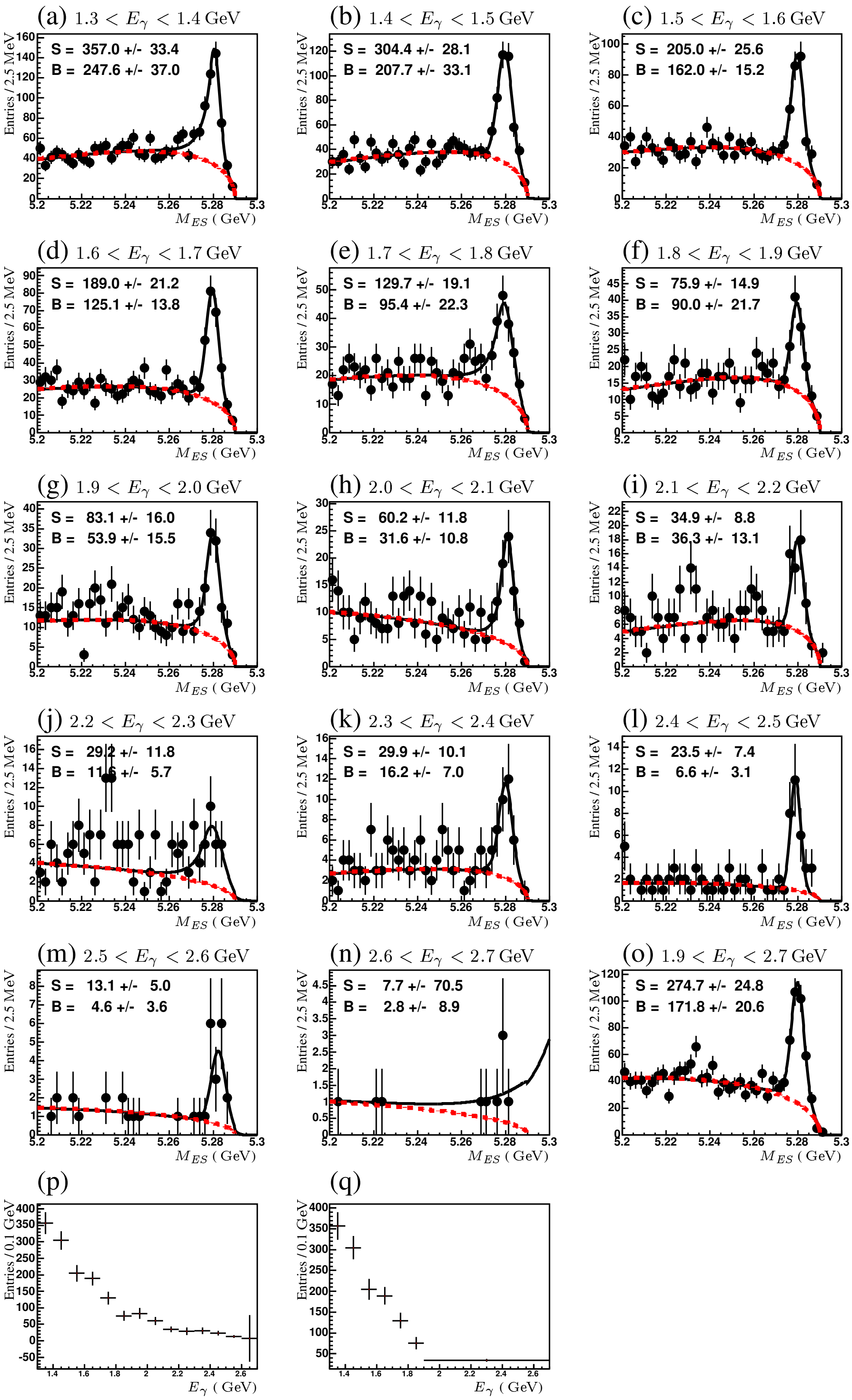

Figure 6.1: Fits to the M_{ES} distributions of the B_{reco} for data events that pass the $B \to X_s\gamma$ selection: (a) - (n) in bins of E_γ ranging from 1.3 GeV to 2.7 GeV, and (o) for events with $1.9 < E_\gamma < 2.7$ GeV. S and B represent the fitted signal and background yields respectively. (p) shows N_i^{meas} for each E_γ range fitted, and (q) shows N_i^{meas} for the ranges of E_γ considered in the χ^2 fit.

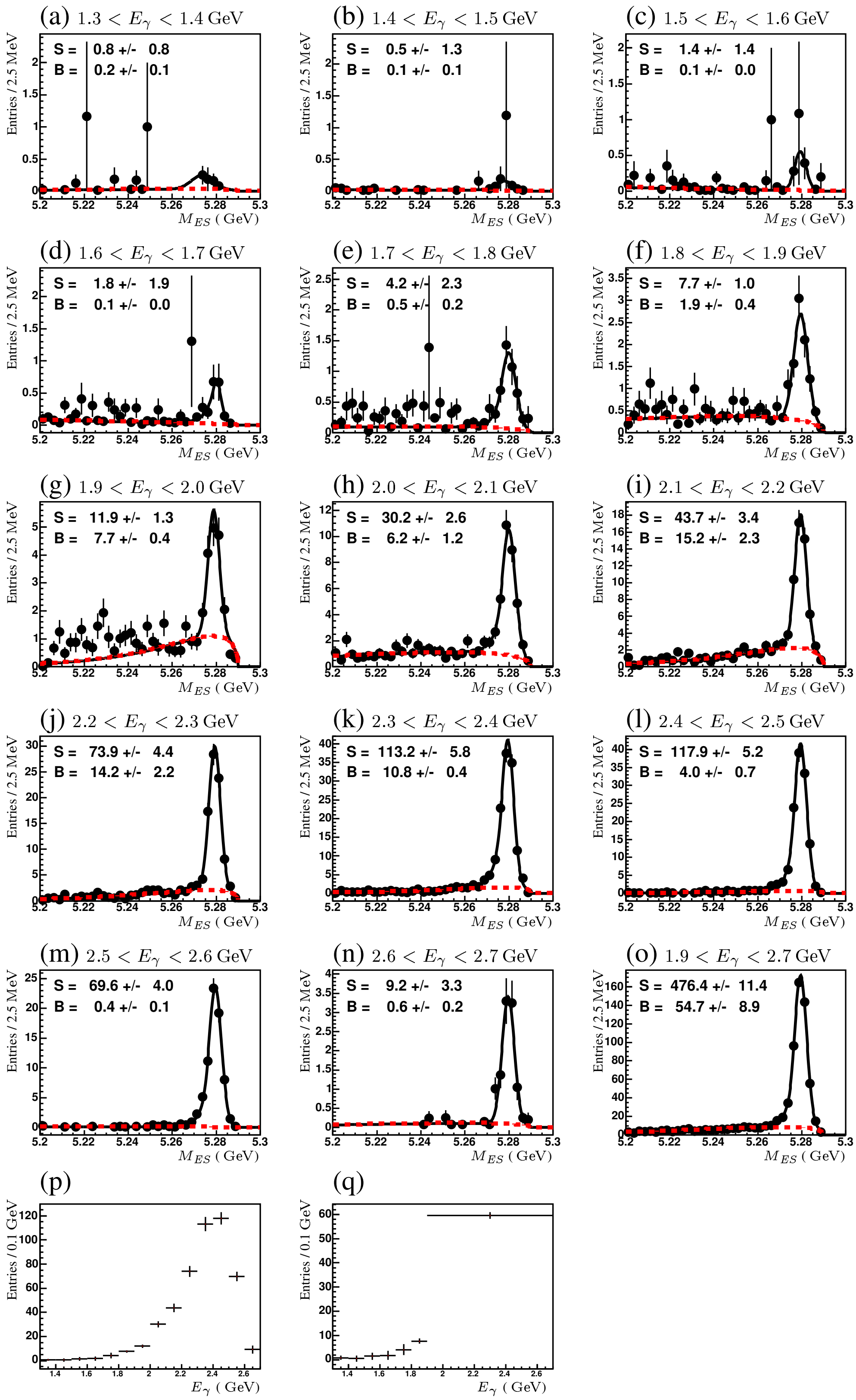

Figure 6.2: Fits to the M_{ES} distributions of the B_{reco} for $B \to X_s\gamma$ simulated events that pass the $B \to X_s\gamma$ selection: (a) - (n) in bins of E_γ ranging from 1.3 GeV to 2.7 GeV, and (o) for events with $1.9 < E_\gamma < 2.7$ GeV. S and B represent the fitted signal and background yields respectively. (p) shows N_i^{sig} for each E_γ range fitted, and (q) shows N_i^{sig} for the ranges of E_γ considered in the χ^2 fit.

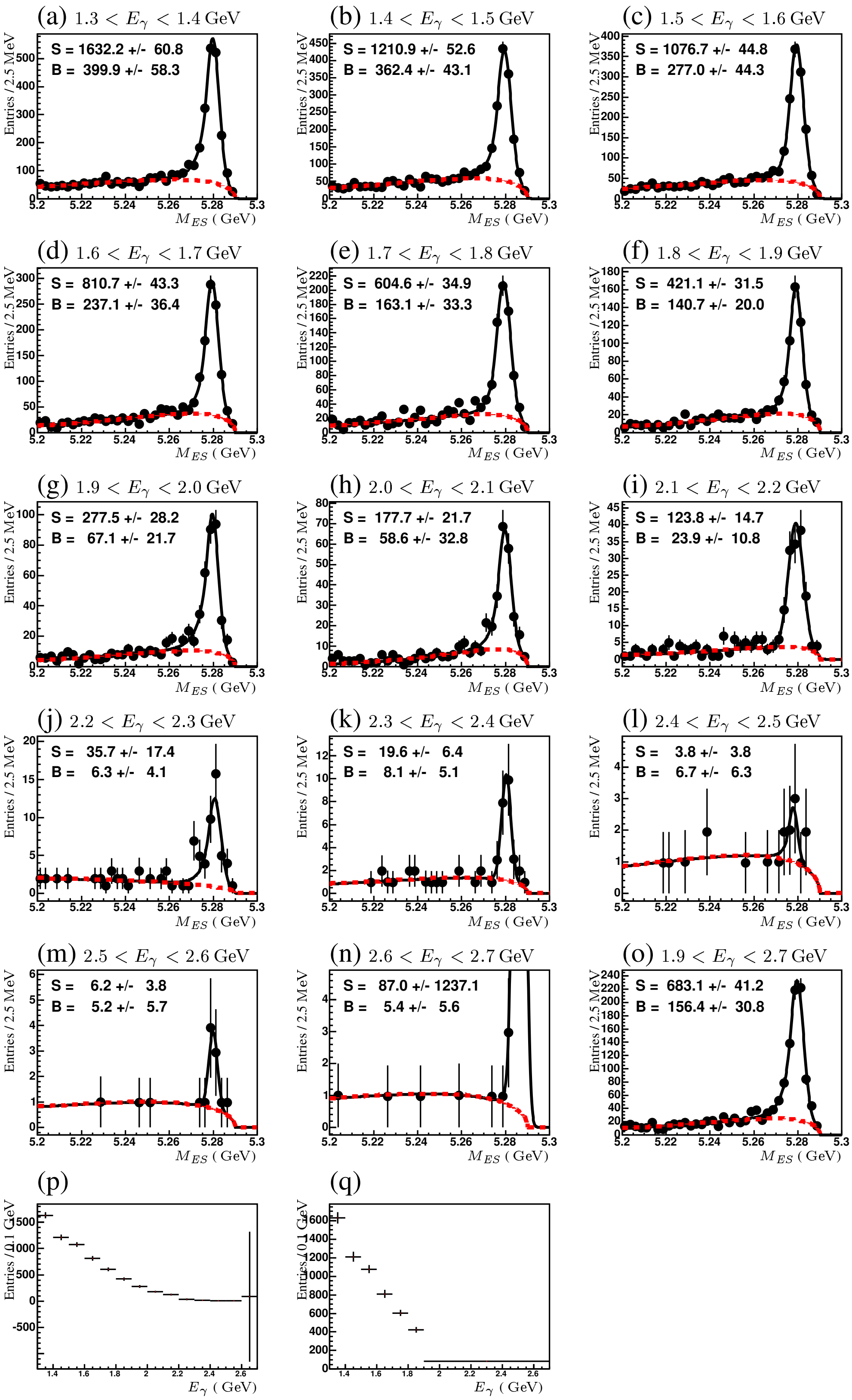

Figure 6.3: Fits to the M_{ES} distributions of the B_{reco} for non-signal $B\overline{B}$ simulated events that pass the $B \to X_s\gamma$ selection: (a) - (n) in bins of E_γ ranging from 1.3 GeV to 2.7 GeV, and (o) for events with $1.9 < E_\gamma < 2.7$ GeV. S and B represent the fitted signal and background yields respectively. (p) shows N_i^{bkgd} for each E_γ range fitted, and (q) shows N_i^{bkgd} for the ranges of E_γ considered in the χ^2 fit.

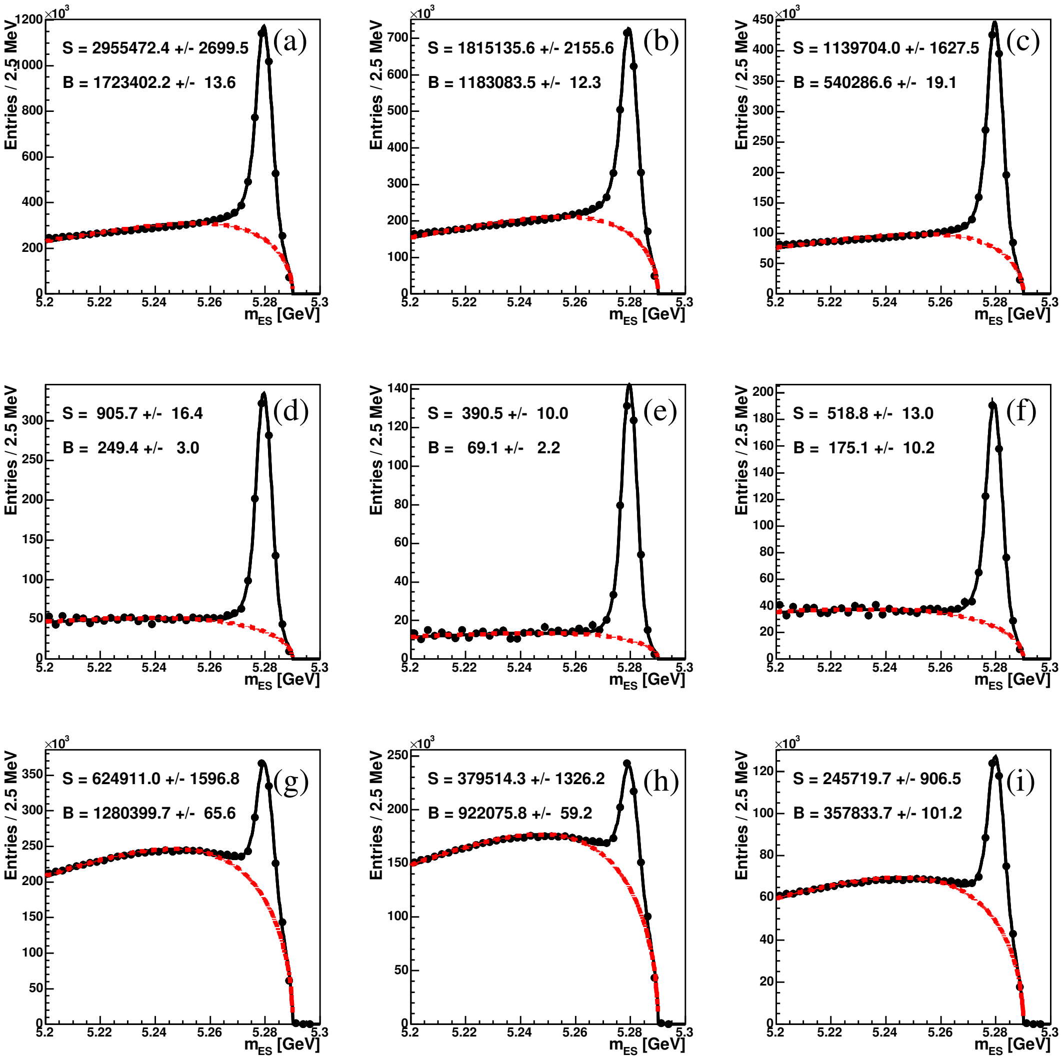

Figure 6.4: M_{ES} fits for the following event samples with integrated purity > 0.34: (a) simulated $B\overline{B}$ background, (b) simulated $B^{+}B^{-}$ background, (c) simulated $B^{0}\overline{B}^{0}$ background, (d) simulated signal, (e) simulated charged signal, (f) simulated neutral signal, (g) data, (h) data with charged B_{reco} candidates, (i) data with neutral B_{reco} candidates. S and B represent the fitted signal and background yields respectively.

6.1.3 Extraction of the Selection Efficiency (ϵ)

The selection efficiency, ϵ, is the B_{reco} event yield after applying the $B \to X_s\gamma$ selection criteria divided by the B_{reco} event yield before any signal selection requirements. The measurement includes the efficiency for requiring a reconstructed photon with energy exceeding $1.9\,\mathrm{GeV}$. It is measured using the simulated signal sample, and is found to be 0.479 ± 0.014.

6.2 Validation of the Method

To validate the measurement technique the analysis is performed first on simulated data. Approximately $210.5\,\mathrm{fb}^{-1}$ of simulated continuum and $B\overline{B}$ events are combined to represent the data sample. The signal component is removed from the remaining simulated $B\overline{B}$ sample and this is used to model the B background. Using the discarded $B \to X_s\gamma$ events to model the signal, the measured branching fraction is determined to be:

$$\mathcal{B}(B \to X_s\gamma) = (3.11 \pm 0.69(\mathrm{stat.})) \times 10^{-4}. \tag{6.5}$$

with a χ^2/DOF = 0.35 for the fit. If instead, the simulated generic signal sample (described in section 4.1.2) is used to model the signal component, the result obtained is:

$$\mathcal{B}(B \to X_s\gamma) = (3.63 \pm 0.75(\mathrm{stat.})) \times 10^{-4}. \tag{6.6}$$

with a χ^2/DOF = 2.07 for the fit. Both results are in good agreement with the branching fraction value of 3.29×10^{-4} for $B \to X_s\gamma$ decays in the $B\overline{B}$ event generator.

Further cross checks are performed using only $B\overline{B}$ events to model the data. Since continuum events are initially subtracted from the data, the same technique can be applied for a $B\overline{B}$ only data sample. A third of the simulated $B\overline{B}$ events are used to represent data, and the rest to model separately the background and signal components. The branching fraction is determined to be:

$$\mathcal{B}(B \to X_s\gamma) = (2.83 \pm 0.60(\mathrm{stat.})) \times 10^{-4}. \tag{6.7}$$

with a χ^2/DOF = 0.18 for the fit. If the simulated generic signal sample is used to model

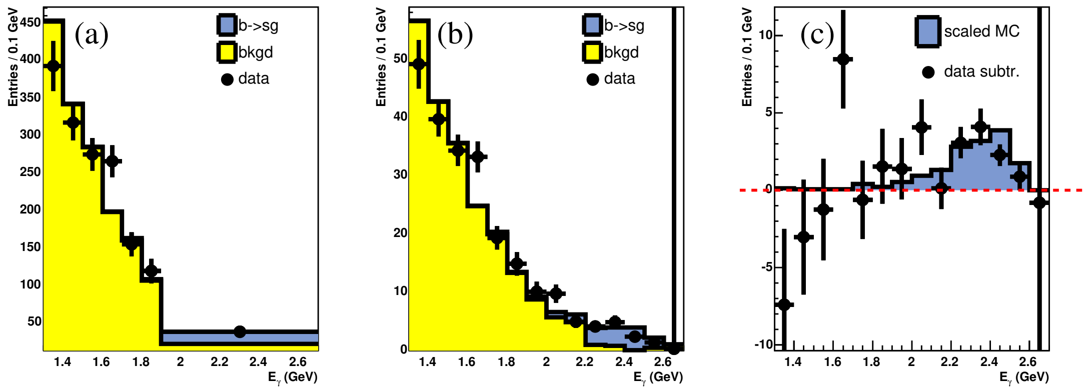

Figure 6.5: Results of the χ^2 fit to the E_γ distribution, with simulated continuum and $B\overline{B}$ events to represent data, and the $B \to X_s\gamma$ component of an independent $B\overline{B}$ sample to model the signal. (a) N_i^{meas} compared to $C_s N_i^{sig} + C_b N_i^{bkgd}$. (b) The same comparison with the region $E_\gamma > 1.9$ GeV displayed in bins of width 0.1 GeV. (c) Background subtracted data compared to $C_s N_i^{sig}$.

the signal, the result is:

$$\mathcal{B}(B \to X_s\gamma) = (3.59 \pm 0.67(\text{stat.})) \times 10^{-4}. \tag{6.8}$$

with a χ^2/DOF = 1.9 for the fit. These results are also compatible with the branching fraction for signal decays in the $B\overline{B}$ event generator.

The results of the χ^2 fit for each of the above trials are illustrated in figures 6.5 - 6.8. The left-hand plots compare N_i^{meas} to the sum of the signal and peaking background scaled with the χ^2 fit parameters (C_s and C_b). The bin ranges in these plots are those used for the χ^2 fit. The middle plots show the same comparison with the region $E_\gamma > 1.9$ GeV displayed in bins of width 0.1 GeV. The right-hand plots show data-simulation comparisons of the background subtracted photon energy distribution ($N_i^{meas} - C_b N_i^{bkgd}$). A photon energy spectrum is clearly visible above $E_\gamma > 1.9$ GeV, confirming that the method is suitable for extracting signal events from the data sample.

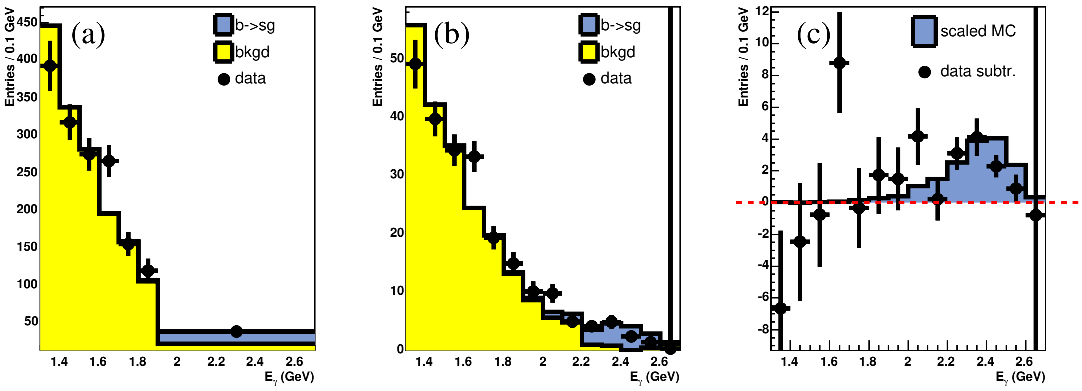

Figure 6.6: Results of the χ^2 fit to the E_γ distribution, with simulated continuum and $B\overline{B}$ events to represent data, and a simulated signal sample to model the signal. (a) N_i^{meas} compared to $C_s N_i^{sig} + C_b N_i^{bkgd}$. (b) The same comparison with the region $E_\gamma > 1.9$ GeV displayed in bins of width 0.1 GeV. (c) Background subtracted data compared to $C_s N_i^{sig}$.

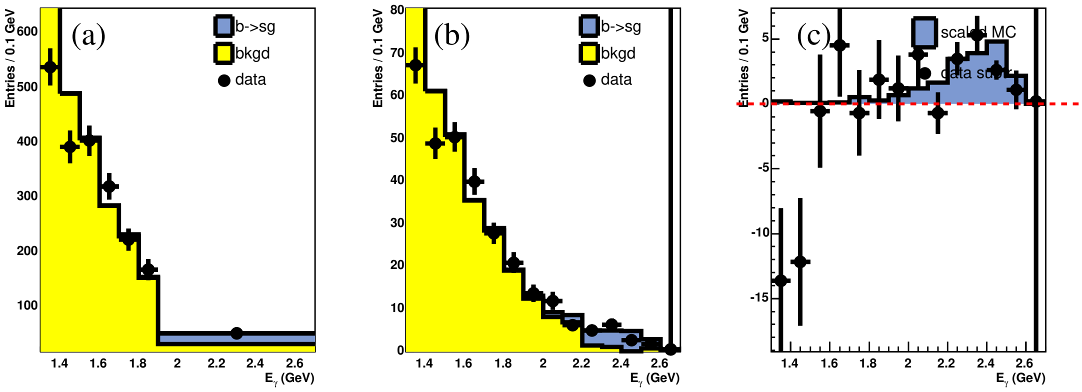

Figure 6.7: Results of the χ^2 fit to the E_γ distribution, with simulated $B\overline{B}$ events to represent data, and the $B \to X_s\gamma$ component of an independent $B\overline{B}$ sample to model the signal. (a) N_i^{meas} compared to $C_s N_i^{sig} + C_b N_i^{bkgd}$. (b) The same comparison with the region $E_\gamma > 1.9$ GeV displayed in bins of width 0.1 GeV. (c) Background subtracted data compared to $C_s N_i^{sig}$.

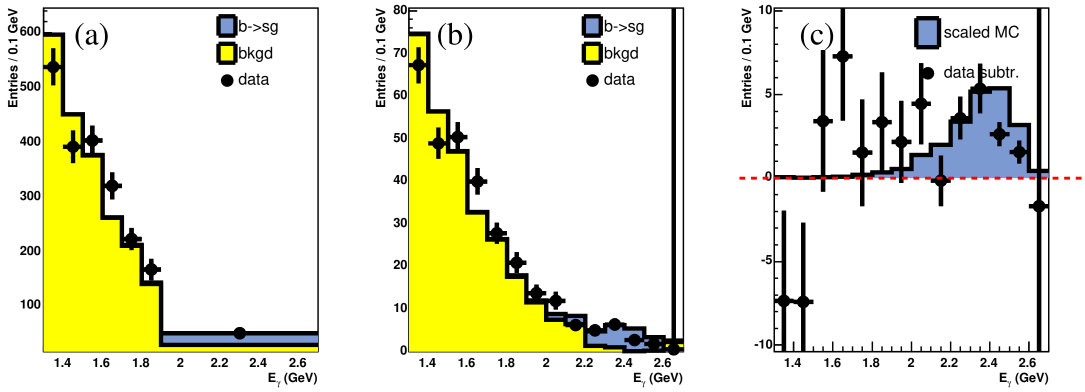

Figure 6.8: Results of the χ^2 fit to the E_γ distribution, with simulated $B\overline{B}$ events to represent data, and a simulated signal sample to model the signal. (a) N_i^{meas} compared to $C_s N_i^{sig} + C_b N_i^{bkgd}$. (b) The same comparison with the region $E_\gamma > 1.9$ GeV displayed in bins of width 0.1 GeV. (c) Background subtracted data compared to $C_s N_i^{sig}$.

6.3 The Result

The branching fraction result is measured using 210.5 fb^{-1} of data. Approximately 850 fb^{-1} of simulated $B\overline{B}$ events are used to model the background, and the combined KN480 non-resonant and $B \to K^*\gamma$ signal samples are used to model the signal. The result obtained is:

$$\mathcal{B}(\mathbf{B} \to \mathbf{X_s}\gamma) = (\mathbf{4.04} \pm \mathbf{0.83}(\mathbf{stat.})) \times \mathbf{10^{-4}}. \tag{6.9}$$

The χ^2/DOF of the fit is 0.89 indicating there is good agreement in the shape of the photon energy distribution for data and simulation. The measured components of the result are:

- The $B \to X_s\gamma$ signal yield, $N_{sig} = 125.8 \pm 25.8$ events.
- The B background yield, $C_b N^{bkgd} = 148.9 \pm 7.7$ events.
- The event yield that passes the signal selection criteria, $N^{meas} = 274.7 \pm 24.8$ events.

- The B_{reco} event yield, $N_B^{meas} = 624911 \pm 1597$ events.
- The signal selection efficiency, $\epsilon = 0.479 \pm 0.014$.

The χ^2 fit results are shown in figure 6.9. The bin ranges in the left-hand plot are those used for the χ^2 fit, with the largest bin being used to extract the signal yield. The background subtracted photon energy distribution in the right-hand plot is not the true photon spectrum. Although the selection criteria is aimed at having uniform efficiency, it does unavoidably favour high energetic photons. To extract the true distribution, corrections are required for the energy dependence of the efficiency, and also for the energy resolution of the detector. These will be necessary to measure the spectrum and extract the shape parameters when more statistics become available.

The statistical error on the measurement is large (20.6%) but will easily be reduced with the addition of more data. It is computed by repeating the measurement with the δN_i^{sim} term in the χ^2 formula (equation 6.3) set to zero. The uncertainty in the shape of the background and signal distributions from the finite simulated statistics is included in the systematic error. It is discussed in the next chapter, where all relevant systematic errors and theoretical uncertainties are evaluated.

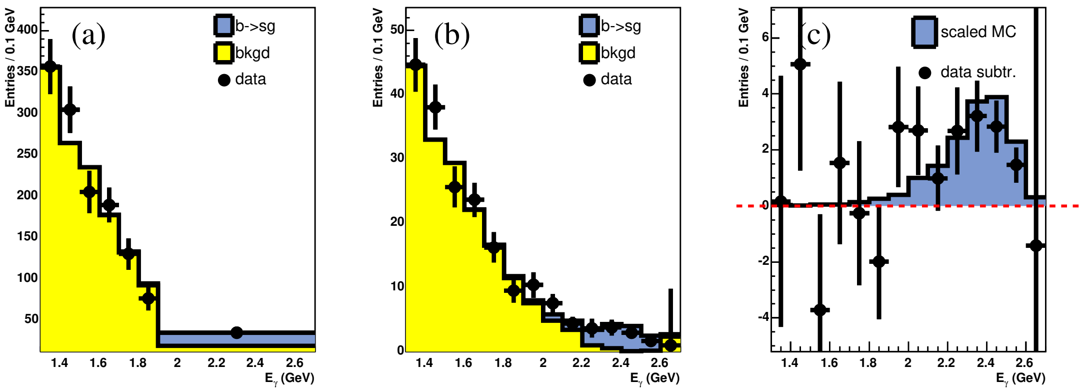

Figure 6.9: Results of the χ^2 fit to the E_γ distribution for the $\mathcal{B}(B \to X_s\gamma)$ measurement. (a) N_i^{meas} compared to $C_sN_i^{sig} + C_bN_i^{bkgd}$. (b) The same comparison with the region $E_\gamma > 1.9$ GeV displayed in bins of width 0.1 GeV. (c) Background subtracted data compared to $C_sN_i^{sig}$.

Chapter 7

Systematic Studies

Several systematic uncertainties must be accounted for in this analysis. They exist for each ingredient of the branching fraction measurement:

- The measured yield (N^{meas}), the B background yield (N^{bkgd}) and the B_{reco} event yield (N_B^{meas}) as determined from fitting the M_{ES} distribution of the B_{reco} candidates. They are each sensitive to the details of the fitting procedure.

- The B background normalization component (C_b) which is obtained from a binned χ^2 fit of combined signal and background samples to the measured photon energy distribution (described in section 6.1.1). It depends on how well the simulation describes the data, and on the finite available simulated statistics.

- The signal selection efficiency (ϵ) which is measured using the simulated signal sample (see section 6.1.3). This depends on the simulation quality, available statistics, and the theoretical model used to simulate the photon energy distribution.

These uncertainties are discussed in this chapter, and are summarized in table 7.6. The error arising from the signal model used in the simulation is not included with the overall systematic error, but is quoted as a separate theoretical error on the branching fraction result.

7.1 B_{reco} Reconstruction and Composition

In the branching fraction calculation it is assumed that the efficiency for reconstructing a B_{reco} candidate for any generic $B\overline{B}$ event ($\epsilon_{B_{reco}}^{B\overline{B}}$) is the same as for $B\overline{B}$ events where the B_{recoil} candidate decays $B \to X_s\gamma$ ($\epsilon^{sig}_{B_{reco}}$) . To test this hypothesis the measured number of B_{reco} events in the generic $B\overline{B}$ sample with a $B \to X_s\gamma$ on the B_{recoil} side is compared to the expected number, determined simply by multiplying the total B_{reco} yield in this sample by the generated branching fraction for $B \to X_s\gamma$ (3.29×10^{-4}). In both cases the yields are determined from fits to the M_{ES} distribution of the B_{reco} candidates, requiring an integrated purity greater than 0.34 as used in the branching fraction analysis. The ratio of efficiencies is found to be compatible with unity, and hence no correction is required:

$$\frac{\epsilon^{sig}_{B_{reco}}}{\epsilon^{B\overline{B}}_{B_{reco}}} = \frac{N^{B\to X_s\gamma}_{B_{reco}}}{(N^{B\overline{B}}_{B_{reco}} \times 3.29 \times 10^{-4})} = 0.973 \pm 0.048 \tag{7.1}$$

A possible difference in the B_{reco} reconstruction efficiency for the data and simulated event samples is not of concern in this analysis, as by construction the simulated signal and background event yields are normalized to match the data from a χ^2 fit to the photon energy distribution. Also, the $B \to X_s\gamma$ selection efficiency does not depend on the B_{reco} reconstruction efficiency since all event yields contributing to the branching fraction calculation (see equation 6.1) are of well reconstructed B candidates.

The selection criteria are designed to extract signal photons originating from the B_{recoil} , hence the branching fraction measurement should be independent of the composition of reconstructed modes of the B_{reco} candidates. To test this assumption, the measurement was repeated as a function of the minimum integrated purity requirement. Figure 7.1 shows that although some small variation exists, the result is consistent within the statistical uncertainty as the composition of the sample is varied.

The conclusion from these studies is that no systematic error is required for the B_{reco} reconstruction efficiency or composition.

7.2 Statistics of Simulated Samples

As each simulated sample has finite statistics, there is a statistical uncertainty in the shape of the signal and background models. This uncertainty is accounted for in the χ^2 fit by the presence of the $\delta N_i^{sim^2}$ term. To obtain the statistical error of the branching fraction for the available data, the measurement is repeated setting this term to zero. To extract the systematic uncertainty associated with the finite simulated statistics, the difference in

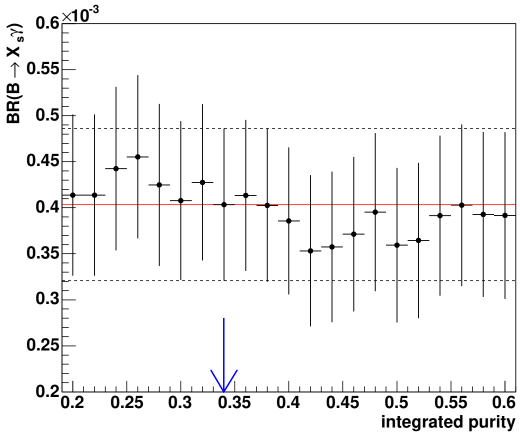

Figure 7.1: The $\mathcal{B}(B \to X_s\gamma)$ measurement as a function of the minimum integrated purity of the sample. The horizontal lines represent the branching fraction result and its statistical errors, obtained with the chosen minimum integrated purity requirement which is indicated by the arrow.

quadrature between the error obtained with and without the $\delta N_i^{sim\,2}$ term is calculated. The systematic uncertainty is determined to be 7.5%.

The selection efficiency also has a systematic uncertainty due to the limited statistics available for the simulated signal sample. The signal sample used in the measurement consists of the scaled KN480 non-resonant samples and the resonant $B \to K^*\gamma$ sample combined according to the Kagan and Neubert prescription. The available statistics are shown in table 4.1, and result in a 3.0% uncertainty in the signal selection efficiency.

7.3 The M_{ES} Fit

The systematic uncertainty associated with the M_{ES} fit arises from placing limits on or fixing parameters of the ARGUS and Crystal Ball functions used to fit the distribution. The chosen technique for the fit is described in section 4.2.4.

The N and ξ parameters of the ARGUS function are restricted. Their limits are the error boundaries of the same parameters obtained from an initial fit to the region $5.2 < M_{ES} < 5.265\ \mathrm{GeV}/c^2$ with an ARGUS function alone. As the region chosen for the initial ARGUS fit may influence the errors on the parameters, the measurement is repeated using the regions $5.2 < M_{ES} < 5.26\ \mathrm{GeV}/c^2$ and $5.2 < M_{ES} < 5.27\ \mathrm{GeV}/c^2$ instead. A maximum change in the branching fraction result of 5.4% is observed.

The tail parameter n of the Crystal Ball function is fixed to 5 for all M_{ES} fits. It is necessary to fix this parameter to ensure all the fits converge. The value for n was obtained from a M_{ES} fit to the signal sample with no constraints on the fit parameters. The branching fraction measurement is repeated varying this value by $\pm\,50\%$ to obtain a systematic error. A maximum change in the branching fraction result of 0.7% is observed.

To determine the systematic error from the fitting technique these two uncertainties are added in quadrature, giving an uncertainty of 5.4%.

7.4 Binning Effects

The effect of using different bin boundaries for the E_γ bins below $1.9\,\mathrm{GeV}$ in the χ^2 fit has been studied. For the branching fraction measurement the range $1.3 < E_\gamma < 1.9\,\mathrm{GeV}$ is split into equal bins of width $0.1\,\mathrm{GeV}$, so that the bin edges in GeV are $\{1.3, 1.4, 1.5, 1.6, 1.7, 1.8, 1.9\}$. These bin boundaries are varied as detailed in table 7.1, and the measurement is repeated. A maximum deviation from the branching fraction result of 2.7% is observed which is assigned as a systematic uncertainty.

E_γ Bin Boundaries (GeV)	Deviation from $\mathcal{B}(B \to X_s\gamma)$ result (%)
$\{1.3, 1.35, 1.45, 1.55, 1.65, 1.75, 1.9\}$	-1.23
$\{1.3, 1.36, 1.46, 1.56, 1.66, 1.76, 1.9\}$	-1.24
$\{1.3, 1.37, 1.47, 1.57, 1.67, 1.77, 1.9\}$	-1.95
$\{1.3, 1.38, 1.48, 1.58, 1.68, 1.78, 1.9\}$	-0.01
$\{1.3, 1.39, 1.49, 1.59, 1.69, 1.79, 1.9\}$	0.03
$\{1.3, 1.41, 1.51, 1.61, 1.71, 1.81, 1.9\}$	-1.76
$\{1.3, 1.42, 1.52, 1.62, 1.72, 1.82, 1.9\}$	-2.45
$\{1.3, 1.43, 1.53, 1.63, 1.73, 1.83, 1.9\}$	-0.89
$\{1.3, 1.44, 1.54, 1.64, 1.74, 1.84, 1.9\}$	-2.71
$\{1.3, 1.45, 1.55, 1.65, 1.75, 1.85, 1.9\}$	-2.18

Table 7.1: The effect on the branching fraction result of varying the E_γ bin boundaries for the χ^2 fit to the E_γ distribution.

7.5 Neutral Reconstruction

Differences between data and simulation in the reconstructed photon efficiency, resolution and energy scale, can effect the branching fraction result. The data-simulation agreement for the neutral reconstruction has been investigated within the *BABAR* collaboration. The studies carried out and corrections required for the simulation to match the data are described in the following subsections.

7.5.1 Photon Efficiency

The photon reconstruction efficiency is verified using samples of $e^+e^- \rightarrow \tau^+\tau^-$ events where the decay $\tau \rightarrow e\nu\bar{\nu}$ is identified for one of the τ decays [50]. The other τ decay is then studied. The ratio of the event yields for τ decays with one and two π^0 s, $R = N(\tau \rightarrow h^{\pm}\pi^0)/N(\tau \rightarrow h^{\pm}\pi^0\pi^0)$, is determined for data and simulation as a function of the π^0 energy, to evaluate possible differences in efficiency. Since the π^0 s are reconstructed from the decay $\pi^0 \rightarrow \gamma\gamma$, the event yields are influenced by the photon efficiency. It is found that for high energy isolated photons no efficiency correction is necessary [51]. The systematic uncertainty of this study gives a 2.5% uncertainty in the efficiency for reconstructing a photon, which gives directly a 2.5% uncertainty in the branching fraction measurement.

7.5.2 Photon Resolution Correction

The data-simulation agreement for the resolution of the calorimeter is checked by studying the π^0 mass from both $\tau \rightarrow h^{\pm}\pi^0$ and $\tau \rightarrow h^{\pm}\pi^0\pi^0$ decays [52]. The π^0 mass distribution is fitted to a third order polynomial function and a logarithmic normal distribution (known as a "Novosibirsk" function) in bins of π^0 energy. The resolution is compared for data and simulation. Energy smearing corrections need to be applied to the photons in order for the simulated π^0 mass resolution to match the data. In this analysis the smearing corrections are applied to all photons belonging to the B_{recoil} . The corrections are shown in table 7.2.

Data taking period	E_γ range (GeV)	Energy scale correction (%)	Gaussian smearing correction (%)
Run1	0.00-0.20	0.281	4.58
Run1	0.20-0.35	0.384	2.28
Run1	0.35-0.50	0.289	2.05
Run1	0.50-0.75	0.229	2.69
Run1	0.75-1.00	0.516	3.40
Run1	1.00-12.0	0.370	2.33
Run2-3	0.00-0.20	0.889	3.39
Run2-3	0.20-0.35	0.977	2.20
Run2-3	0.35-0.50	0.753	1.77
Run2-3	0.50-0.75	0.611	1.30
Run2-3	0.75-1.00	0.421	0.75
Run2-3	1.00-12.0	0.468	1.22
Run4	0.00-0.20	0.230	3.39
Run4	0.20-0.35	0.488	2.80
Run4	0.35-0.50	0.304	2.25
Run4	0.50-0.75	0.485	2.09
Run4	0.75-1.00	0.229	2.15
Run4	1.00-12.0	0.405	1.34

Table 7.2: Photon energy scale and energy smearing corrections to improve the data-simulation agreement for neutral reconstruction. The corrections for each energy range are applied to simulation produced to model data that is collected in the "data taking period" shown in the first column.

7.5.3 Energy Scale Correction

The calibration of the EMC is performed as a function of energy and polar angle in the laboratory frame as described in [32]. The data-simulation agreement for the energy scale of the calibrated EMC is also evaluated by studying the π^0 mass distribution from $\tau \to h^\pm\pi^0$ and $\tau \to h^\pm\pi^0\pi^0$ decays [53]. The π^0 mass distributions are fitted to the same function as described in 7.5.2 for the energy ranges shown in table 7.2, and the peak π^0 mass values are compared for data and simulation. Energy scale corrections for simulated photons which give data-simulation agreement are subsequently determined. These are shown in table 7.2, and are applied to photons belonging to the B_{recoil} .

7.5.4 Neutral Reconstruction Uncertainty

The uncertainty from applying the energy smearing and energy scale corrections detailed in table 7.2 is evaluated by comparing the branching fraction result obtained without the corrections to the final result with the corrections applied, thus assuming 100% uncertainty on the corrections. A deviation of 6.0% is observed. This is combined in quadrature with the photon efficiency uncertainty, to give an overall systematic error of 6.5% for the neutral reconstruction.

7.6 Data-Simulation Agreement

As simulation is required to estimate the signal selection efficiency, it is important that the simulation describes the data well for all variables used in the selection. Figure 7.2 shows the comparison of data and simulation (continuum plus $B\overline{B}$ samples) for these variables, and appendix B shows the same comparison for the Fisher input variables. For each bin of the variable plotted, the combinatorial background is subtracted from a fit to the M_{ES} distribution of the B_{reco} . The simulated samples are scaled to have the same ratio of charged to neutral B events as in the data before the fits to M_{ES} are performed. The distributions for data and simulation are normalized to the same area and tested for compatibility with a χ^2 test.

The overall data-simulation agreement is good for most variables. For low values of the LAT variable a small shift is observed in the simulated distribution with respect to data, and so the LAT requirement is relaxed to avoid selecting in this region.

As this is a blind analysis, a π^0 control sample is used to test the data-simulation agreement for the photon energy distribution. This control sample consists of events that fail the usual π^0 veto requirements and so is independent of the selected signal sample used for the measurement. Figure 7.3 shows the data-simulation agreement. The ratio of the distributions is fitted with a first order polynomial function. The fitted function is independent of photon energy within errors. Hence, it is concluded that there is no systematic difference between the data and simulation which might affect the photon energy distribution, and no correction is applied.

To further test the data-simulation agreement for the variables used to select signal events, the stability of the branching fraction result is studied by repeating the measurement after varying the main signal selection criteria. Figure 7.4 shows the branching fraction results as a function of the cut value of each variable used to select $B \to X_s\gamma$ events. The chosen selection criteria (in table 5.4) are applied for every variable, except

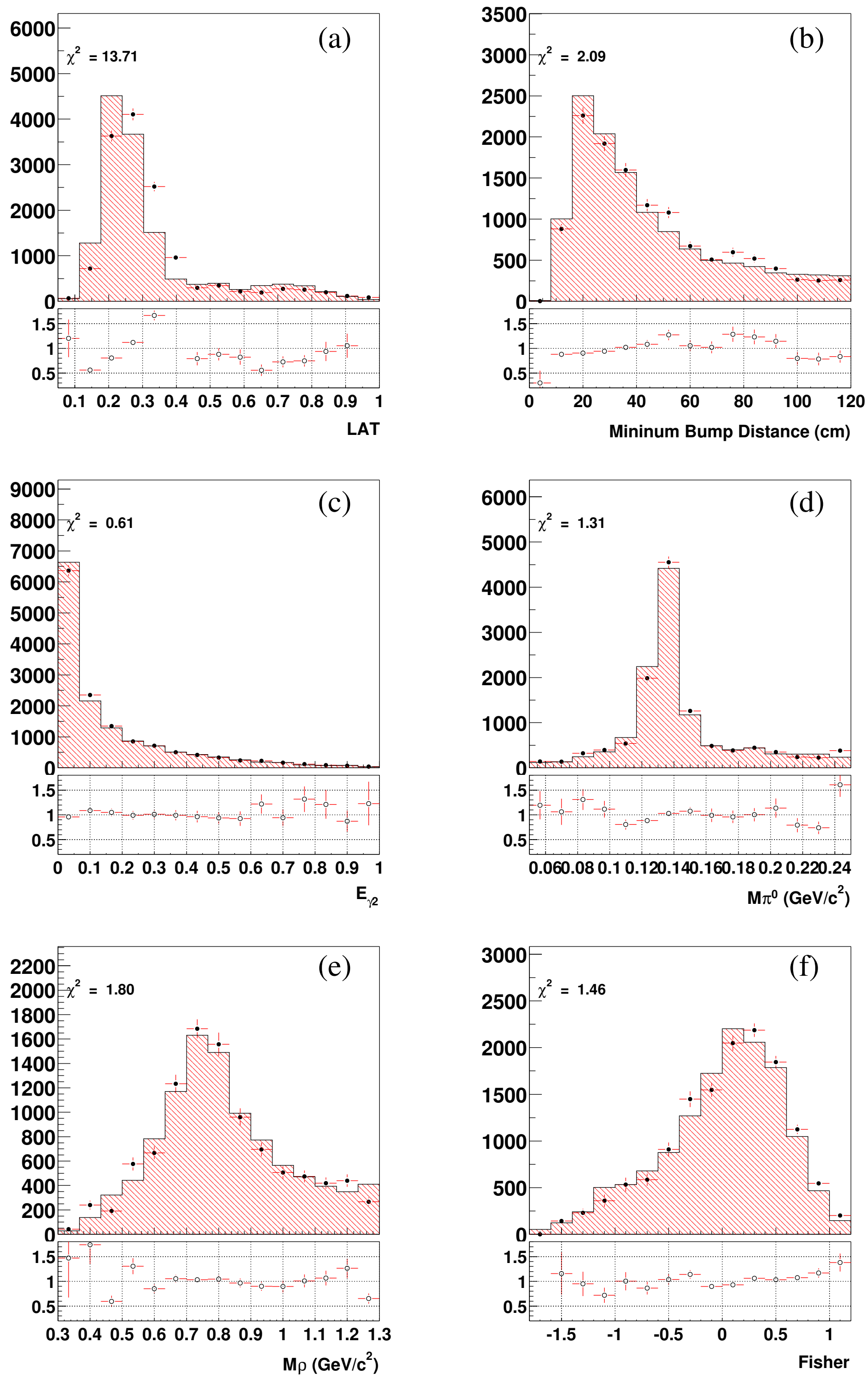

Figure 7.2: Plots showing the data-simulation agreement for the (a) LAT, (b) minimum bump distance, (c) energy of the second π^0 photon, (d) M_{π^0}, (e) M_ρ, and (f) Fisher distributions. The combinatorial background subtraction is performed for each bin, and an integrated purity > 0.34 is required. The distributions are normalized to the same area and their ratio, data (points) / simulation (histogram), is shown beneath each plot. The χ^2/DOF is indicated in each case as a test for compatibility.

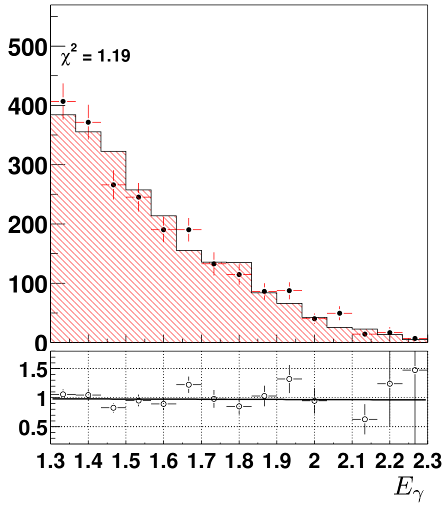

Figure 7.3: The data-simulation agreement of the photon energy distribution for the π^0 control sample (events that fail the π^0 veto requirement, but pass all other signal selection criteria). The combinatorial background subtraction is performed for each bin and the distributions are normalized to the same area. The χ^2/DOF is indicated as a test for compatibility. The ratio of the distributions, data (points) / simulation (histogram), is shown beneath the plot and is fitted with a first order polynomial function.

for the requirement that is varied.

The branching fraction results are stable when varying the selection criteria, even when changing the cut values by a large amount, with any variations significantly smaller than the statistical error. No systematic trends as a function of cut are observed. This shows that the simulation describes the data well. As the cuts are varied, the change in the estimated fraction of signal events in data is accommodated for by the selection efficiency measured from simulation. Hence in conclusion, no systematic error is required for the data-simulation agreement.

7.7 Model Dependence

The selection efficiency is determined from the signal sample and is therefore dependent on the theoretical model used to simulate the photon energy spectrum. It includes a component for requiring a signal photon with $E_\gamma > 1.9$ GeV to extrapolate the measured spectrum to the full E_γ range. The effect of varying the theoretical model is studied to evaluate the uncertainty in the selection efficiency. The overall efficiency is considered,

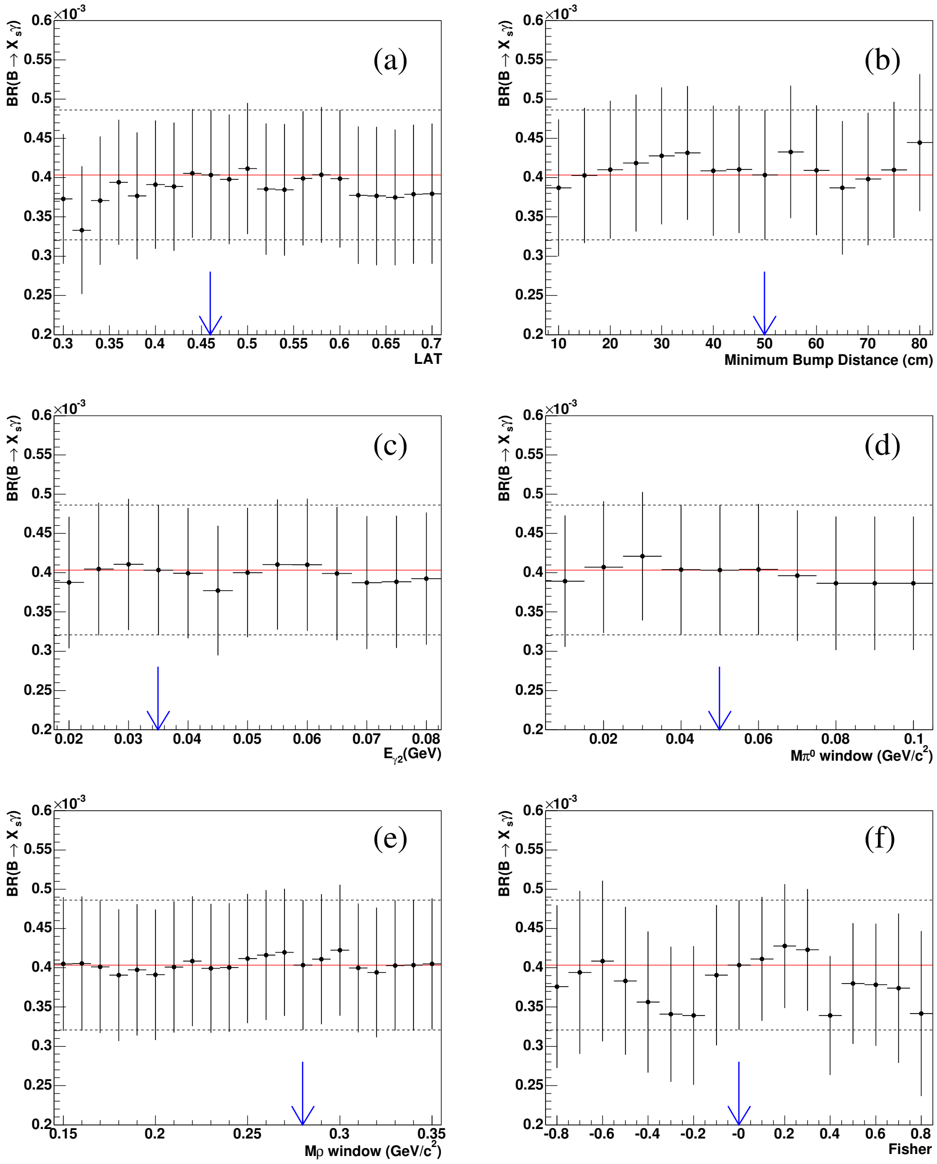

Figure 7.4: The $\mathcal{B}(B \to X_s\gamma)$ measurement as a function of the (a) LAT, (b) minimum bump distance, (c) energy of the second π^0 photon, (d) π^0 veto $M_{\gamma\gamma}$ window, (e) ρ veto $M_{\pi^0,\pi}$ window, and (f) Fisher cut values. The horizontal lines represent the branching fraction result and its statistical errors, obtained with the chosen values for the cuts which are indicated by the arrows.

not just the effect of the E_γ photon criteria, in order to account for any correlation between E_γ and the other selection variables.

Varying the signal model may also influence the background normalization coefficient, since the shape of the E_γ spectrum below 1.9 GeV is considered in the χ^2 fit. This effect is found to be negligible as very few signal events exist below 1.9 GeV after the signal selection criteria are applied. Only the change in selection efficiency is assigned as a theoretical error.

The model of Kagan and Neubert [21] is used in this analysis and is described in section 2.4. The uncertainty in this model arises from:

- the shape of the E_γ spectrum which depends on the input parameters m_b and μ_π,
- the cut-off point in the m_{X_s} spectrum ($m_{X_s}^{cut-off}$) below which the non-resonant $B \to X_s\gamma$ spectrum is replaced with the resonant $B \to K^*\gamma$ component,
- the fraction of $B \to K^*\gamma$ events in the photon spectrum.

The signal model used for the branching fraction measurement has a b quark mass of 4.80 GeV/c^2, and a $m_{X_s}^{cut-off}$ at 1.02 GeV/c^2 below which the non-resonant $B \to X_s\gamma$ spectrum is replaced with $B \to K^*\gamma$ events. The cut-off is computed such that the fraction of $B \to K^*\gamma$ events in the model is 11%. This corresponds to the ratio of the current experimental average branching fractions for $B \to K^*\gamma$ and $B \to X_s\gamma$ [4]. The effect on the selection efficiency of varying the model parameters is described in the following subsections.

7.7.1 Dependence on m_b

The Kagan and Neubert model [21] for the E_γ spectrum is parameterized in the variables m_b and μ_π. The authors prescribe that the b-quark mass should be varied between 4.65 and 4.95 GeV/c^2 keeping $\mu_\pi/\overline{\Lambda}$ constant (where $\overline{\Lambda} \approx m_B - m_b$), to evaluate the theoretical uncertainty. The dependence of the model on μ_π can be ignored as it is much smaller than the dependence on m_b.

The simulated KN465, KN480, KN495 and $B \to K^*\gamma$ cocktail signal samples are used to study the effect on the selection efficiency of varying m_b between the suggested limits. For each sample, $m_{X_s}^{cut-off}$ is computed such that the fraction of the m_{X_s} spectrum

signal sample	m_b (GeV/c^2)	$m_{X_s}^{cut-off}$ (GeV/c^2)
KN465	4.65	1.13
KN480	4.80	1.02
KN495	4.95	0.89

Table 7.3: The values of $m_{X_s}^{cut-off}$ computed for the Kagan and Neubert signal model [21] with different input values of m_b.

below the cut-off represents the $B \to K^*\gamma$ contribution of 11%. The $m_{X_s}^{cut-off}$ values used in this study are shown in table 7.3.

When setting m_b to 4.65 GeV/c^2 (4.95 GeV/c^2) a deviation is observed in the selection efficiency of -7.5% (+6.8%) away from the central value obtained with the KN480 sample. This change in the selection efficiency is assigned as a theoretical error and is the dominant source of the theoretical uncertainty on the branching fraction measurement.

7.7.2 Sensitivity to Assumed Branching Ratios

The $m_{X_s}^{cut-off}$ is computed such that the fraction of $B \to K^*\gamma$ events in the signal model always corresponds to the ratio of branching fractions for $B \to K^*\gamma$ and $B \to X_s\gamma$. The branching fractions used in this analysis are the average experimental results [4]:

- $\mathcal{B}(B^0 \to K^{*0}(892)\gamma) = (4.01 \pm 0.20) \times 10^{-5}$
- $\mathcal{B}(B^\pm \to K^{*\pm}(892)\gamma) = (4.03 \pm 0.26) \times 10^{-5}$
- $\mathcal{B}(B \to X_s\gamma) = (3.52^{+0.30}_{-0.28}) \times 10^{-4}$

The dependence of the selection efficiency on the fraction of $B \to K^*\gamma$ events in the model is studied by varying the $B \to K^*\gamma$ branching fraction within the experimental errors, keeping the total $B \to X_s\gamma$ branching fraction fixed. The KN480 and $B \to K^*\gamma$ generic signal samples are used for this study. The values of $m_{X_s}^{cut-off}$ and the fraction of $B \to K^*\gamma$ events used in each trial are shown in table 7.4. A variation in the selection efficiency of $\{0.4\%, -0.1\%\}$ from the central value is observed. This is assigned as a theoretical error.

Although the $B \to X_s\gamma$ branching fraction is the final result of this analysis, the shape of the photon energy spectrum in the simulation depends on the assumed $B \to X_s\gamma$

$\mathcal{B}(B^0 \to K^{*0}(892)\gamma)$ $(\times 10^{-5})$	$\mathcal{B}(B^\pm \to K^{*\pm}(892)\gamma)$ $(\times 10^{-5})$	$m_{X_s}^{cut-off}$ (GeV/c^2)	Fraction of $B \to K^*\gamma$ (%)
3.81	3.77	1.01	10.8
4.01	4.03	1.02	11.4
4.21	4.29	1.03	12.1

Table 7.4: The values of $m_{X_s}^{cut-off}$ computed with different $B \to K^*\gamma$ branching fractions.

$\mathcal{B}(B \to X_s\gamma)$ $(\times 10^{-4})$	$m_{X_s}^{cut-off}$ (GeV/c^2)	Fraction of $B \to K^*\gamma$ (%)
3.24	1.04	12.4
3.52	1.02	11.4
3.82	1.00	10.5

Table 7.5: The values of $m_{X_s}^{cut-off}$ computed with different $B \to X_s\gamma$ branching fractions.

branching fraction used to compute $m_{X_s}^{cut-off}$. The sensitivity of the selection efficiency to varying the $B \to X_s\gamma$ branching fraction used in the simulation within the experimental errors is studied. For this study the $B \to K^*\gamma$ branching fraction is kept constant. The $m_{X_s}^{cut-off}$ values used for each trial are shown in table 7.5. A variation in the selection efficiency of $\{-0.2\%, 0.4\%\}$ from the central value is observed and is assigned as a theoretical error.

7.7.3 Sensitivity to the Boundary Between $K^*\gamma$ and $X_s\gamma$

The m_{X_s} spectrum for the KN480 signal model has a sharp boundary at $m_{X_s}^{cut-off} = 1.02\,\mathrm{GeV}/c^2$, below which the non-resonant $B \to X_s\gamma$ spectrum is replaced with $B \to K^*\gamma$ events. In reality this boundary is a smooth transition. To take this into account, an uncertainty is computed by varying $m_{X_s}^{cut-off}$ between 0.92 and $1.12\,\mathrm{GeV}/c^2$ without changing m_b or the $B \to K^*\gamma$ fraction. The KN480 and $B \to K^*\gamma$ generic signal samples are used for this study. The variation in the selection efficiency from the central value obtained with $m_{X_s}^{cut-off}$ at $1.1\,\mathrm{GeV}/c^2$ is $\{+1.2\%, -1.2\%\}$. This uncertainty is assigned as a theoretical error.

7.7.4 Model Dependence Uncertainty

The overall model dependence uncertainty in the branching fraction result is determined by adding in quadrature the errors detailed in this section. It is dominated by the uncertainty on the b quark mass. The uncertainty is determined to be: $\{6.9\%, -7.6\%\}$.

7.8 $B \to X_d\gamma$ Subtraction

As there is no requirement of a strange particle in the signal event selection, $B \to X_d\gamma$ events also contribute to the measured signal yield. According to the standard model expectation, the $B \to X_d\gamma$ and $B \to X_s\gamma$ branching fractions are in the ratio $|V_{td}/V_{ts}|^2$. A previous analysis by the CLEO experiment [8] found approximately the same selection efficiency for $B \to X_d\gamma$ and $B \to X_s\gamma$ events. Assuming the efficiencies for the two decays are the same in this analysis, and $|V_{td}/V_{ts}|^2 = 0.040 \pm 0.016$ [16], a correction of $(-4.0 \pm 1.6)\%$ is applied to the final result to remove the $B \to X_d\gamma$ component. The 1.6% error is treated as a theoretical uncertainty.

7.9 Summary of the Systematics

The systematic errors and theoretical uncertainties decribed in this chapter are summarized in table 7.6. They are added in quadrature to give an overall systematic error of 12.0% and a total theoretical error of $\{+7.1\%, -7.8\%\}$. The largest systematic error comes from the uncertainty in the shape of the background model due to the limited simulated statistics available. This can be reduced by using a larger sample of simulated $B\overline{B}$ events to model the B background. An improvement in the M_{ES} fitting technique is necessary to reduce the error in the extraction of the B_{reco} yields. The error assigned to the neutral reconstruction may decrease in the future as detector effects are better understood. In addition, the large theoretical error can be reduced by minimizing the photon energy dependence of the selection criteria. It can also be reduced by lowering the minimum photon energy requirement when more data are available, and when background rejection methods are improved such that it will be possible to extract signal events at lower photon energies.

Source of Systematic Uncertainty	Relative Uncertainty (%)
Experimental	
B_{reco} reconstruction and composition	-
simulated statistics available	7.5
signal selection efficiency	3.0
M_{ES} fit	5.4
χ^2 binning effects	2.7
neutral reconstruction	6.5
Total	12.0
Theoretical	
$B \to X_d\gamma$ subtraction	1.6
model dependence	$\{+6.9, -7.6\}$
Total	$\{+7.1, -7.8\}$

Table 7.6: The systematic errors and theoretical uncertainties in the $B \to X_s\gamma$ branching fraction measurement.

Chapter 8

Conclusions

A measurement of the $B \to X\gamma$ branching fraction has been presented in this thesis using $210.5\,\mathrm{fb}^{-1}$ of data collected by the *BABAR* detector. The result obtained is:

$$\mathcal{B}(\mathbf{B} \to \mathbf{X_s}\gamma) = (\mathbf{4.04} \pm \mathbf{0.83}(\mathbf{stat.}) \pm \mathbf{0.48}(\mathbf{syst.})^{+\mathbf{0.29}}_{-\mathbf{0.32}}(\mathbf{theo.})) \times \mathbf{10^{-4}}. \qquad (8.1)$$

Figure 8.1 shows that this result is consistent with previous experimental measurements and the theoretical prediction based on the Standard Model. Hence there is no evidence to date to suggest that the decay rate is affected by new physics processes.

In this analysis high energetic photons recoiling to fully reconstructed B mesons were studied. Since the efficiency for selecting a reconstructed B candidate is low ($\sim 0.3\%$), the statistical uncertainty is the dominant error on the branching fraction result at present, but this will easily be reduced when more data are available. In order to compete with the precision of other $B \to X_s\gamma$ analyses (see table 1.1) the systematic uncertainty must also be reduced. This can be achieved by using larger samples of simulated events, and improving the M_{ES} fitting technique and neutral reconstruction.

Extracting signal events at the lower end of the photon energy spectrum where the signal is overwhelmed by hadronic background is a huge challenge for $B \to X_s\gamma$ analyses. The method described in this thesis is extremely effective at suppressing background. It is anticipated that with a larger data sample, one will be able to select signal events at photon energies below $1.9\,\mathrm{GeV}$ which will reduce the theoretical uncertainty on the branching fraction result. Furthermore, it will be possible to measure the shape of the photon energy spectrum directly in the B rest frame and extract the HQET parameters m_b, and λ_1. The full reconstruction of the non-signal B meson could be the preferred technique for such measurements of $B \rightarrow X_s\gamma$ decays when data samples of $\sim 1\text{ab}^{-1}$ are available.

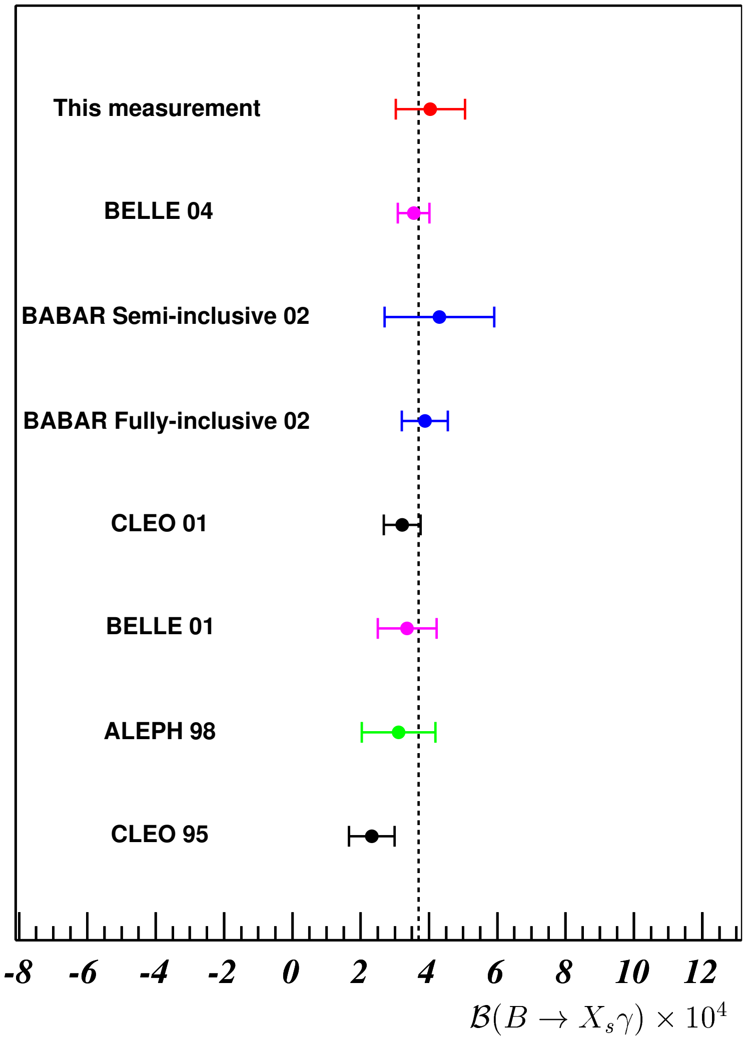

Figure 8.1: $B \rightarrow X_s\gamma$ branching fraction results for this analysis and the previous measurements detailed in table 1.1. The dotted line represents the central value of the most complete NLO theoretical prediction [3] based on the Standard Model.

Appendix A

M_{ES} Distributions of B Decay Modes

Figures A.1 - A.3 show the fitted M_{ES} distributions of the reconstructed B modes used in this analysis. The integrated purity > 0.34 criterion is applied and the rejected modes with high combinatoric background are not included.

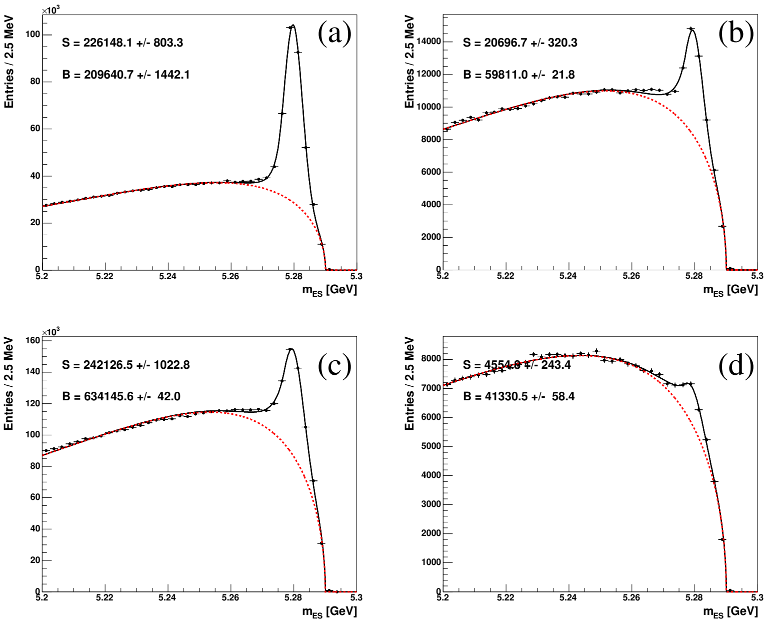

Figure A.1: Fitted M_{ES} distributions for $B \to D^{(*)}X$ where X consists of (a) π, (b) K, (c) $\pi\pi^0$ (with $M_X < 1.5$ GeV/c^2), and (d) $K\pi^0$ (with $M_X < 1.5$ GeV/c^2). S and B represent the fitted signal and background yields respectively.

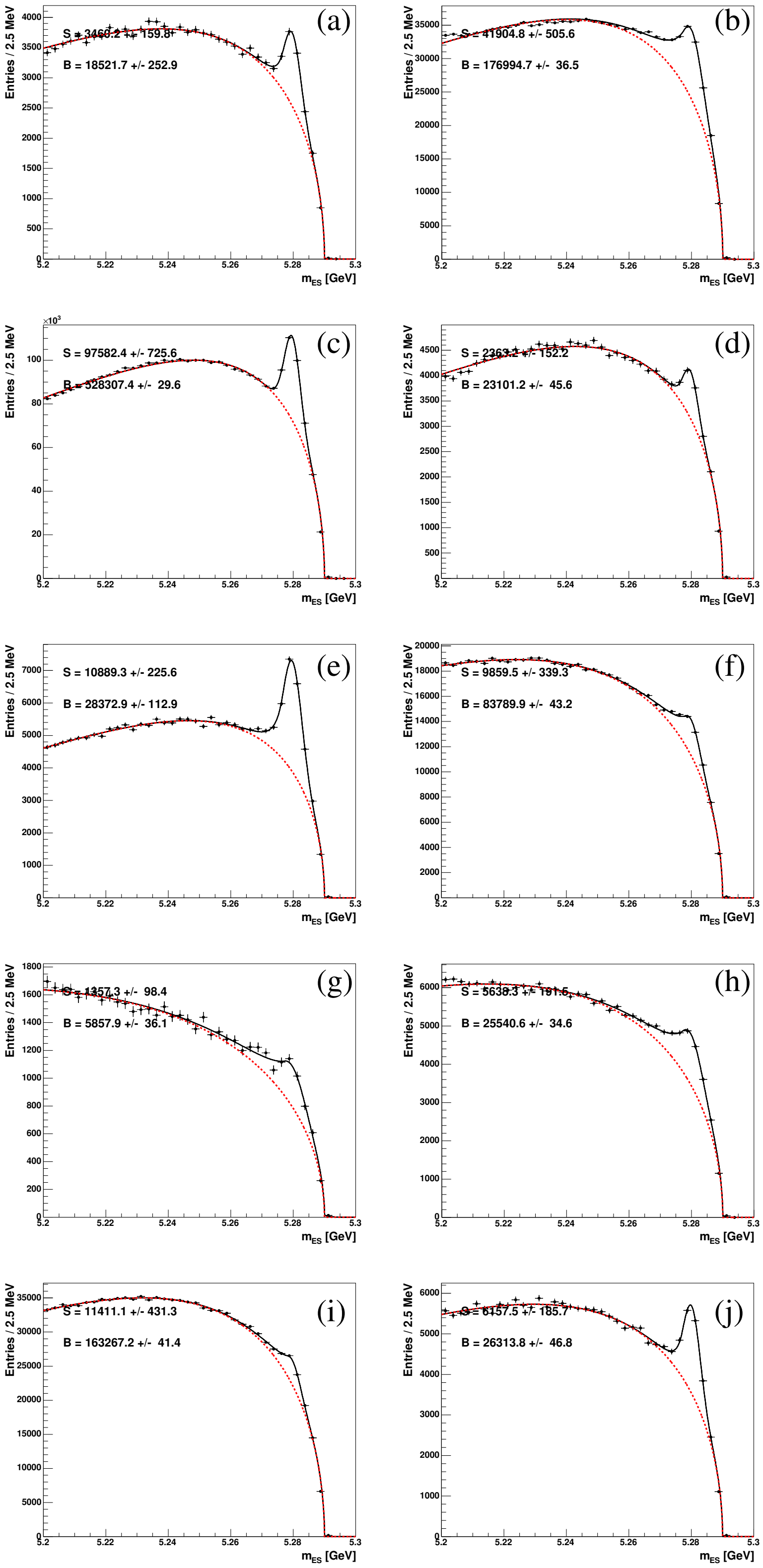

Figure A.2: Fitted M_{ES} distributions for $B \to D^{(*)}X$ where X consists of (a) KK^0_S, (b) $\pi\pi^0\ \pi^0$ (with $M_X < 1.5\ \mathrm{GeV}/c^2$), (c) $\pi\pi\pi$ (with $M_X < 1.5\ \mathrm{GeV}/c^2$), (d) $K\pi\pi$ (with $M_X < 1.5\ \mathrm{GeV}/c^2$), (e) $KK\pi D_S$, (f) ω, (g) $K\pi\pi\pi^0$ (with $M_X < 2.2\ \mathrm{GeV}/c^2$), (h) $KK\pi\pi^0$, and (i) $\pi\pi\pi\pi\pi$(with $M_X < 2.3\ \mathrm{GeV}/c^2$). (j) Fitted M_{ES} for $B \to D^{*+}X$ with $D^{*+} \to D^+\pi^0$. S and B represent the fitted signal and background yields respectively.

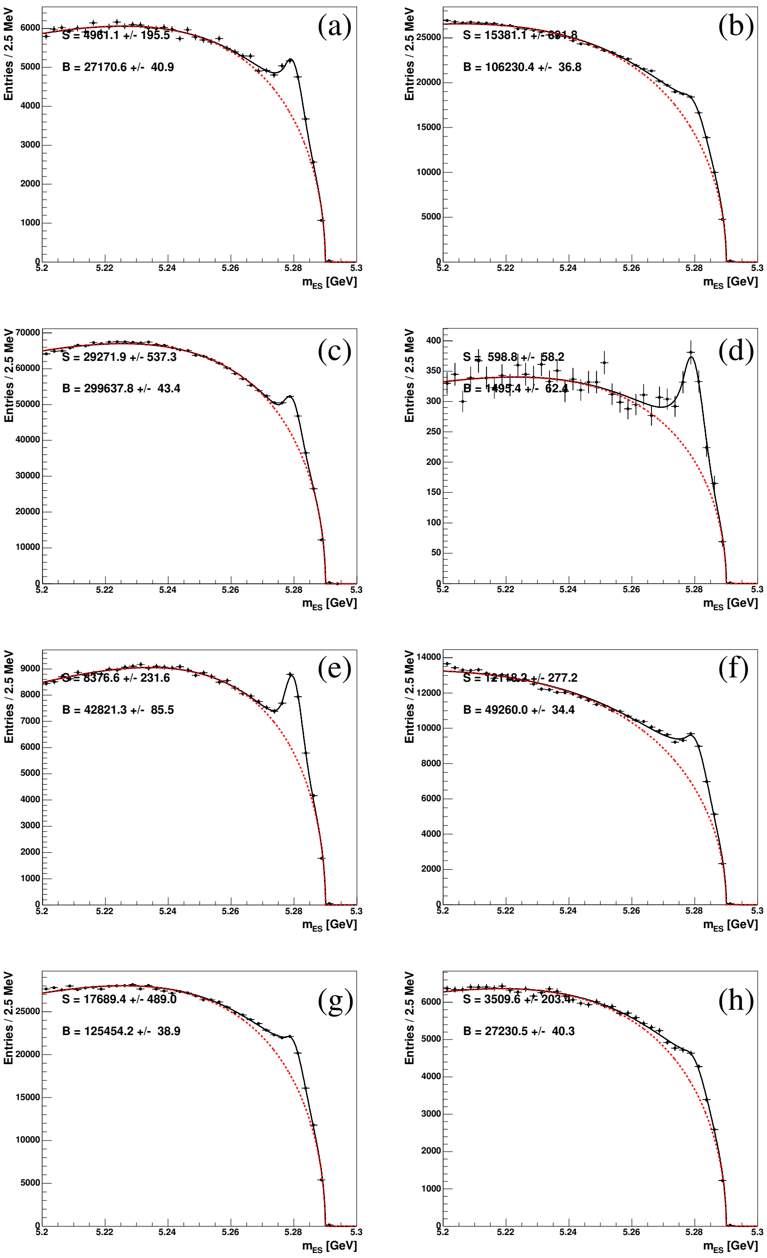

Figure A.3: Fitted M_{ES} distributions for $B \to D^{(*)}X$ where X consists of (a) $\pi\pi^0$ (with $M_X > 1.5$ GeV/c^2), (b) $\pi\pi^0$ π^0 (with $1.5 < M_X < 2.0$ GeV/c^2), (c) $\pi\pi\pi$ (with $1.5 < M_X < 2.0$ GeV/c^2), (d) $K\pi\pi$ (with $M_X > 1.5$ GeV/c^2), (e) $KK\pi$, (f) $\pi\pi\pi\pi^0$ (with $M_X < 1.6$ GeV/c^2), (g) $\pi\pi\pi\pi^0$ (with $1.6 < M_X < 2.2$ GeV/c^2), and (h) $K\pi^0$ K_S^0 (with $M_X > 1.8$ GeV/c^2). S and B represent the fitted signal and background yields respectively.

Appendix B

Data-Simulation Comparison Plots

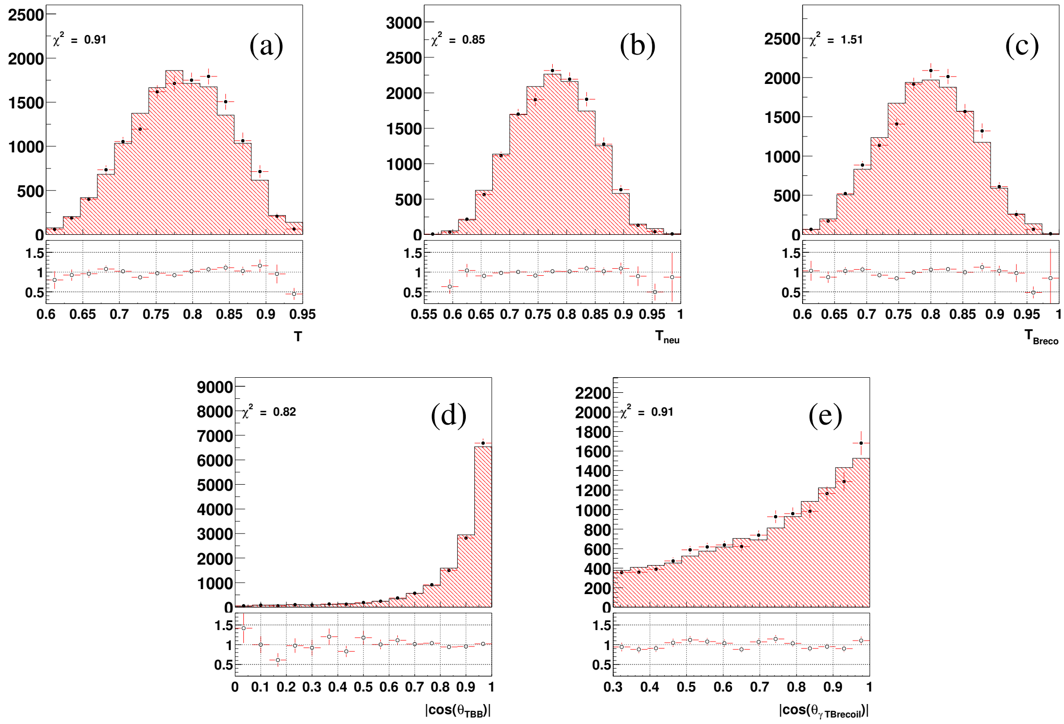

Figure B.1: The data-simulation agreement for event shape variable distributions: (a) T, (b) T_{neu}, (c) $T_{B_{reco}}$, (d) $|cos(\theta_{TBB})|$ and (e) $|cos(\theta_{\gamma T_{B_{recoil}}})|$. The combinatorial background subtraction is performed for each bin, and an integrated purity > 0.34 is required. The distributions are normalized to the same area and their ratio, data (points) / simulation (histogram), is shown beneath each plot. The χ^2/DOF is indicated in each case as a test for compatibility.

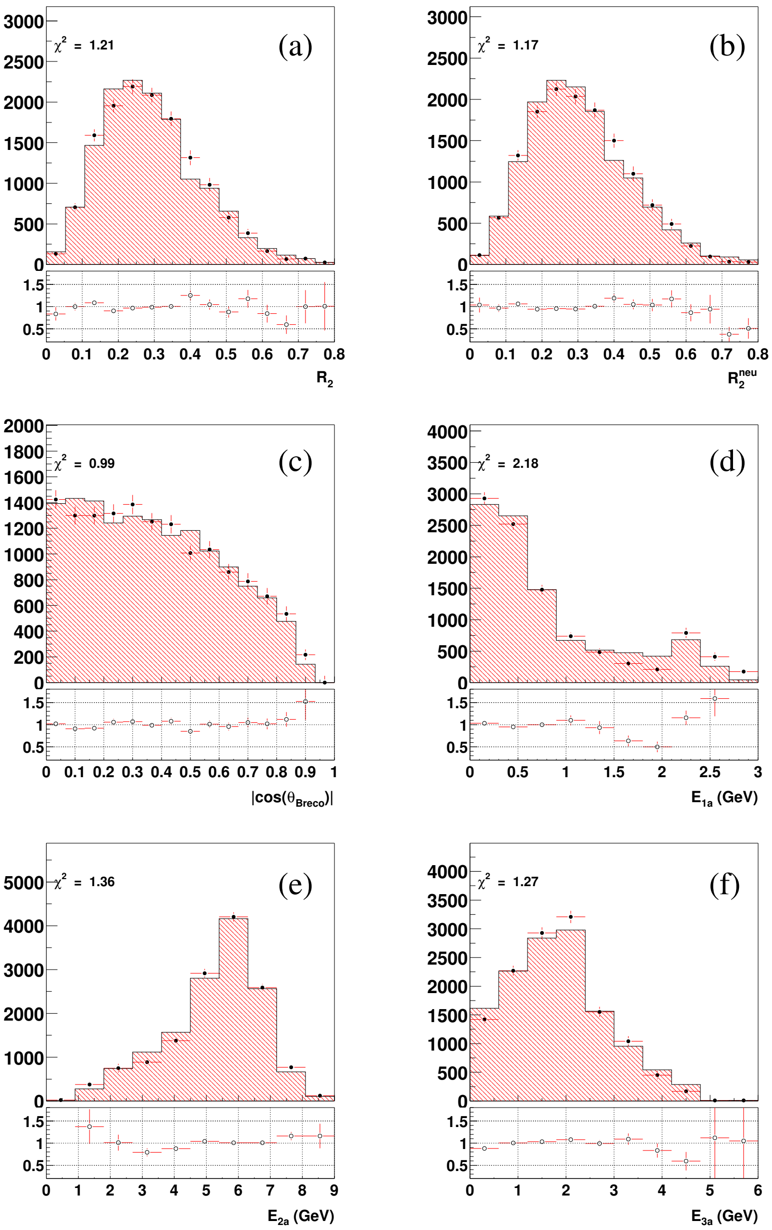

Figure B.2: The data-simulation agreement for event shape variable distributions: (a) R_2, (b) R_2^{neu}, (c) $|\cos(\theta_{B_{reco}})|$, (d)$E_{1a}$, (e)$E_{2a}$ and (f)E_{3a}. The combinatorial background subtraction is performed for each bin, and an integrated purity > 0.34 is required. The distributions are normalized to the same area and their ratio, data (points) / simulation (histogram), is shown beneath each plot. The χ^2/DOF is indicated in each case as a test for compatibility.

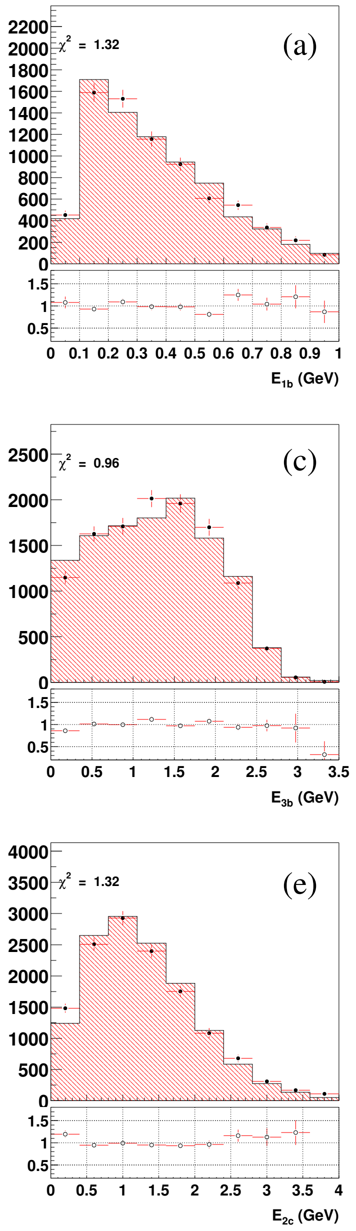

Figure B.3: The data-simulation agreement for the energy flow variables: (a)E_{1b}, (b)E_{2b}, (f)E_{3b}, (d)E_{1c}, (e)E_{2c} and (f)E_{3c}. The combinatorial background subtraction is performed for each bin, and an integrated purity > 0.34 is required. The distributions are normalized to the same area and their ratio, data (points) / simulation (histogram), is shown beneath each plot. The χ^2/DOF is indicated in each case as a test for compatibility.

Bibliography

[1] J. R. Ellis, M. K. Gaillard, D. V. Nanopoulos and S. Rudaz, Nucl. Phys. B **131**, 285 (1977).

[2] R. Ammar *et al.* [CLEO Collaboration], Phys. Rev. Lett. **71**, 674 (1993).

[3] A. J. Buras, A. Czarnecki, M. Misiak and J. Urban, Nucl. Phys. B **631**, 219 (2002).

[4] Heavy Flavor Averaging Group,
URL: http://www.slac.stanford.edu/xorg/hfag/rare/ichep04/rad_ll/, (2004).

[5] CLEO Collaboration, M.S. Alam *et al*, Phys. Rev. Lett. **74** 2885 (1995).

[6] ALEPH Collaboration, R. Barate *et al*, Phys. Lett B **429**, 169 (1998).

[7] Belle Collaboration, K. Abe *et al*, Phys. Lett. B **511**, 151 (2001).

[8] CLEO Collaboration, S. Chen *et al*, Phys. Rev. Lett. **87** 251807 (2001).

[9] *BABAR* Collaboration, B. Aubert *et al.*, Contributed to the 31^{st} International Conference on High Energy Physics (2002). hep-ex/0207074.

[10] *BABAR* Collaboration, B. Aubert *et al.*, Contributed to the 31^{st} International Conference on High Energy Physics (2002). hep-ex/0207076.

[11] Belle Collaboration, P. Koppenburg *et al*, Phys. Rev. Lett. **93** 061803 (2004).

[12] F. Halzen and A. D. Martin, "Quarks & Leptons, An Introductory Course in Modern Particle Physics", J. Wiley (1984).

[13] P. W. Higgs, Phys. Lett. **12**, 132 (1964).
P. W. Higgs, Phys. Rev. Lett. **13**, 508 (1964).

[14] N. Cabibbo, Phys. Rev. Lett. **10**, 531 (1963).

[15] S. L. Glashow, J. Iliopoulos and L. Maiani, Phys. Rev. D **2**, 1285 (1970).

[16] K. Hagiwara *et al.*, the Particle Data Group, Phys. Rev. D **66** 010001 (2002).

[17] L. Wolfenstein, Phys. Rev. Lett. **51**, 1945 (1983).

[18] J. H. Christenson, J. W. Cronin, V. L. Fitch and R. Turlay, Phys. Rev. Lett. **13**, 138 (1964).

[19] *BABAR* Collaboration, L. Lista, eConf **C0409272**, 010 (2004).

[20] S. Weinberg, ”The Quantum Theory of Fields, Volume III, Supersymmetry”, Cambridge University Press (2000).

[21] A. Kagan and M. Neubert, Eura. Phys. Jour, **7**, 5 (1999).

[22] P. Gambino and M. Misiak, Nucl. Phys. B **611**, 338 (2001).

[23] D. del Re, “Measurement of $|V_{ub}|$ Studying Inclusive Semileptonic Decays on the Recoil of Fully Reconstructed Bs with the *BABAR* Experiment”, PhD thesis, Università degli Studi di Roma “La Sapienza”, (2002).

[24] A. Bauras and M. Misiak, submitted to Acta Phys. Pol. B (2002).

[25] A. Ali and C. Greub, Phys. Lett. B **361**, 146 (1995).

[26] S. Bertolini, F. Borzumati and A. Masiero, Phys. Rev. Lett. **59**, 180 (1987).

[27] M. Luke, Prepared for Theoretical Advanced Study Institute in Elementary Particle Physics (TASI 2002): Particle Physics and Cosmology: The Quest for Physics Beyond the Standard Model(s), Boulder, Colorado, 2-28 Jun 2002.

[28] M. Misiak and M. Steinhauser, Nucl. Phys. B **683**, 277 (2004).

[29] Z. Ligeti, M. E. Luke, A. V. Manohar and M. B. Wise, Phys. Rev. D **60**, 034019 (1999).

[30] PEP-II: “An Asymmetric B Factory.” Conceptual Design Report, SLAC-R-418 (1993).

[31] *BABAR* Collaboration, D. Boutigny *et al.*, “*BABAR* Technical Design Report”, SLAC-R-0457 (1995).

[32] *BABAR* Collaboration, B. Aubert *et al.*, Nucl. Instrum. Meth. A **479**, 1 (2002).

[33] *BABAR* Collaboration, P. F. Harrison and H. R. Quinn (ed.), “The BaBar Physics Book: Physics at an Asymmetric B Factory”, SLAC-R-504 (1998).

[34] M. G. Green and T. R. McMahon, Contemp. Phys. **42**, 339 (2001).

[35] P. Billoir, Nucl. Instrum. Methods A **225**, 335 (1984).

[36] T. Brandt, “Electron Identification and Measurement of the Inclusive Semileptonic Branching Fraction of B Mesons at the *BABAR* Experiment”, PhD thesis, Technische Universität Dresden, (2001).

[37] G. Mancinelli and S. Spanier, “Kaon Selection at the *BABAR* Experiment”, *BABAR* internal note, BAD 116.

[38] D. J. Lange, Nucl. Instrum. Methods A **462**, 152 (2001).

[39] T. Sjöstrand, Comput. Phys. Commun **82**, 74 (1994).

[40] GEANT4 Collaboration, S. Agostinelli *et al.*, Nucl. Instrum. Meth. A **506**, 250 (2003).

[41] D. del Re *et al.*, "Semi-exclusive B Reconstruction", *BABAR* internal note, BAD 271.

[42] D. Dujmic, "Merged π^0 Reconstruction: From Cluster Shape to Mass", *BABAR* internal note, BAD 514.

[43] H. Albrecht *et al.*, The ARGUS Collaboration, Z. Phys. C **48**, 543 (1990).

[44] Crystal Ball Collaboration, "A Study of the Radiative Cascade Transition Between the Upsilon-prime and Upsilon Resonances", DESY F31-86-02.

[45] A. Sarti *et al.*, "Measurement of the Inclusive Charmless Branching Ratio and the Determination of $|V_{ub}|$ Based on the Hadron Mass Spectrum in $B \to X_u \ell \nu$ Decays", *BABAR* internal note, BAD 540.

[46] Fabio Bellini, "Measurement of the $b \to s\gamma$ Branching Ratio Studying the Recoil of Fully Reconstructed Bs with the *BABAR* Experiment", PhD thesis, Università degli Studi di Roma "La Sapienza", (2003).

[47] G. C. Fox and S. Wolfram, Nucl. Phys. B **149**, 413 (1979).

[48] R. A. Fisher, Annals of Eugenics **7** 179 (1936).

[49] Cornelius++ User Guide, URL: http://www.slac.stanford.edu/BFROOT/www /Physics/Tools/Tagging/Cornelius++/index.html

[50] "Study of π^0 Reconstruction Efficiency in Run I Data Using $\tau\tau$ 1-on-1 Decays", *BABAR* internal note, BAD 196.

[51] "Comparison Between Monte Carlo and Data of the π^0 Detection and Reconstruction Efficiency Using τ 1-on-1 Decays", *BABAR* internal note, BAD 378.

[52] "π^0 Reconstruction in Run I", *BABAR* internal note, BAD 20.

[53] "Study of the Effect of the EMC Energy Scale on Physics Analyses", *BABAR* internal note, BAD 765.